Lancaster University

Transient Flashes in Saturn's UV Aurora: an Analysis of Hubble Space Telescope 2013-2017 Campaigns and Cassini Magnetic Field Measurements

Tianshu Qin

Supervisor: Sarah V. Badman

This thesis is submitted for the degree of

Master of Science by Research

in the

Department of Physics

February 2022

Abstract

Transient flashes in Saturn's auroral images correspond to ~1 h quasiperiodic (QP) pulsations in *in-situ* particle and wave measurements at high latitudes. A previous investigation by Bader et al. (2019) showed these events mostly take place near dusk and link to magnetodisc reconnection. In this study, we examined northern auroral images from Hubble Space Telescope's (HST) 2013-2017 campaigns, identified 29 short-lived, recurrent features and examined simultaneous magnetometer (MAG) data collected by the Cassini orbiter. We found, when HST observation cadence permitted, a flash lifetime of 4-17 min (subject to uncertainties related to exposure times), and a 40-70 min periodicity in occurrence. A heat map was constructed to illustrate the aggregate occurrence of transient auroral signatures, and it shows a strong preference in both local time, 14-19 LT, and latitude, 75-85°. These transient flashes are identified in either the presence or absence of Saturn's main auroral oval, indicating the lacking of dependence on the main emission power. The concurrent magnetic field pulsations generally take a sawtooth shape rather than a sinusoid, and the local field strength can experience a change varying significantly from 0.5 to 5.0 nT (depending on the range of Cassini). The QP pulsation events were all detected when the spacecraft was in the southern hemisphere and are usually seen with a less bent-back field, suggesting closed field lines in a more dipolar configuration. One of the identified field pulsation events (in 2014-100) indicates that these features could occur at the ~21 LT region, in agreement with the spatial location of an identified, atypical flash (2016-232). We also found the ionospheric footprint of the spacecraft must be close to the region of flashes for magnetic field pulsations to be detected, indicating a localised rather than global driving process.

Declaration

I, Tianshu Qin, hereby declare that this thesis titled "Transient Flashes in Saturn's UV aurora" is my own original work that was done while in candidature for a research degree at Lancaster University. This work has not been submitted in substantially the same form for the award of a higher degree elsewhere. Any sections of the thesis which have been published, or submitted for a higher degree elsewhere, has been clearly identified. Where the work of others is quoted, the source is clearly given. Where a part of this thesis is based on joint efforts, I have made a clear acknowledgement of what was done by others and what was contributed by myself.

Date: 27 February 2022

Acknowledgement

Contents

List of Figures

List of Tables

1   Introduction

1.1   Single Particle Motion

In this section, the motion of an individual charged particle will be addressed, neglecting its direct interaction with the surrounding particles. A particle with charge q experiences the Coulomb force from the net electric field **E**,

$$\mathbf{F_C} = q\mathbf{E}. \tag{1.1}$$

A particle with charge q moving with a velocity **v** experiences the Lorentz force in a magnetic field **B** directed perpendicular to the particle's motion,

$$\mathbf{F_L} = q(\mathbf{v} \times \mathbf{B}). \tag{1.2}$$

The motion of a charged particle is determined by the effect of the electromagnetic field and is also the source of the fields. This is described by the Maxwell equations:

$$\nabla \cdot \mathbf{E} = \frac{\rho_q}{\varepsilon_0} \tag{1.3}$$

$$\nabla \cdot \mathbf{B} = 0 \tag{1.4}$$

$$\nabla \times \mathbf{E} = -\frac{\partial \mathbf{B}}{\partial t} \tag{1.5}$$

$$\nabla \times \mathbf{B} = \mu_0(\mathbf{j} + \varepsilon_0 \frac{\partial \mathbf{E}}{\partial t}) \tag{1.6}$$

Equation (1.3) and (1.4) are Gauss' laws for electricity and magnetism, respectively, with constants ρ_q as the charge density and ε_0 as the vacuum permittivity, equation (1.5) is the Maxwell-Faraday's law, and equation (1.6) is the Ampere-Maxwell's law where μ_0 is the vacuum permeability.

1.1.1   Gyration

Starting from Newton's second law, the motion of a charged particle with mass m under the influence of an electromagnetic field is given by the combination of the Coulomb force and Lorentz force,

$$\mathbf{F} = m\frac{\mathrm{d}\mathbf{v}}{\mathrm{d}t} = q(\mathbf{E} + \mathbf{v} \times \mathbf{B}). \tag{1.7}$$
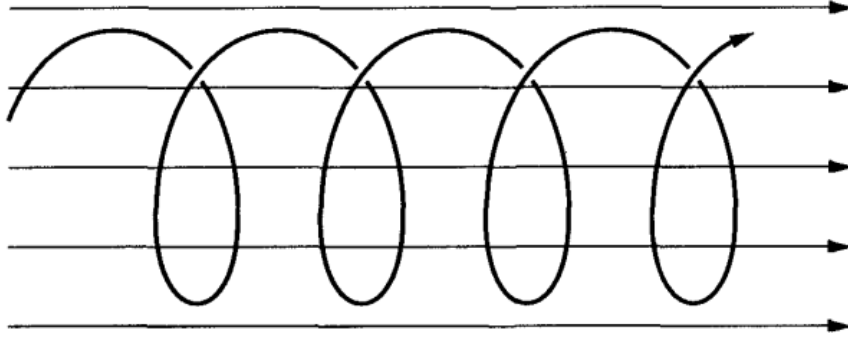
Figure 1.1: A charged particle moving in a helicoidal path as a result of the magnetic field and its velocity component along the direction of the field (indicated by the straight arrows to the right). Taken from: (Baumjohann and Treumann, 2012)

In a situation of only the presence of a uniform magnetic field, the equation is simplified to

$$m\frac{\mathrm{d}\mathbf{v}}{\mathrm{d}t} = q(\mathbf{v} \times \mathbf{B}). \tag{1.8}$$

The resulting force is always perpendicular to the direction of the particle's velocity, so this gives rise to a circular motion whose direction of motion is determined by the sign of the electric charge. Applying a dot product with velocity $\mathbf{v}$ to both sides of the last equation, we get

$$m\frac{\mathrm{d}\mathbf{v}}{\mathrm{d}t} \cdot \mathbf{v} = q(\mathbf{v} \times \mathbf{B}) \cdot \mathbf{v}, \tag{1.9}$$

where the left-hand side represents the change in kinetic energy and the right-hand side equals zero using the vector relation $\mathbf{X} \cdot (\mathbf{X} \times \mathbf{Y}) = 0$. This shows that the kinetic energy (and velocity) of the charged particle stays constant during this simple gyration, and the velocity here is noted $v_\perp$ as it is always oriented perpendicular to the magnetic field.

The angular frequency of the gyration (also known as gyrofrequency) about a guiding centre is given by

$$\omega_g = \frac{|q|\,B}{m} \tag{1.10}$$

and is independent of the sign of the particle's electric charge.

In a situation that the particle has an initial velocity component parallel to the magnetic field (noted as $v_\parallel$), the particle moves in a three-dimensional helicoidal path as shown in Figure 1.1. The pitch angle of this path – the angle the particle moves with respect to the magnetic field - is defined as

$$\alpha = \tan^{-1}\left(\frac{v_\perp}{v_\parallel}\right) \tag{1.11}$$

Hence $\alpha=90°$ describes a pure gyration with net velocity perpendicular to the magnetic field, while $\alpha=0$ (or 180°) describes the particle moving parallel (or anti-parallel) to the magnetic field.

1.1.2 Electron Drift

When taking the effect of electric field into account, the electrostatic force will result in an additional drift on the guiding centre of the particle's gyromotion. This drift velocity, named the E×B drift, is given by

$$\mathbf{v_E} = \frac{\mathbf{E} \times \mathbf{B}}{B^2} \tag{1.12}$$

and independent of either the particle's mass or the sign of the electric charge, hence electrons and ions drift with a common speed in the same direction.

For a charged particle in planetary magnetosphere, other forces generating the drift motion on the guiding centre are written as

$$\mathbf{F_\nabla} = -\mu \nabla B \tag{1.13}$$

$$\mathbf{F_p} = -m \frac{\mathrm{d}\mathbf{E}}{\mathrm{d}t} \tag{1.14}$$

$$\mathbf{F_g} = -m\mathbf{g} \tag{1.15}$$

$$\mathbf{F_C} = m v_\parallel^2 \frac{\mathbf{R_C}}{R_C^2} \tag{1.16}$$

They are related to the magnetic field gradient (1.13), polarisation (1.14), gravity (1.15) and magnetic field curvature (1.16), respectively, with $\mathbf{g}$ as the gravitational acceleration and $\mathbf{R_C}$ as the radius of the magnetic field curvature. The magnetic moment is given by the ratio between the perpendicular energy component and the magnetic field strength, and it takes the form

$$\mu = m \frac{v_\perp^2}{2B} = \frac{W_\perp}{B}. \tag{1.17}$$

1.1.3 Magnetic Mirroring

When a charged particle moves into regions with stronger field, its perpendicular velocity and energy will increase while the parallel components will decrease due to conservation of magnetic moment (1.17). The particle will hence have smaller velocity component along the field line as it enters greater magnetic field strength regions, until the instance when motion in this direction fully stops ($v_\parallel = 0$) and the particle's overall
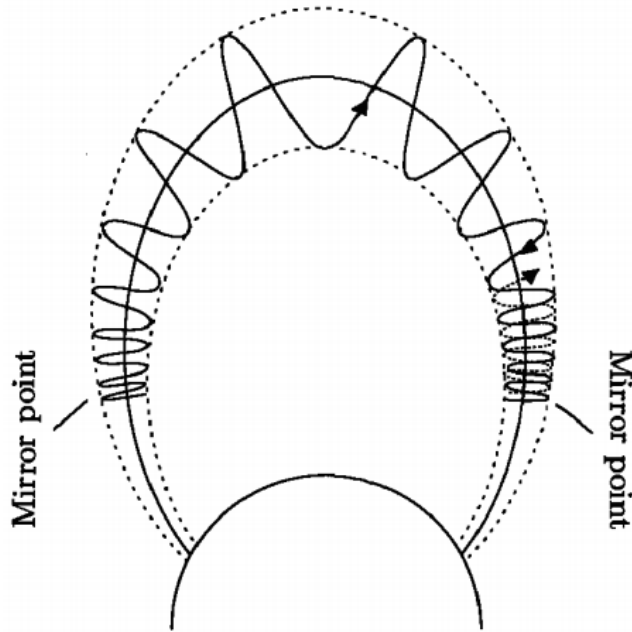
Figure 1.2: Schematics showing the bounce motion of a charged particle in a planetary magnetic field due to the confinement of the two magnetic mirrors at either end of the field line. Taken from: (Prolss, 2004)

motion becomes purely gyration. This location where the pitch angle $\alpha = 90°$ is known as the mirror point, and here the particle gets reflected back due to the persisting action of the parallel component of the gradient force (or the mirror force) $\mathbf{F}_\nabla$.

For a planetary magnetosphere, which is a magnetic dipole geometry with converging field lines at both ends and minimum field strength in the equatorial plane, there are two magnetic mirror points located at each end of the field line, making the charged particles trapped and bounce back and forth between the mirrors as illustrated by the sketch Figure 1.2.

Hence the pitch angle of the particle's gyromotion at a certain point can be determined by the ratio between the field strengths at that location, B, and at the mirror point, B_m:

$$\alpha = \sin^{-1}[(\frac{B}{B_m})^{1/2}] \tag{1.18}$$

1.1.4 Frozen-in Flux Theorem and Breakdown

We take the general form of Ohm's law

$$\mathbf{j} = \sigma_0(\mathbf{E} + \mathbf{v} \times \mathbf{B}), \tag{1.19}$$

where σ_0 is the plasma conductivity, and combine with Maxwell-Faraday's law (1.5) and Ampere-Maxwell's law (1.6) to obtain the induction equation:

$$\frac{\partial \mathbf{B}}{\partial t} = \nabla \times (\mathbf{u} \times \mathbf{B}) + \frac{1}{\mu_0 \sigma_0} \nabla^2 \mathbf{B} \tag{1.20}$$

where $\mathbf{u}$ is the bulk velocity, a macroscopic plasma property in magnetohydrodynamics (MHD). The two terms on the right-hand side of this equation represent, respectively, the convective and diffusive motion of the plasma.

The frozen-in magnetic flux theorem is based on the situation when magnetic diffusion is neglected, that is, there is negligible electric resistance (or infinite conductivity σ_0). Hence the convective term in equation (1.20) dominates while the diffusive term is reduced, yielding the hydromagnetic theorem, or frozen-in flux theorem with the following equivalent expression:

$$\mathbf{E} + \mathbf{v} \times \mathbf{B} = 0 \tag{1.21}$$

This equation shows that there is no electric field in the frame moving with the plasma in a scenario with infinite conductivity. The ratio between the convective and diffusive terms in equation (1.20) is defined as the magnetic Reynolds number which tells whether the magnetic field is convection or diffusion dominated. The expression is

$$R_m = \mu_0 \sigma_0 L_B V \tag{1.22}$$

where L_B is the characteristic length over which the field varies and V is the average plasma velocity perpendicular to the field. In cases when diffusion is neglected (e.g., in typical collisionless space plasma), one will have $\sigma_0 \sim \infty$, hence the Reynolds number will be $R_m \gg 1$. The motion of the magnetic field is dominated by the flow together with the plasma, in other words, the magnetic flux is frozen-in into the flow.

However, in the process of magnetic merging, where the magnetic topology changes through the breaking of the field lines and the reconnection to other field lines, the aforementioned frozen-in flux concept breaks down. For a configuration of two anti-parallel magnetic field lines drawn as the left panel of Figure 1.3, the change in field
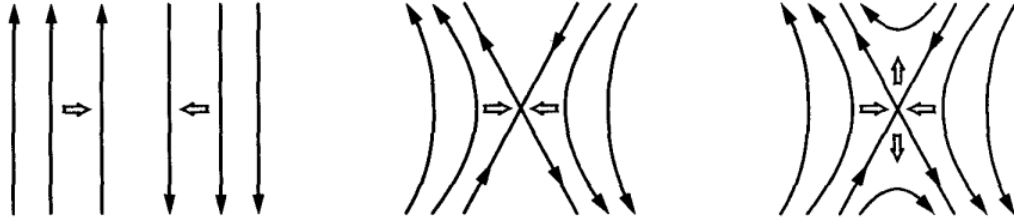
Figure 1.3: Sketches of the evolution of magnetic field line merging and reconnection. Taken from: (Baumjohann and Treumann, 2012)

across the boundary between the two field lines creates a thin current sheet within the boundary. The merging occurs when the field lines move towards the current and become a "X" configuration as shown in the middle panel of Figure 1.3, with zero field strength at the reconnection site, the magnetic neutral point or the "X-line". The antiparallel field lines are broken at the neutral point, and sections on one side are reconnected with those on the other side as shown in the right panel of Figure 1.3. The newly reconnected field lines are comprised of plasmas from both sides of the current sheet and get ejected from the neutral point.

1.2 Saturn's Magnetosphere

A planet's magnetosphere is a cavity formed by the fact that its terrestrial magnetic field gets distorted by the flow of the solar wind. This region – a protective bubble – has multiple layers of structures as shown in Figure 1.4 and is dominated by the planet's own magnetic field and plasma. The solar wind plasma does not escape the interplanetary magnetic field lines due to the aforementioned frozen-in flux theorem, and the interplanetary magnetic field lines cannot easily penetrate into the planet's magnetic field. Magnetopause, the boundary separating the two regions, is where the kinetic pressure of the solar wind plasma balances the magnetic pressure from the planet's magnetic field and plasma. In the dayside (frontside) the field lines are compressed, while in the nightside they are stretched into magnetotail. Saturn has the second largest magnetosphere among all solar system planets after Jupiter. This section briefly addresses the structure of Saturn's magnetosphere and its dynamic processes.

1.2.1 Radiation Belts

Radiation belts are located in Saturn's inner magnetosphere, formed by efficient trapping and accumulating mechanisms of high energy protons and relativistic electrons (from hundreds of keV to tens of MeV) and other ions (Gombosi et al., 2009). Sat-
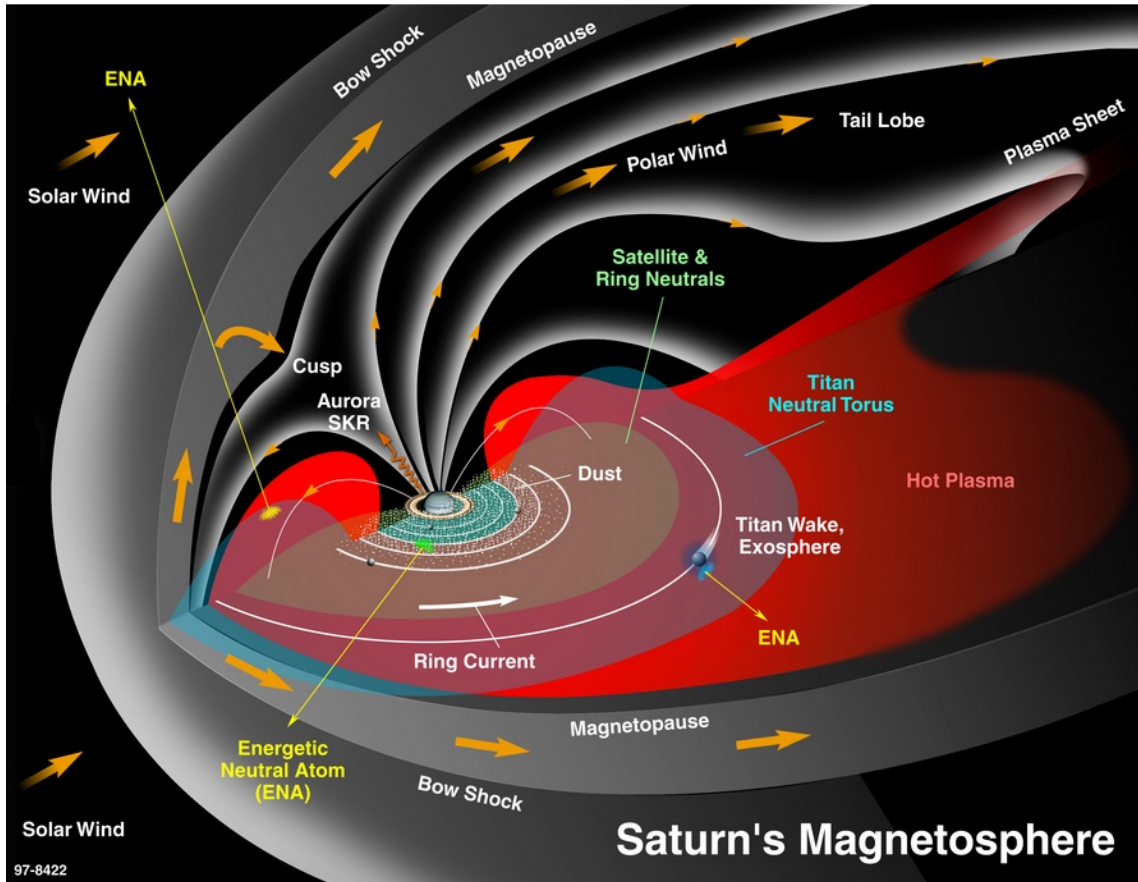
Figure 1.4: A global view of the structure of Saturn's magnetosphere. Image credit: NASA/JPL.

urn's permanent ion radiation belt sits between just above the planet's surface (∼1.03 Rs) and the orbit of Tethys (4.9 Rs) (Kollmann et al., 2013). The belt is separated by the orbits of Saturn's moons due to proton absorption by the moons, and Tethys stops ion transport from the belt to the outside (Roussos et al., 2008) as illustrated by the multiple cut-offs in proton measurements in Figure 1.5. The electron radiation belt extends from the outer edge of A-ring (2.7 Rs) till ∼7 Rs (Roussos et al., 2014). The source particles for the planetary radiation belts are thought to be directly given by Cosmic ray albedo neutron decay (CRAND) process. Galactic cosmic rays (GCR) impact Saturn's atmosphere or rings and create secondary neutrons through nuclear reactions, the secondary neutrons subsequently decay back into protons and electrons which can be magnetically trapped and populate the radiation belts. The radiation belt dynamics and proton intensity were observed to be directly connected to the solar activity (Gombosi et al., 2009; Roussos et al., 2011). Shprits et al. (2018) proposed whistler mode chorus waves and hiss waves as potential accelerators of radiation belt electrons.
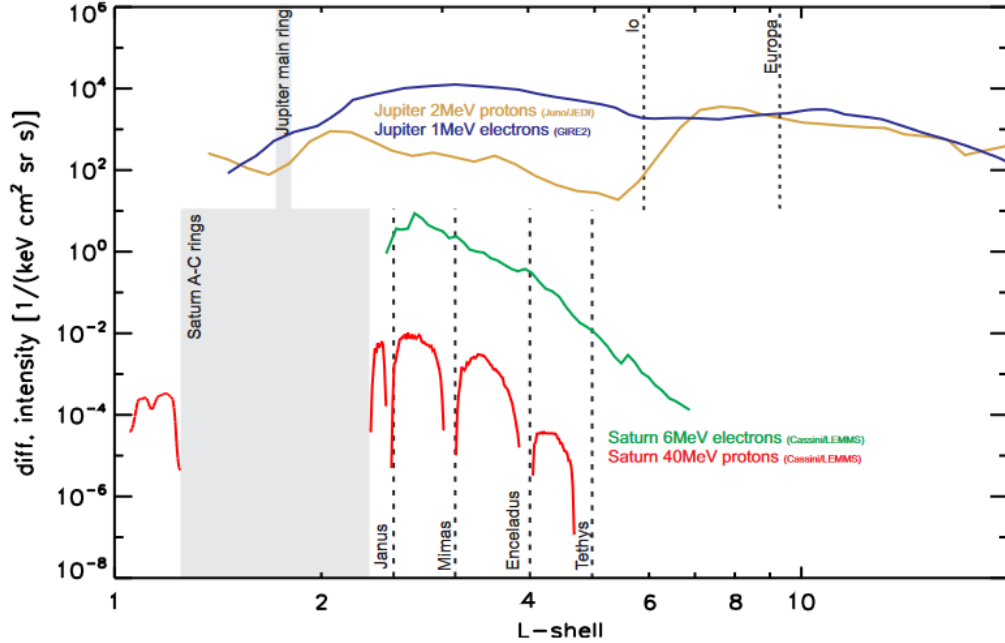
Figure 1.5: Intensity profiles of the radiation belts of Jupiter and Saturn. Saturn measurements include both Cassini average data outside of rings and corrected proton components inward of rings (Kollmann et al., 2018; Roussos et al., 2018).

1.2.2 Ring Current and Magnetodisc

Saturn's ring current and its connection to the solar wind has been intensively investigated with Pioneer 11 (Smith et al., 1980), Voyager (Connerney et al., 1981, 1983; Ness et al., 1982) and Cassini observations (Bunce et al., 2007, 2008; Kellett et al., 2009, 2010, 2011).

The ring current - an invisible ring of eastward drifting positive ions - was inferred to be located between 8 and 16 Rs according to Voyager data and carries a total azimuthal current of ∼10 MA (Connerney et al., 1983). It takes the shape of a full or sometimes a partial doughnut as shown by the red region (i.e., high intensity) in Figure 1.6a. Furthermore, the ring current is found usually asymmetric in local time due to thermal plasma pressure, strongest at dusk (Sergis et al., 2017) and highly dynamic with modulations due to solar wind pressure (Arridge et al., 2006; Guio et al., 2020) and the corresponding position of the magnetopause (Bunce et al., 2007). The latter also updated that the inner edge of the ring current is located at 6.5 Rs while the outer margin extends to 21 Rs as indicated by the dashed line on the planet's equatorial plane in Figure 1.6b, where the ring current extends from the plasma sheet to within a few saturnian radii of the magnetopause on the dayside while merging into the tail of the plasma sheet on the nightside. Furthermore, the ring current is understood to

8

be periodically enhanced by hot plasma injections (see Section 1.4) (Paranicas et al., 2005; Carbary et al., 2008; Mitchell et al., 2009; Provan et al., 2021).

The effect of outward plasma pressure plus centrifugal forces exceeds that of the magnetic tension in the outer magnetosphere and hence stretches the field lines radially outward from a dipole configuration to form the magnetodisc (Kivelson, 2015). Arridge et al. (2008b) observed the displacement of Saturn's magnetospheric current and plasma sheet away from the incoming solar wind direction at all observed local times, indicative of a bowl shape as shown in Figure 1.6c. Bunce et al. (2007) showed that the dynamics of the internal stresses giving rise to Saturn's ring current play an important role in producing the dayside magnetodisc. Moreover, Arridge et al. (2008b) pointed out that the magnetopause straightens out the field lines and resists stretching, thus a compressed magnetosphere forms a quasi-dipolar configuration on the dayside like Earth (predicted by Connerney et al. (1980)), while this confinement occurs at a rather larger radial distance for an expanded magnetosphere forming the stretched-out magnetodisc (supported by Bunce et al. (2008)).

1.2.3 Magnetopause and Magnetotail

Saturn's magnetopause stand-off distance is typically located at ∼20-25 Rs with the full range observed between 16-40 Rs (Pilkington et al., 2015), highly inconstant due to both internal plasma pressure and solar activity (Arridge et al., 2006; Achilleos et al., 2008; Pilkington et al., 2015). On the night flank, the magnetotail is formed when the magnetospheric field lines can elongate to much greater radial distances, and the vastly stretched field lines become almost parallel as sketched in Figure 1.6b. The tail lobes, the open flux regions outside the plasma sheet as marked and labelled in Figure 1.4, are magnetic field lines connecting the planet's ionosphere on one end while closing at the other end to nightside solar wind magnetic field (Gombosi et al., 2009). One may explore more detailed studies on magnetotail dynamics referring to Arridge et al. (2011); Jackman (2013); Badman et al. (2014).

1.3 Magnetospheric Dynamics

1.3.1 Centrifugal Interchange

Saturn's magnetospheric plasma population is mainly provided by the water plume ejection from its moon Enceladus located at ∼4 Rs. The planet's magnetospheric dynamics include processes of mass loss in the magnetodisc on various spatial and time scales and are dominated by the planetary rotational effects. In the inner magnetosphere, the pri-

(a)

(b)

(c)
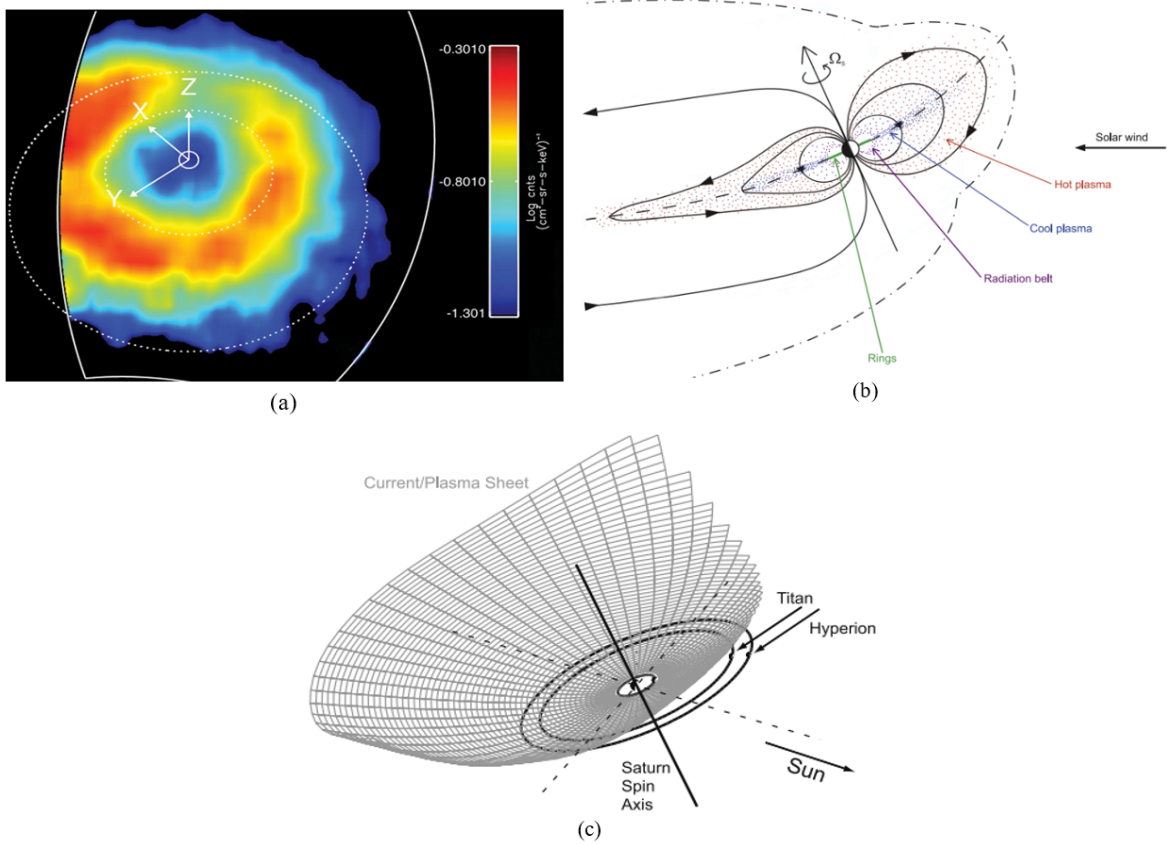
Figure 1.6: (a): Colour map of Saturn's ring current by recording the intensity of the escaping particles using Cassini's ion and neutral camera taken on 19 March 2007. Saturn is at the centre, the Z-axis points parallel to planet's spin axis, the X-axis points sunward, and the Y-axis points toward dusk. Two white dotted circles are the orbits of the moon's Rhea and Titan respectively, indicative of the general inner and outer boundaries of the ring current. (b): Sketch of key constituents and their general configurations in the noon-midnight meridian of the magnetosphere for Saturn's southern hemisphere summer conditions. (c): Three-dimensional schematic showing the bowl-shaped current/plasma sheet. Image credit: NASA/JPL/APL (a); Kellett et al. (2009) (b); Arridge et al. (2008a) (c).

mary mechanism for outward mass transport is thought to be the centrifugally driven flux tube interchange instability (Southwood and Kivelson, 1987). As the flux tubes with cold and dense plasma at the inner magnetosphere travels radially outward, the hot and tenuous plasma at the middle magnetosphere is injected towards the planet to conserve magnetic flux, while reducing the centrifugal potential energy of the system, as illustrated by Figure 1.7 (Thomas et al., 2004; Hill et al., 2005). The outward moving plasma is lost via magnetotail reconnection and plasmoid ejection, modulated by the variable upstream solar wind environment and the planetary period oscillations described below (Arridge et al., 2011; Bradley et al., 2018). The inward-moving hot plasma injections processes are observed at 6-10 Rs (Hill et al., 2005; Azari et al., 2018) and may be triggered by the arrival of larger, hot plasma injections originating from a more distant reconnection site (Mitchell et al., 2015; Thomsen and Coates, 2019).
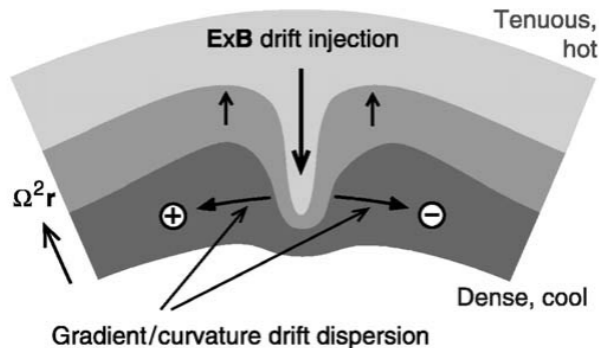
Figure 1.7: Cartoon demonstrating centrifugal interchange instability - the injection of hot plasma into the region of cold plasma while the latter is transported outward. Taken from: Hill et al. (2005)

1.3.2 Vasyliunas Cycle and Dungey Cycle

One of the major sources of a planet's plasma circulation is the Vasyliunas cycle. As the magnetospheric plasma is carried outward through rapid rotation overwhelming the magnetic tension, a reconnection site (drawn as the dashed line with "X" mark in Figure 1.8) is expected to form in the magnetotail to release a fraction of the plasma and magnetic field threading it. The disconnected plasma and field (plasmoids) are "pinched off" downtail, while the returning plasma along the reconnected field lines are heated and accelerated (Kivelson and Southwood, 2005). Therefore, the outer magnetosphere forms a layer of more energetic flux tubes (70% of rigid corotation) on the dawnside (Richardson and Sittler Jr, 1990). The effects of the solar wind only come into play at large radial distances downtail, so the process is vastly dominated by the internally driven (sub)corotation of the planet (Vasyliunas, 1983; Brice and Ioannidis,

1970). Cassini-era observations suggested reconnection could occur at all local times in the magnetodisc, not just the midnight sector (Delamere et al., 2015; Guo et al., 2018b).

The other main source is the solar wind driven Dungey cycle which dominates the flux circulation at Earth (Dungey, 1961) but is less significant in fast-rotating gas giants (i.e., Jupiter and Saturn). As illustrated by Figure 1.8, the planet's magnetic field lines open to the solar wind at the dayside magnetopause (shown by magnetopause "X" line) are drawn towards the pole then carried down the tail. At the nightside, the tail reconnections sites are more towards the dawn due to the planet's rapid rotation (shown by tail "X" line), and the newly closed flux tubes are drawn back, following magnetic tension, to the planet into a dipolar configuration and then towards the dayside via dawn where they start another revolution. The returning flux tubes on the dawnside through the Dungey cycle experience an acceleration to 80% of rigid corotation (Cowley et al., 2004b). At Saturn, the global plasma convection is a pattern with coexistence of both internal (Vasyliunas cycle) and external (Dungey cycle) elements as depicted by Cowley et al. (2004a) in Figure 1.8, although the Vasyliunas cycle dominates as the Dungey cycle occurs only in rather thin layers in the outer magnetosphere and is significant only during solar wind compressions (Badman and Cowley, 2007).

1.4 Planetary Rotational Modulation

Saturn's rotational modulations by planetary period oscillations (PPOs) have been observed in various magnetospheric parameters (reviewed by Carbary and Mitchell (2013)). To briefly address this fascinating topic, there are two separately driven PPO systems, one associated with the northern hemisphere and the other with the southern, with different periods (Kurth et al., 2016; Gurnett et al., 2009; Andrews et al., 2010; Provan et al., 2011). These systems give rise to intervals of thickening and thinning of the nightside plasma/current sheet during their rotational cycles, as well as north-south oscillations (Morooka et al., 2009; Provan et al., 2012; Cowley and Provan, 2017). MHD simulations were used to model PPO modulations with a twin-vortex current system in the planet's polar ionosphere (Jia et al., 2012) driven by asymmetric thermospheric heating (Smith, 2011), and the connection between the modulations and PPO related FACs was also observed (Hunt et al., 2014, 2015; Southwood and Cowley, 2014; Chowdhury et al., 2022).

Figure 1.9 thoroughly illustrates the two separate PPO systems on the northern (a-d in the left column) and southern (e-h in the right column) hemisphere. Figure 1.9(a) and (e) show the bird's eye view from above the north pole and through the planet
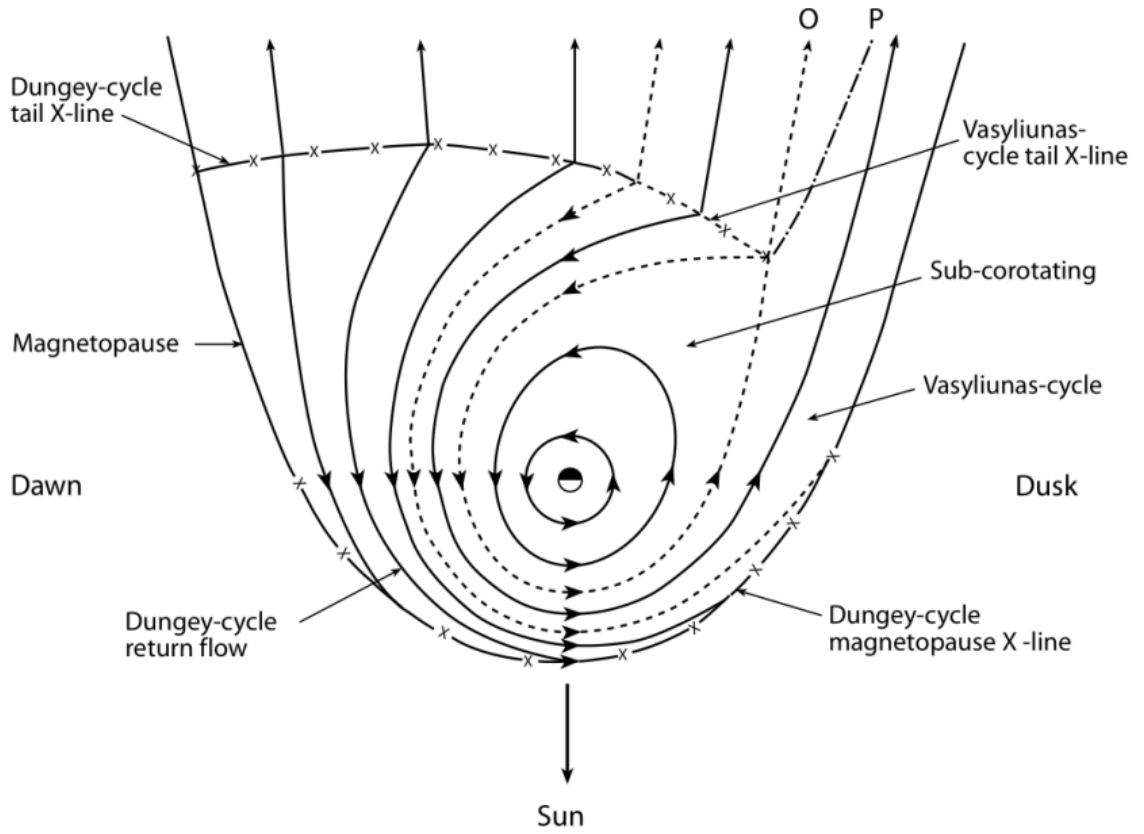
Figure 1.8: Schematic of plasma flows in Saturn's magnetosphere viewing down the equatorial plane with the Sunward direction to the bottom of the page. The solid lines with "X" marks show the Dungey-cycle reconnection sites, and the dashed line with "X" marks corresponds to the Vasyliunas-cycle reconnection site. The dashed line marked with "O" represents due to the Vasyliunas cycle. The dot and dash line marked with "P" stands for the outer limit of the plasmoid. Taken from: Cowley et al. (2004a)

to the southern ionosphere. The rotation phase angle, $\Psi_{N,S}$, represents the azimuthal orientation of the northern and southern PPO systems, respectively, relative to the noon meridian Andrews et al. (2011). Red streamlines represent the ionospheric twin-vortex flow as mentioned above (Jia et al., 2012), while green and blue components show the current flows and the magnetic field perturbations. The current and field orientations in the $\Psi_{N,S} = 90 - 270°$ meridian plane are illustrated in Figure 1.9(b) and (f), while the $\Psi_{N,S} = 0 - 180°$ meridian plane in (c) and (g), where the black arrowed lines indicate Saturn's intrinsic magnetic field. Figure 1.9(d) and (h) show the overall effect by field perturbations in the $\Psi_{N,S} = 0 - 180°$ meridian plane, where the PPO modulations give rise to the opposite effects on two sides of the planet. The thickening of the plasma/current sheet for $\Psi_N = 180°$ and $\Psi_S = 0$ ° and the thinning for $\Psi_N = 0°$ and $\Psi_S = 180°$ are the consequence of either constructive and destructive superposition of the PPO-related fields (Figure 1.9(c) and (g)) onto the planet's background field. The effects of the two PPO systems are simultaneously present in the nightside plasma/current sheet (Hunt et al., 2018; Provan et al., 2018b,a, 2019). Thus, the resultant modulation is given by the relative rotation phase (also known as the "beat phase") of the two systems:

$$\Delta\Psi = \Psi_N - \Psi_S \qquad (1.23)$$

When two PPO systems are in phase ($\Delta\Psi = 0°$) the north-south oscillations of the plasma/current sheet are maximum whereas the thickening and thinning effects are minimum. Contrarily, when the two oscillations are in antiphase ($\Delta\Psi = 180°$) we have minimum the north-south oscillations and maximum thickening and thinning effects. Magnetic reconnection in the tail is more likely to correspond to thinned current sheet, hence it is favored under PPO antiphase conditions. Bradley et al. (2020) found that major compression-response events were triggered during solar wind compressions and when the two PPO systems were in antiphase, resulting in maximum variations in the thickness of the current sheet.

PPO modulations are observed in all measurements, but, aurora-wise, the modulation-driven variations in current density on auroral field lines, which connect the planet's polar ionosphere to the magnetosphere, gives rise to a periodic modulation in auroral intensity (Nichols et al., 2010a; Badman et al., 2012b; Nichols et al., 2016; Bader et al., 2018) and the location of the main auroral oval (Provan et al., 2009; Nichols et al., 2010b, 2016; Bader et al., 2018).
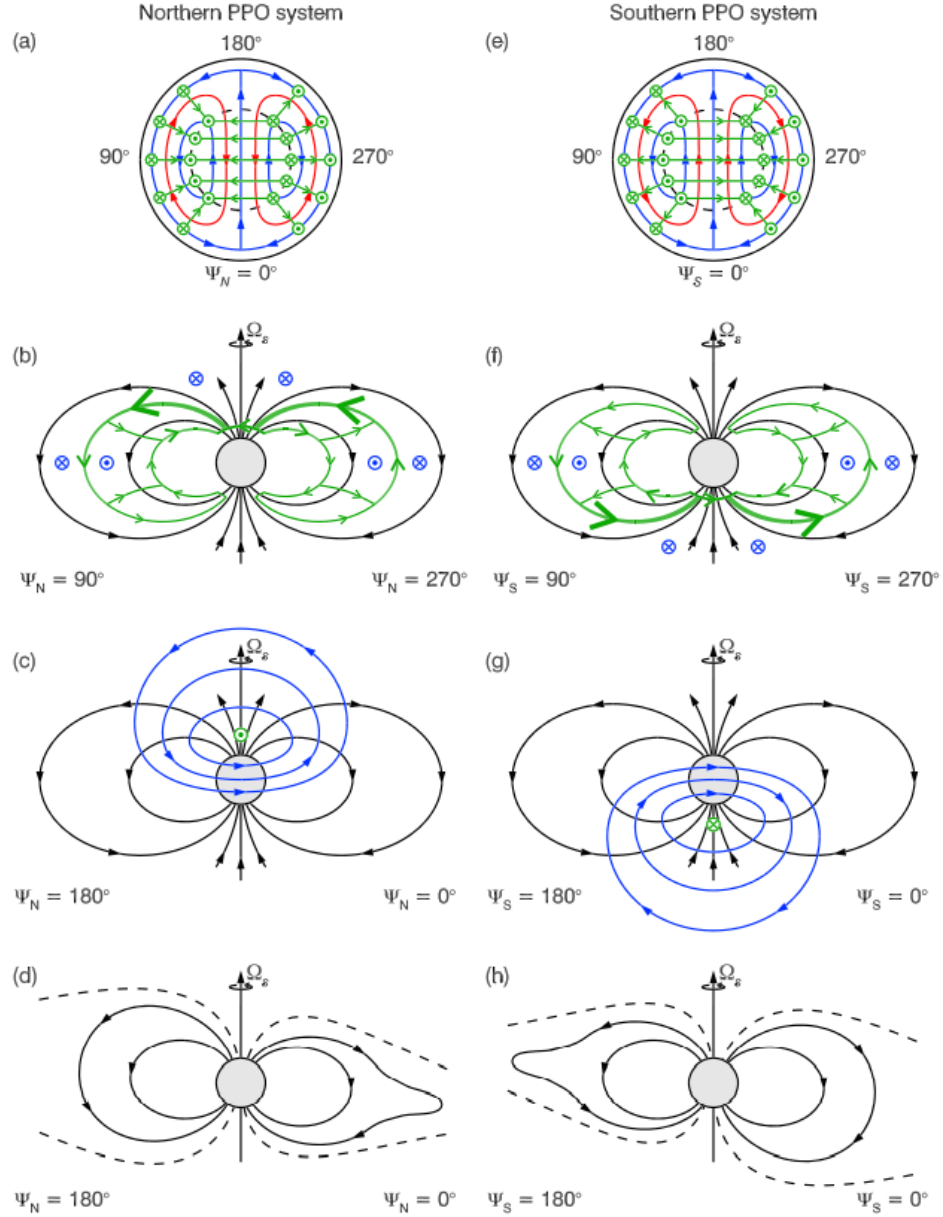
Figure 1.9: Sketches showing the magnetic fields and currents associated with the northern (a) - (d) and southern (e) - (h) PPO systems. The green marks represent the configuration of electric currents, whereas the blue marks represent that of the associated perturbation fields. The dots and crosses inside circles indicate vectors pointing out of and into the page. Panels (a) and (e) show views of the ionosphere from above the north pole and through the planet to the southern ionosphere, where the arrowed red paths represent the associated ionospheric/ atmospheric flow streamlines. The rotation phase angle, $\Psi_{N,S}$, indicates the azimuthal orientation of the northern and southern PPO systems. Panels (b) and (f) show the currents and field perturbations in the $\Psi_{N,S} = 90 - 270°$ meridian, whereas (c) and (g) show the field perturbations in the $\Psi_{N,S} = 0 - 180°$ meridian, where the arrowed black lines indicate the quasi-axisymmetric planetary field on which these perturbations are superposed. Panels (d) and (h) show the overall effect by field perturbations in the $\Psi_{N,S} = 0 - 180°$ meridian plane, where the PPO modulations give rise to the opposite effects on two sides of the planet while the dashed lines indicate the outer boundary of the plasma/current sheet. Taken from Bradley et al. (2020) based on observations and models from Andrews et al. (2010); Provan et al. (2012); Hunt et al. (2015); Cowley and Provan (2017).
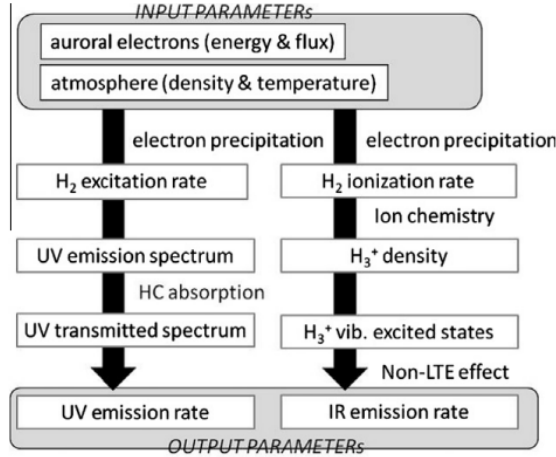
Figure 1.10: Flowchart of auroral emission model which gives UV and IR emission rate depending on two input parameters: particle precipitation and the atmospheric composition and temperature. Taken from: Tao et al. (2011)

1.5 Saturn's Aurora

Auroral electrons in the planet's magnetosphere follow the magnetic field lines connecting into the planet and precipitate into the upper atmosphere where they excite atmospheric particles (hydrogen atoms and molecules) through collision. Aurorae emitted in optical wavebands - infrared (IR), visible and ultraviolet (UV) - are primarily related to the planet's principal atmospheric constituent. Figure 1.10 summarises the process of UV and IR emission whose production rate is dependent of both precipitating electron energy and atmospheric conditions. The electron-excited H atoms and H_2 molecules de-excite to ground state to emit photons in visible and UV wavelengths, dominated by H Lyman- line and H_2 Werner and Lyman bands in the far UV (Gérard et al., 2004). On the other hand, IR emissions are produced by de-excitation of thermally excited H_3^+ as a result of ionisation of neutral H_2 by energetic electrons. A statistical investigation by (Badman et al., 2011) showed UV and IR main oval aurorae are typically driven by the same field-aligned current system, even though UV emissions lack an intense poleward feature detected by Stallard et al. (2008) in the IR.

Plasma, which is confined in the magnetosphere by centrifugal force and forms the magnetodisc, flows following the direction of planet's rotation with flow speeds generally below rigid corotation. Beyond $\sim$3.3 Rs, where the plasma slows from corotation (Wilson et al., 2009) the lagging configuration of the magnetic field introduces an azimuthal component of the field above and below the equatorial plane and requires a radially outward current to flow. This current is closed via field-aligned currents (FACs) connecting to the planet's ionosphere, and equatorward ionospheric currents are associated

with the magnetic curvature (J×B) force to accelerate the subcorotating plasma. This current system transfers angular momentum from the planet to the magnetospheric plasma to attempt to spin it up to corotation and is the source of Jupiter's main auroral oval (Cowley and Bunce, 2001). The equivalent system at Saturn is too weak and low latitude to generate the main emission (Cowley and Bunce, 2003), but strong flow shears in the outer magnetosphere are instead thought to be associated with the main, LT-fixed auroral currents detected there.

Ray and Ergun (2012) pointed out that a lower ionospheric Pedersen conductance at high latitudes gives rise to a reduced magnitude of currents flowing through the ionosphere, and the centrifugal confinement of the magnetospheric plasma at high latitudes results in a lack of current-carrying plasma. The two authors also suggested that the entire electron distribution can saturate into the loss cone via the acceleration region located above the ionosphere. Field-aligned acceleration by parallel electric fields is therefore expected to carry the required current. Studies on terrestrial auroral zone indicated parallel electric fields along the magnetic field lines as the fundamental particle acceleration mechanism (Ergun et al., 1998). Recent studies with Juno's observational data on Jovian main aurora showed strong parallel electric fields plays a role for particle accelerations in order to maintain magnetospheric circuits like at Earth (Clark et al., 2017), but the energy flux is less significant than that produced by a diffuse aurora process with broadband and stochastic characteristics (Allegrini et al., 2017; Mauk et al., 2017), in which Alfven waves are likely to be responsible for converting field energy into auroral particle acceleration (Saur et al., 2018). Both terrestrial and Jovian research give invaluable implications to possible acceleration mechanisms at Saturn, but *in-situ* measurements in the vicinity of the acceleration regions were lacking due to Cassini's limited orbital geometry until its end of mission when the spacecraft made low altitude auroral passes. Particle acceleration of a broadband nature at Saturn was seen while no sufficient magnitude of Alfven wave was found in order to produce the observed accelerated proton populations (Bader et al., 2020). Therefore, Saturn seems to have a similar accelerating regime to Earth, being driven by powerful parallel electric fields, but their exact nature is not fully understood and is a very important topic that requires further investigation.

HST's STIS and ACS cameras have been the main instruments to study Saturn's UV aurora, but the images are of much poorer quality than Jupiter's owing that Saturn is located at twice the distance from Earth's orbit, which results in a halved spatial resolution, and its aurora is a lot dimmer giving a reduced signal to noise. The Saturn's orbit insertion of Cassini provided a combination of various *in-situ* measurements at much
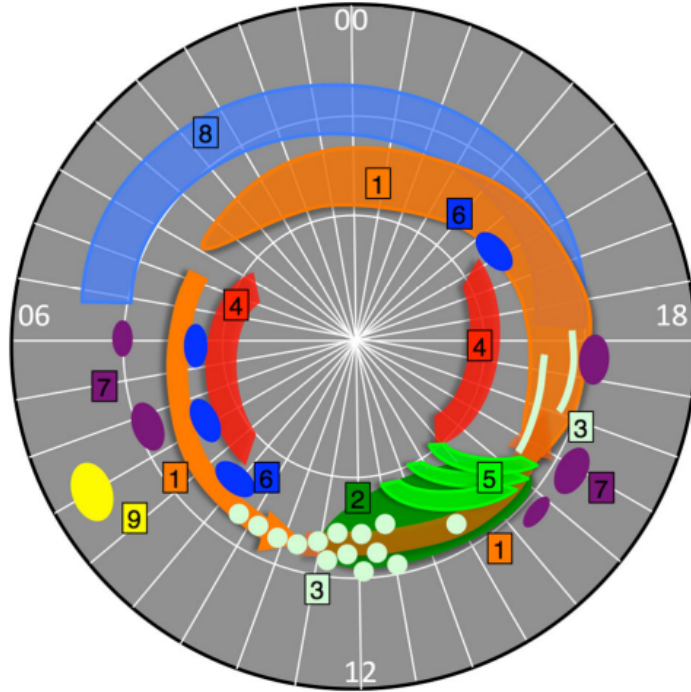
Figure 1.11: Cartoon of various features in Saturn's UV aurora from both HST and Cassini observations. The polar plot displays local time as labelled and the colatitude from 0 (centre) - 30 (outermost ring). 1. Main (ring of) emission; 2. Cusp emission; 3. Small scale spots and arcs; 4. Poleward auroral arcs; 5. Bifurcations; 6. Poleward auroral spots; 7. Signatures of injections; 8. Outer emission; 9. Enceladus footprint. Taken from: Grodent (2015)

wider timescales. One of the most important findings was that Saturn's main auroral dynamics were rapidly enhanced when large solar wind pulses arrived (Crary et al., 2005; Badman et al., 2005). Saturn's aurora consists of multiple signatures of diverse nature and lifetime, as sketched in Figure 1.11. The large variety of auroral features including their possible driving mechanisms has been closely reviewed (Badman et al., 2015; Grodent, 2015), and they are succinctly summarised below categorised basically by their latitudes.

1.5.1 Main Emission

The principal constituent of Saturn's aurora forms a partial ring (though named the main "oval") of multiple separate structures of different sizes. It usually spreads around the poles at both hemispheres within 20° colatitude, and the general morphology contracts (or expands) poleward (equatorward) during active (quiet) solar periods, although this dynamical motion is asymmetric (Grodent, 2015). The northern hemisphere was found to have a smaller oval size but higher emission power than the southern counterpart (Nichols et al., 2008), attributed to the northward offset of the planet's internal

magnetic field (Dougherty et al., 2018). As one can tell from the orange signatures marked "1" in Figure 1.11, the UV main emission is roughly comprised of three components: a narrow corotating arc with the highest brightness starting from pre-dawn sector to, and often past, 12 LT that sometimes continues with a fainter one covering up to pre-dusk which slightly superposes with a much wider arc originating from pre-dawn to pre-dusk. The brightness of the entire main oval can vary from ∼10-100 kR and is directly related to the solar wind ram pressure (Crary et al., 2005; Badman et al., 2005) as mentioned above. The bulk of the UV main emission is found to be highly mobile especially the brightest arc in the dawn-noon sector, rotating with ∼70% of corotation (Grodent et al., 2005), but has been observed to stagnate around noon (Radioti et al., 2017a). It has been suggested that the corotation of accelerated plasma through magnetotail reconnection near midnight (Cowley et al., 2005) or ring current enhancement (Mitchell et al., 2009) could be responsible for producing these main emission arcs. Cassini's UVIS observed a "bunch of grapes" near noon and very narrow arcs in the noon-dusk sector overlapping the main oval (white dots and arcs marked "3") (Grodent et al., 2011), the grapes are proposed to be driven by FACs as a result of magnetopause Kelvin-Helmholtz (KH) waves while the arcs are associated with non-uniform plasma flow in the equatorial plane. Similar features are also observed by the HST in both Saturn's hemispheres and associated with second harmonic ultra-low frequency waves (Meredith et al., 2013).

1.5.2 Inner Emissions

Alternative UV emissions (marked "2" in Figure 1.11) may turn up at the noon sector overlapping the rotating main arc in that region or replacing them, although there is no clear association to the main emissions because these atypical features are only observed occasionally due to the long observing periods required. These features are considered in relation to reconnection either poleward of the cusp or at low latitudes of dayside magnetopause under a southward or northward interplanetary magnetic field, respectively (Bunce et al., 2005; Kinrade et al., 2017). A series of investigations into Cassini's UVIS 2008 observations framed the evolution of the bifurcating arc signatures (marked "5" in Figure 1.11) which are related to low latitude magnetopause reconnection: they started from the main emissions in noon-dusk sector, then the tail gradually develops poleward while the head stays relatively unchanged latitude-wise forming 2 or 3 offset arcs as the centre follows the planet's rotation (Radioti et al., 2011, 2013; Badman et al., 2013). More recently, Lamy et al. (2018) suggested an unexpectedly frequent identification (in about 50% of the images) of recurrent cusp-related emissions

and bifurcations with potential connection with the strong solar wind conditions. Transient spots (marked "6" in Figure 1.11) located at poleward boundaries of the main oval typically in the dawn and dusk-midnight sectors were also highlighted by Radioti et al. (2011) study, and newly reconnected field lines in the magnetotail can be rapidly accelerated back towards the planet (becoming dipolarised) following reconnections and in turn powers the nightside spot features which then develops into the dawnside through subcorotation (Jackman, 2013). The features that are totally isolated poleward from the main oval (marked "4" in Figure 1.11) are mostly faint UV arcs at 80° colatitude in both dawn and dusk sectors and are noted in a recent study of Saturn's northern aurorae by Lamy et al. (2018).

1.5.3   Outer Emissions

There are more spot-like features (purple spots marked "7" in Figure 1.11), at the equatorward boundaries of the main oval, that are not observed frequently because of its short lifetime (several to tens of minutes) and low emission power (<10 kR) (Grodent et al., 2005; Radioti et al., 2009). Based on the brightness distribution of such spot emissions modelled by Radioti et al. (2013), these features were found to be behave as energetic particle injections (Grodent, 2015). Equatorward of the main oval on the top half of the polar projection, there sits an outer emission arc (marked "8" in Figure 1.11) typically at 20° colatitude on both. The emissions again are faint but observed by HST (Grodent et al., 2005; Lamy et al., 2018), and later UVIS observations indicates that they can map to 9 Rs in the nightside magnetosphere and rotates with the planet at 70% corotation just like the main emissions (Grodent et al., 2010; Radioti et al., 2017b). The potential driving mechanism was suggested to be the super-thermal electrons (at 7-10 Rs) in the night half or a nightside net upward current layer (Schippers et al., 2008, 2012).

1.5.4   Enceladus Footprint

Unlike Jupiter where the footprints of its moons are visible in UV aurora, the footprint of Saturn's moon Enceladus was only observable with Cassini's UVIS because of the weak intensity with the UV spot only visible in a small minority of observations of this region. Three consecutive observations of Saturn's northern polar region on 26 August 2008 revealed the Enceladus footprint of different emission magnitude, probably indicative of variable volcanic plume activity on the Saturn's moon (Pryor et al., 2011). The footprint counts as one of the faint equatorward spot-like signatures briefly summarised

above.

1.5.5 Quasiperiodic Flashes

Auroral flashes were first observed in HST images by Radioti et al. (2009), who indicated a potential association with energetic particle injections. Badman et al. (2012a) identified upward bursts of light ions (100-360 keV), energetic electrons (hundreds of keV) and broadband whistler wave during an interval of ∼1 h bifurcation signatures in Saturn aurora. Radioti et al. (2013) proposed a relation between quasiperiodic (QP) ∼1 h auroral bifurcations and magnetopause reconnection supported by the observation of cold dense electrons and "stepped" ion energy-latitude dispersions. Meredith et al. (2013) examined small-scale transient features (10-30 min duration) with HST images for both northern and southern UV aurora and suggested they were produced on newly-opened field lines and were not conjugate between hemispheres. Mitchell et al. (2016) reported another observation of repeated auroral intensifications at high latitudes and showed the accompanying ∼1 h pulsations in magnetic field, auroral hiss power and electron and ion energies, also suggesting recurrent reconnection events at the magnetopause as the driving mechanism. They also pointed out the rapid rotation (through 6 hours in LT from noon to dusk) of these auroral arcs as well as the involvement of the polar cap region.

Two statistical surveys (Roussos et al., 2016; Palmaerts et al., 2016) of the ∼1 h QP electron injection events (with hundreds of keV up to several MeV of energy) suggested a variable interpulse period (∼40-90 min) as well as a dawn-dusk asymmetry with ∼80% of the events identified in the duskside, indicative of being dominated by reconnection sites in the duskside. A survey of low-frequency waves (of periods 10-60 min) by Pan et al. (2021) showed an intense population of magnetic fluctuations extending from the pre-noon sector to dusk, but a clear local minimum in the distribution was seen at ∼18 LT. Bader et al. (2019) examined all available UVIS auroral sequences and also found an obvious location bias on the duskside for ∼1 h auroral flashes. They suggested a closed field configuration as the QP pulsation event was observed in both hemispheres, and a possible internal driving mechanism – a "drizzle" of small-scale magnetodisc reconnection events predominantly in the dusk flank, contributing to plasma circulation in this region.

The reconnection "drizzle" was proposed by Delamere et al. (2015), who examined Cassini MAG data for identified current sheet crossings in Saturn's magnetosphere and found large-scale reconnection events are insufficient to support the observations of large B_θ variations as well as frequent negative measurements in B_θ. They concluded

that plasma can be lost through reconnection "drizzle" (a patchy network of small-scale reconnection sites), which are found predominately on the dusk flank. Studies of the dayside magnetodisc by Guo et al. (2018a,b) showed that magnetodisc reconnections can occur on the dayside, and, with potential corotation with the planet, the existence of internally driven "drizzle-like" dayside magnetodisc reconnection casts a reconsideration of the balance between internal and external drivers that control magnetic reconnection especially on the dayside.

In addition, the magnetospheric box model by Yates et al. (2016) showed the ~1 h QP magnetic field fluctuations are second harmonic Alfven waves standing between the northern and southern ionospheres in the outer magnetosphere and modulated by the rocking of Saturn's magnetosphere. Yao et al. (2017) proposed another possible link with wave characteristics – pulsating FACs generated by travelling Alfven waves – when investigating a near-noon auroral feature of 30 min duration. Furthermore, Rusaitis et al. (2018) suggested that solar wind periodic density structures could propagate into Saturn's magnetosphere and show up in the MAG data. The authors found these field perturbations spreading across both dayside and nightside with Alfvenic characteristics and proposed that the driving mechanisms were standing Alfven waves driven from solar wind (Rusaitis et al., 2018, 2021).

1.6   Content of This Thesis

This research focuses on the HST observations of Saturn's aurora during 2013-2017 to search for potential quasi-periodic auroral flashes and describe as well as statistically analyse their characteristics, combined with magnetic field measurements using Cassini's magnetometer. Section 2 will introduce the basic operation of different instrumentations, the image/data processing techniques and the origin of uncertainties. Several examples of identified auroral flashes with either similar or contrasting features will be presented in Section 3, including an overview of the occurrence of such events. Magnetometer data for the time list of identified auroral flashes will be shown in Section 4, specifically analysing the indications of field perturbations and whether these pulsed events are correlated with transient flashes. Section 5 will compare the results from this research to previous studies mentioned in Section 1.4.5, and open topics such as the dependence of spatial location, the periodicity, the conjugate field configuration, and the potential powering dynamic process of these quasi-periodic energetic events will be discussed.

2 Instrumentation and Methods

2.1 Hubble Space Telescope

The Hubble Space Telescope (HST) was deployed into the low Earth orbit (LEO, $\sim$540 km) in 1990 and has been providing massive astronomical data of immense importance. Two of its instruments, Advanced Camera for Surveys (ACS) and Space Telescope Imaging Spectrograph (STIS), are widely used for observation of outer planet's UV aurora. The ACS is a third-generation instrument with only the Wide Field Channel (WFC) and the Solar Blind Channel (SBC) available due to previous failures of the other three channels. The STIS is a second-generation spectrograph for the telescope, with improved performance compared with its predecessor. It has two photon-counting Multianode Microchannel Array (MAMA) detectors, which has a field of view of 25×25 arcsec^2, to record UV and a charge-coupled device (CCD) to cover visible bands.

This study uses images from HST 2013, 2014, 2016 and 2017 campaigns to identify short-lived brightenings on Saturn's northern UV aurora. The 2013 images came from the ACS's SBC and were filtered by "F115LP" and "F125LP", which are effectively the MgF2 (1150-2000 Å) and CaF2 (1200-2000 Å) filters respectively. The other images were taken by the STIS and mostly filtered by "F25SrF2" (1250-1900 Å), which forbids geocoronal Lyman- emission (1216 Å), while the 2014 campaign also includes the ones using "25MAMA" (1150-1900 Å), which is preferred when sky background is not significant and hence provided much greater dayglow contamination to the images.

Because of the use of different instruments and filters, the integration time for subexposures from different years varies – 100 sec for 2013 images, between 270 and 420 sec for 2014 images, 450 sec for 2016 images, and 500 sec 2017 images, respectively. It is noticeable that the most outstanding uncertainties when calculating time differences involve the time of light travel from the planet to the camera and the integration time of each subexposures.

All images used in this study are processed using the pipeline developed at Boston University, including dark count subtraction, flat-fielding, correction for geometric distortion, and subtraction of an empirical background (Clarke et al., 2009). The photon counts are converted to units of kiloRayleigh (kR), which is a measure of photon flux, using the filter-specific conversion factors determined by Gustin et al. (2012), and assuming a colour ratio (ratio of intensity in unabsorbed and absorbed wavebands) of 1.1. A Rayleigh is defined as a column emission rate of 10^{10} photons per metre squared per column per second. The images are projected onto a planetocentric polar grid with spatial resolution 0.25×0.25 deg (longitude $\times$ latitude), which corresponds to a resolution

on the planet of $\sim250 \times 250$ km.

2.1.1 Flash Identification

The duration of transient flashes in Saturn's UV aurora is of order 10-30 min with a typical periodicity of ~1 h as pointed out in previous investigations (Badman et al., 2013; Radioti et al., 2013; Mitchell et al., 2016). More recently, Bader et al. (2019) showed statistically with Cassini UVIS that flashes had a typical duration of <20 min and power up to 50% of the total auroral power. These observed characteristics were used to guide the identifications of flashes in this study. Hence in this study we aimed to look for auroral features

1. with high enough brightness that can be easily picked out above the background emission,

2. of sufficient size to be well distinguished in the polar projected images,

3. whose lifetimes lie between several and 20 min,

4. that are likely to re-appear with a typical ~1 h gap between each occurrences.

Moreover, one would expect to observe across several subexposures the minor evolution of the short-lived events in only the 2013 images because of much shorter integration times available than the other years. Sequences of images were manually examined for evidence of bright flashes above the background emission (1). A qualitative judgement was applied whether a transient was noise or a sufficiently coherent to be a flash (2) and which appeared in several consecutive images (3) and, when observing cadence permitted, in consecutive HST orbits (4).

2.1.2 Map of Distribution

These transient auroral features may take variable shapes and non-fixed locations of occurrence as pointed out by previous studies (Badman et al., 2013; Radioti et al., 2013; Bader et al., 2019), hence constructing a map of distribution ("heat map") representing their overall latitude and local time dependence would enable us to find links to particular energetic events observed in *in-situ* measurements.
The duration of flashes are generally longer than the image integration times, so an averaged pseudo-image was hence created by adding the image frames containing well

distinguished transient features and averaged by the number of frames N:

$$< I >= \sum_N I/N. \tag{2.1}$$

This is named a pseudo-image because it does not show what was captured by the camera but an averaged distribution of a transient flashing event across several subexposures. More importantly, due to the fast rotation of Saturn, it is likely that these auroral features may change position even within a matter of minutes, the pseudo-image obtained in this step depicts the full evolution of a flash. However, the peak intensities will be lowered after averaging for those dynamic flashes. It is also important to consider that the flash region has background brightness or may already show other types of features (e.g., the main oval or the inner arcs), we hence need to subtract the "background":

$$I_{flash} =< I > -I_{background}. \tag{2.2}$$

These "background" intensities are persisting and not changing dramatically over each HST exposure, so chronologically the subexposure before the flashing frame is used as the "background" frame. But this, of course, does not take into account the rotating background across several subexposures (of order several tens of minutes). To construct a heat map for every flashing event, the sector containing the flash morphology was extracted by setting all pixels outside this sector to zero as we only want to map the transient features. A threshold intensity is chosen explicitly for every event in order to further subtract the background pixel values:

$$I_{heat} = I_{flash} - I_{threshold}. \tag{2.3}$$

In this case the threshold intensity was determined by the lowest intensity value within the flash region. Although the threshold intensity can sometimes be smaller than a minority of those bright background features which survived the previous background subtraction process, it is a trade off for maintaining the complete flash morphology. The non-zero pixels in our intensity array, I_{heat}, were then assigned to the same value and plotted onto our heat map as we focus on the location of occurrence here instead of the actual intensity value.

2.2 Cassini

The Pioneer 11 spacecraft was the first to discover Saturn's magnetosphere in 1979, followed by Voyager 1 one year later. Those fly-by missions, in which spacecraft stayed in Saturn's magnetosphere for no more than several days, could not allow scientists to take a closer look at the true nature of the giant invisible bubble until the arrival of Cassini spacecraft (2004 - 2017). The measurements from Cassini have revealed many puzzles, e.g., Enceladus' water and ice plumes are the main source of Saturn's E-ring and leaves a fingerprint on the magnetospheric aurora.

2.2.1 Footprint

NASA's SPICE data, which are also known as "kernels", consist of navigation and other ancillary information on precision observation geometry. Breaking the letters down it stands for "Spacecraft ephemeris", "Planet" (or, generally speaking, location of any target object), "Instrument information", "C-matrix" (that is, orientation information), and "Event information". Cassini's orbital locations corresponding to the entire time sequence of HST images examined in this study are obtained using SPICE with the Kronocentric Solar Magnetic (KSMAG) coordinates and projected on top of the HST polar plots. Saturn is centred at the origin with the Z axis pointing along the magnetic dipole moment and the X axis directed sunward. The duskward Y axis is the right-handed cross product between Z and X axis. *In-situ* measurements enable us to look for connections between the observed QP flashes and any large-scale or small-scale signatures. The mapping from the spacecraft position was performed using the Burton et al. (2010) model of the internal field, plus the Bunce et al. (2007) model of the ring current for a standard magnetopause standoff distance of 21 Rs. This model does not include any azimuthal component of the field, i.e., no offset in LT between the spacecraft and its mapped ionospheric footprint. Fig 2.1 shows the variation of the Bunce and Burton model of Saturn's magnetosphere compared to the UCL model (Sorba et al., 2019) for the northern hemisphere during solar compression (Fig 2.1a) and rarefaction (Fig 2.1b). The models show good alignment around noon until incrementally >10 Rs in the north or >15 Rs in the south where the discrepancy can reach ∼2° in colatitude for both solar wind conditions.

2.2.2 Magnetometer

Cassini had two magnetometers: a fluxgate magnetometer (FGM) and a vector helium magnetometer (V/SMH) which failed after arriving at Saturn in 2005. The FGM is
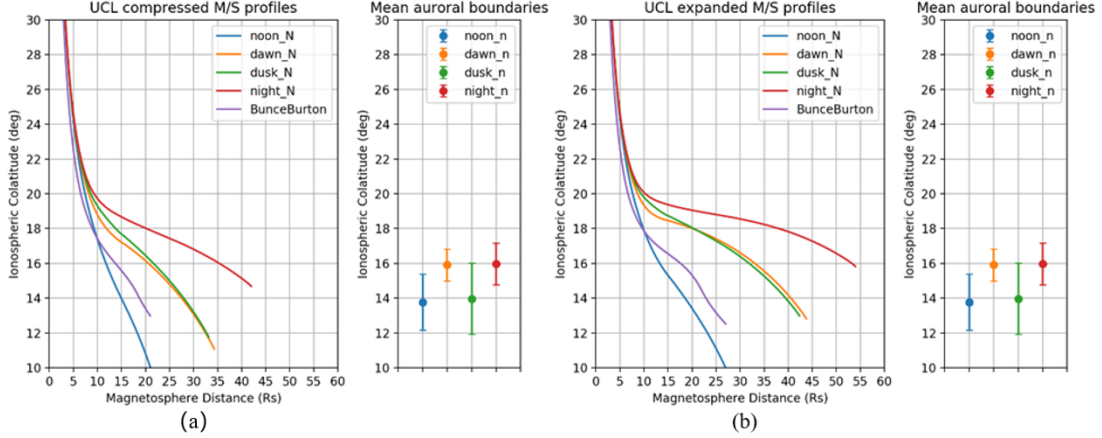
Figure 2.1: Bunce et al. (2007) and Burton et al. (2010) model of Saturn's magnetosphere compared to the UCL model (Sorba et al., 2019) for northern hemisphere during solar compression (left) and rarefaction (right). Image Courtesy: J. Kinrade.

designed for making high-frequency (from 0 Hz to at least 30 Hz) 3-D vector measurements of the magnetic field using its three orthogonal ring core fluxgate sensors. The FGM can operate over 4 dynamic ranges: ± 40 nT range at 0.004 nT resolution (R0), ± 400 nT range at 0.048 nT resolution (R1), ± 10000 nT range at 1.2 nT resolution (R2), and ± 44000 nT range at 5.4 nT resolution (R3). It is hence noticeable that small field perturbations could not be precisely detected by the MAG when it is operating in R3 mode. The FGM is mounted at the halfway of an 11 m boom whereas the V/SMH is mounted at the end in order to minimise the influence of spacecraft-generated field variations. The raw data from the FGM are first pre-processed to extract from the telemetry packets, including removing corrupted data and correcting data times, then calibrated using the spacecraft rotation, and finally rotated onto various geophysical coordinates. All data sets are publicly available on NASA's Planetary Data System, and the processing above were all performed by Imperial College. In this study, Cassini's calibrated and 1 min averaged MAG data corresponding to the time sequence of HST images is examined in search for field perturbations particularly on the duskside where QP flashes are found. The Saturn-centred coordinate system - Kronocentric spherical coordinates (KRTP) - was used, where the radial (R) component points radially from the Saturn's centre to the spacecraft, the azimuthal (ϕ) component is parallel to kronographic equator and positive in the direction of corotation, and the southward (θ) component completes the right handset.

3 Observations of Transient Auroral Flashes in HST UV Images

3.1 Typical Flash Examples

We examined all HST auroral images from campaigns in 2013, 2014, 2016, and 2017 to identify flashes following the criteria described in Section 2.1.1. From these, 29 flashes were detected, in observations on 21 separate days. Four examples of image sequences of typical flashes are shown in Figures 3.1-3.4 (2013-110, 2013-111, 2017-66, 2017-239, respectively). The integration times are 100 sec for 2013 images and 500 sec for 2017 images respectively. In the figures, panel (a) shows the image frame before a transient feature was observed, panel (b) shows the frame during the flashing event, and panel (c) after the event. The yellow arrows in these figures highlight the location of each identified flash, all in the duskside. These four example flashes have a duration of 11 min (2013-110 and 2013-111), 16.7 min (2017-066) and 8.3 (2017-238) min, respectively. The flashes in Figures 3.1 3.2 and 3.3 show the flash in the duskside occurred while a main auroral arc, of variable intensity, was present in the dawn-noon or/and the dusk-midnight sector. Figure 3.4 shows the flashes occurred with very faint/no main aurora present in any other LT. Figure 3.3 also shows a persisting, bright stripe auroral feature which can be related to the duskside inner emissions (Lamy et al., 2018; also appears in Figure 3.5 and Figure A.7 and A.8). The flashes in Figure 3.1b and 3.2b are of arc shapes extending for 3 hours in LT while the other two have their main morphology concentrated at 15 or 18 LT. These four examples all show that flashes sit in the duskside poleward of $20°$ colatitude, and they tend to be static in terms of their spatial locations over the interval of exposures (of few minutes integration time) rather than rotating in either direction.

The flashes were not detected in the midnight-to dawn or dawn-to-noon region of main aurora, perhaps because in the conditions of high main auroral powers they could not be detected above the dynamics. However, they were also not detected in this region when the main emission was faint.

Figure 3.1: HST images of Saturn's northern hemisphere in polar projection for the frames before (a), during (b), and after (c) the 2013-110 event. The yellow arrow in (b) indicates the identified transient feature. 0-40° colatitude range was extracted hence the innermost ring in every plot stands for 10° colatitude (or 80° latitude) and each two rings are spaced by an increment of 10°. The longitude is represented in local hour starting from 0 at the top anti-clockwise, hence the dawn is at 6 LT, noon at 12 LT and dusk at 18 LT. The exposure time for the images is 100 sec.
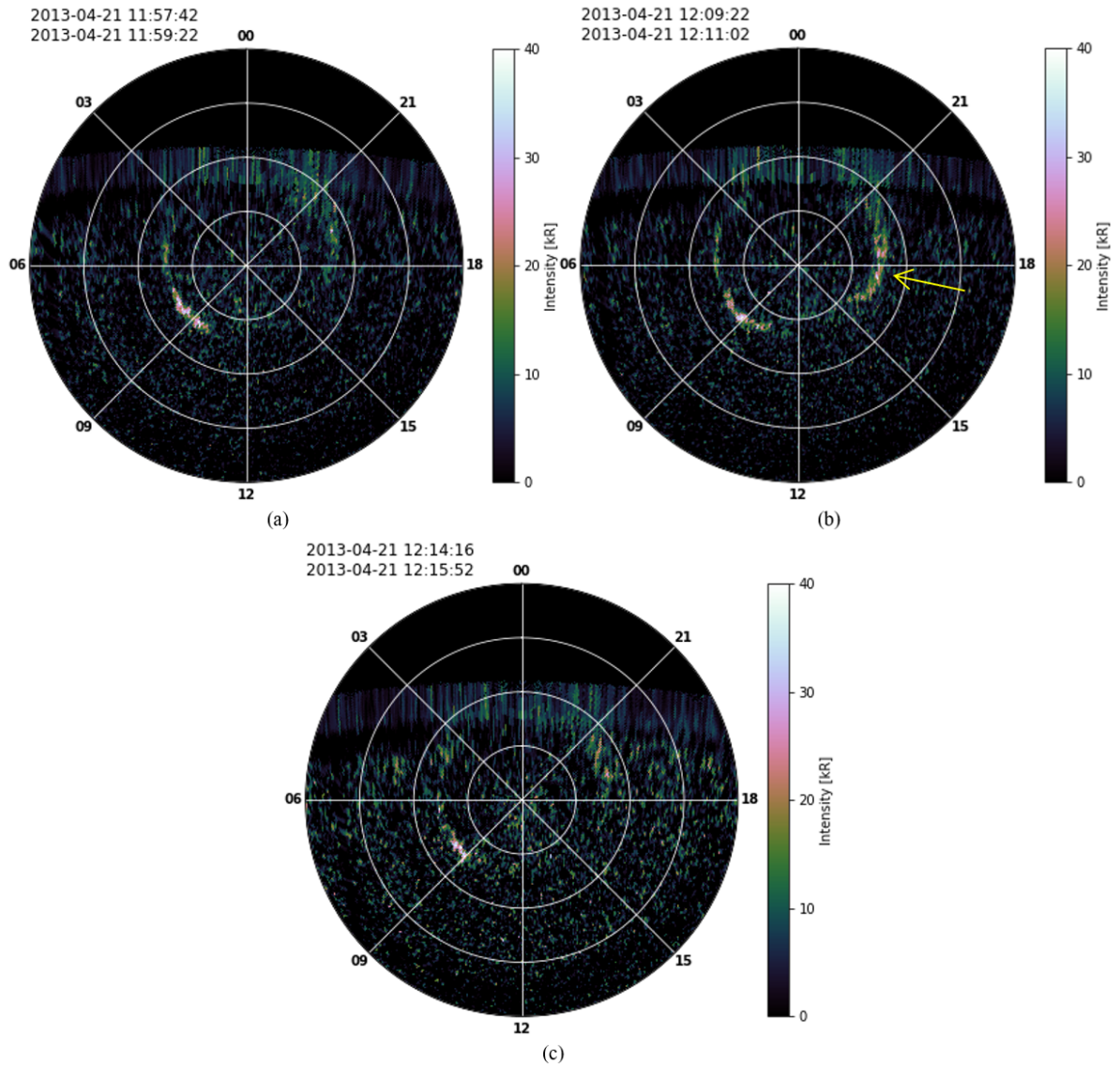
Figure 3.2: HST images of Saturn's northern hemisphere in polar projection for the frames before (a), during (b), and after (c) the 2013-111 event. The yellow arrow in (b) indicates the identified transient feature. 0-40° colatitude range was extracted hence the innermost ring in every plot stands for 10° colatitude (or 80° latitude) and each two rings are spaced by an increment of 10°. The longitude is represented in local hour starting from 0 at the top anti-clockwise, hence the dawn is at 6 LT, noon at 12 LT and dusk at 18 LT. The exposure time for the images is 100 sec.
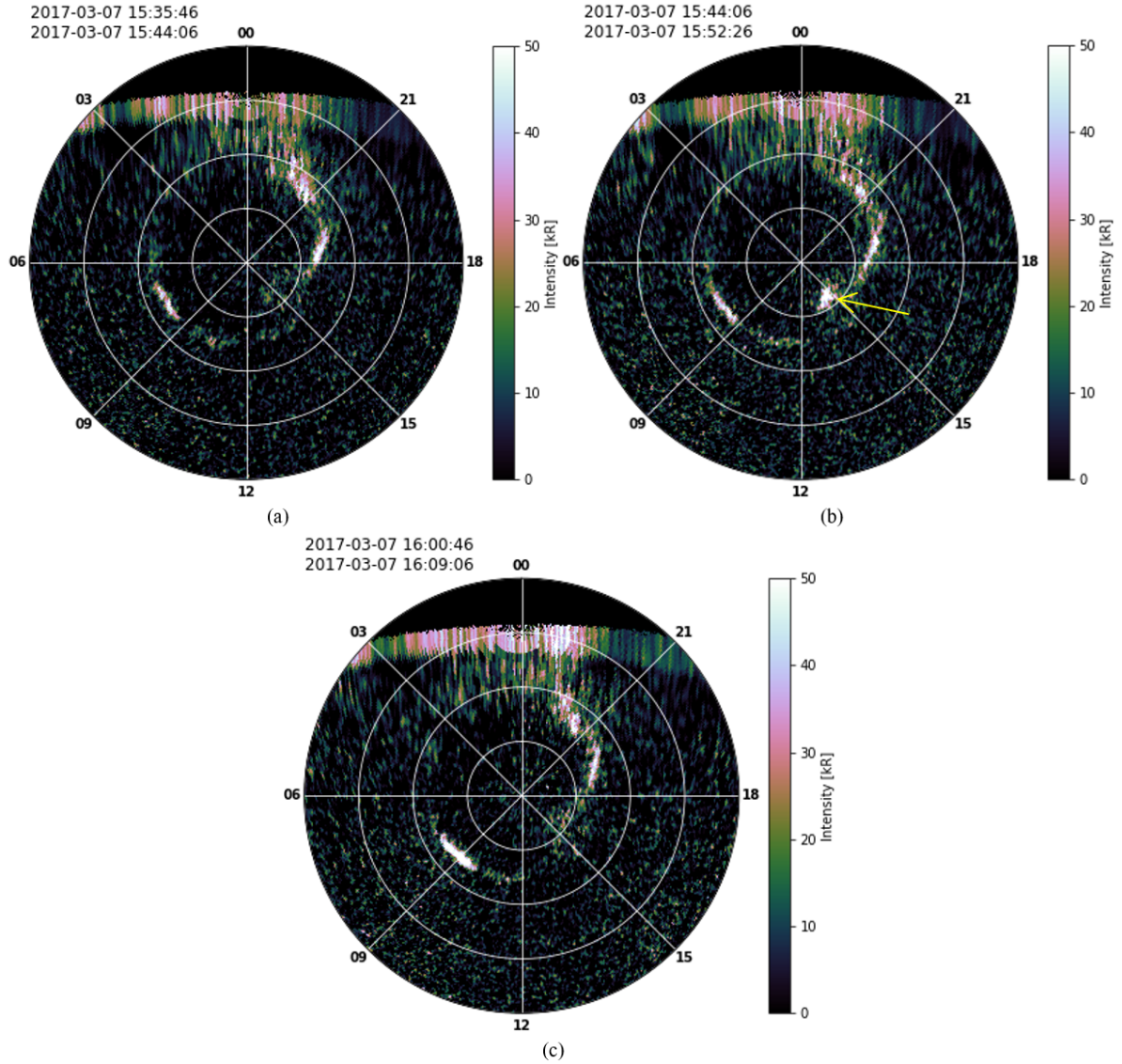
Figure 3.3: HST images of Saturn's northern hemisphere in polar projection for the frames before (a), during (b), and after (c) the 2017-066 event. The yellow arrow in (b) indicates the identified transient feature. 0-40° colatitude range was extracted hence the innermost ring in every plot stands for 10° colatitude (or 80° latitude) and each two rings are spaced by an increment of 10°. The longitude is represented in local hour starting from 0 at the top anti-clockwise, hence the dawn is at 6 LT, noon at 12 LT and dusk at 18 LT. The exposure time for the images is 500 sec.
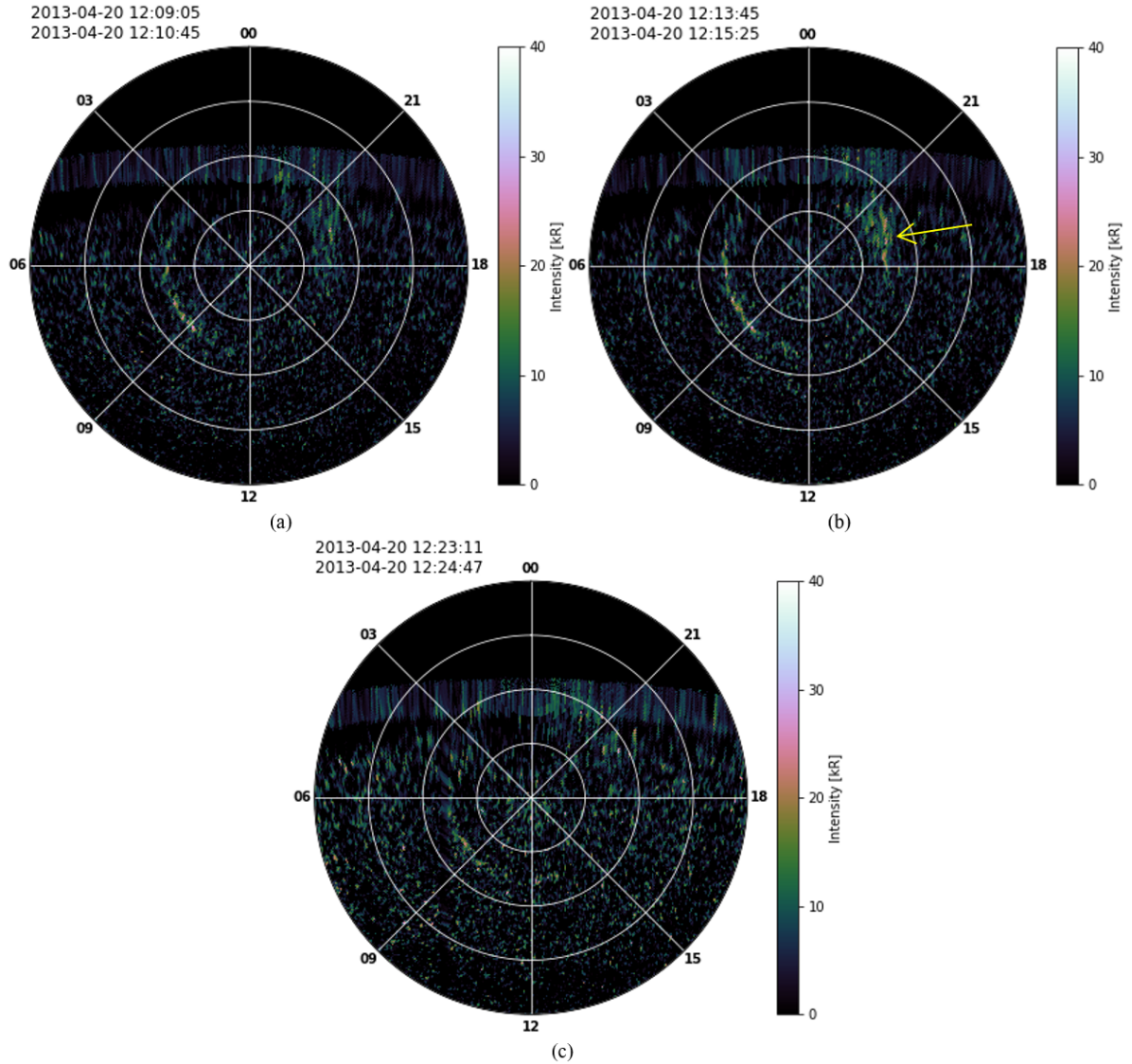
Figure 3.4: HST images of Saturn's northern hemisphere in polar projection for the frames before (a), during (b), and after (c) the 2017-238 event. The yellow arrow in (b) indicates the identified transient feature. 0-40° colatitude range was extracted hence the innermost ring in every plot stands for 10° colatitude (or 80° latitude) and each two rings are spaced by an increment of 10°. The longitude is represented in local hour starting from 0 at the top anti-clockwise, hence the dawn is at 6 LT, noon at 12 LT and dusk at 18 LT. The exposure time for the images is 500 sec.
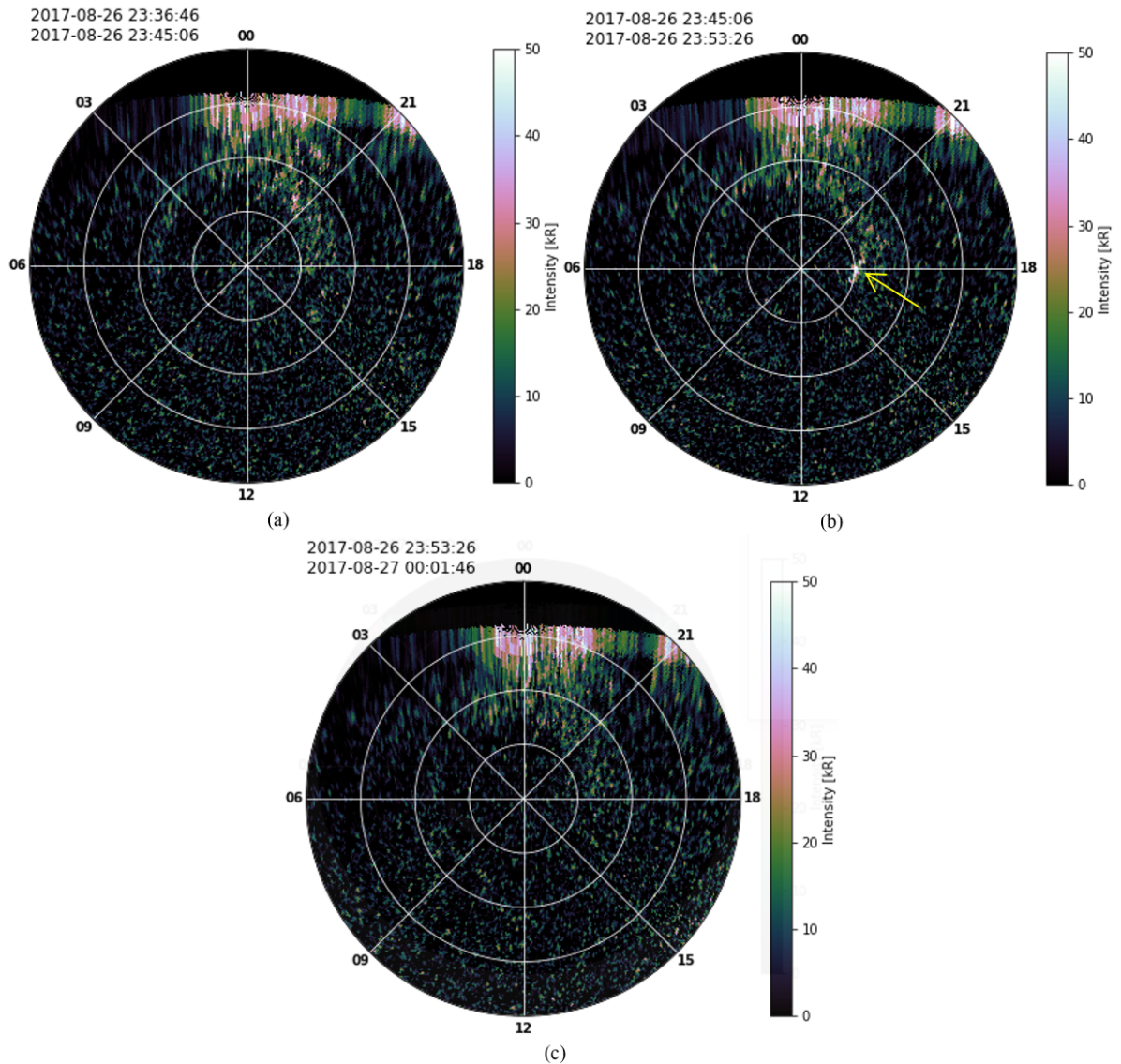
3.2 Atypical Flashes: Outlying and Rotating

Figures 3.5-3.7 show further examples of flashes (2014-100 and two events in 2016-232) with rather different characteristics. The yellow arrow in the figures indicates the identified transient feature while the blue arrow indicate the persisting feature near the transient flash. The exposure times for the images shown here are 270 and 420 sec for 2014 and 450 sec for 2016. The figures show that these flashes can sometimes be fast evolving either following (Figure 3.5a-3.5b) or countering (Figure 3.7b-3.7c) the direction of corotation, and can occur at very late local hour - $\sim$21 LT (Figure 3.6b). All these examples shown here have much higher intensities as opposed to the those typical flash examples (Figure 3.1-3.4), suggesting more violent processes in the magnetosphere in these cases.

In the first example, 2014-100 (Figure 3.5), the flash moves from 12-18 LT (in Figure 3.5a) to 15-21 LT (in Figure 3.5b) between the two subexposures. The leading edge was moving 25% of corotation. In the second event in 2016-232 (Figure 3.7), the flash rotated from 16-20 LT (Figure 3.7b) to 13-17 LT (Figure 3.7c) and 5° poleward, then sat on top of a portion of the main aurora at 15 LT and 10° colatitude. The edge was moving 25% of corotation speed as well but in the opposite direction of corotation contrast to the previous example (2014-100, Figure 3.5). In both fast-evolving flashes, a persisting (duration longer than HST observing interval) feature near the flash was seen, indicated by the blue arrow, at dusk (Figure 3.5) and noon (Figure 3.7). Besides, both of them were seen, in images with similar time integrations, when the main auroral oval were either quiet (Figure 3.5) or active (Figure 3.7). This further shows that transient auroral flashes are more localised and can be independent of changes in the auroral dynamics in a global scale.
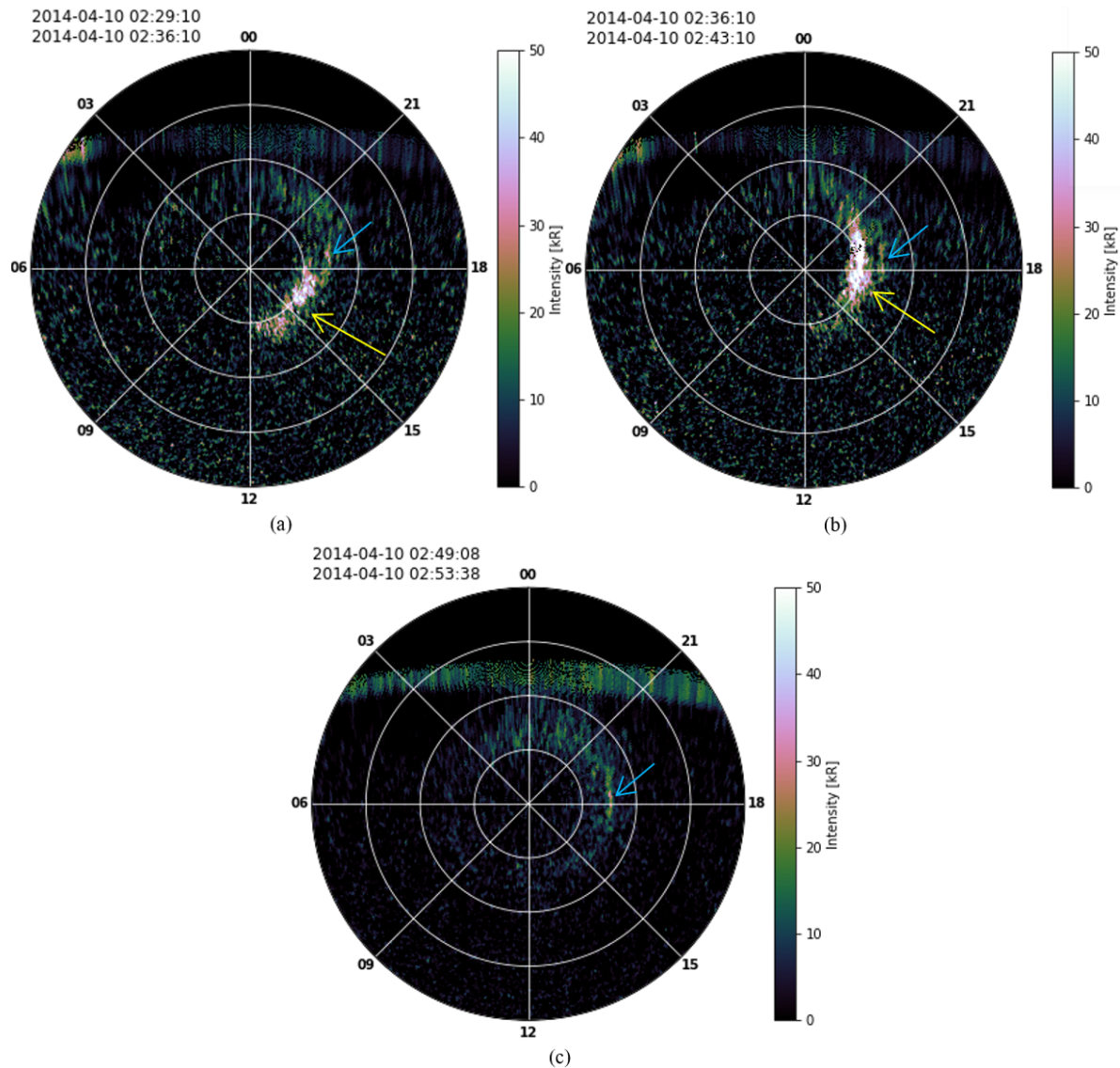
Figure 3.5: HST images of Saturn's northern hemisphere in polar projection for the frames during (a and b), and after (c) the fast rotating 2014-100 event. The yellow arrow in (b) indicates the identified transient feature while the blue arrow indicate the persisting feature near the transient flash. 0-40° colatitude range was extracted hence the innermost ring in every plot stands for 10° colatitude (or 80° latitude) and each two rings are spaced by an increment of 10°. The longitude is represented in local hour starting from 0 at the top anti-clockwise, hence the dawn is at 6 LT, noon at 12 LT and dusk at 18 LT. The exposure times ranges from 270-420 sec.
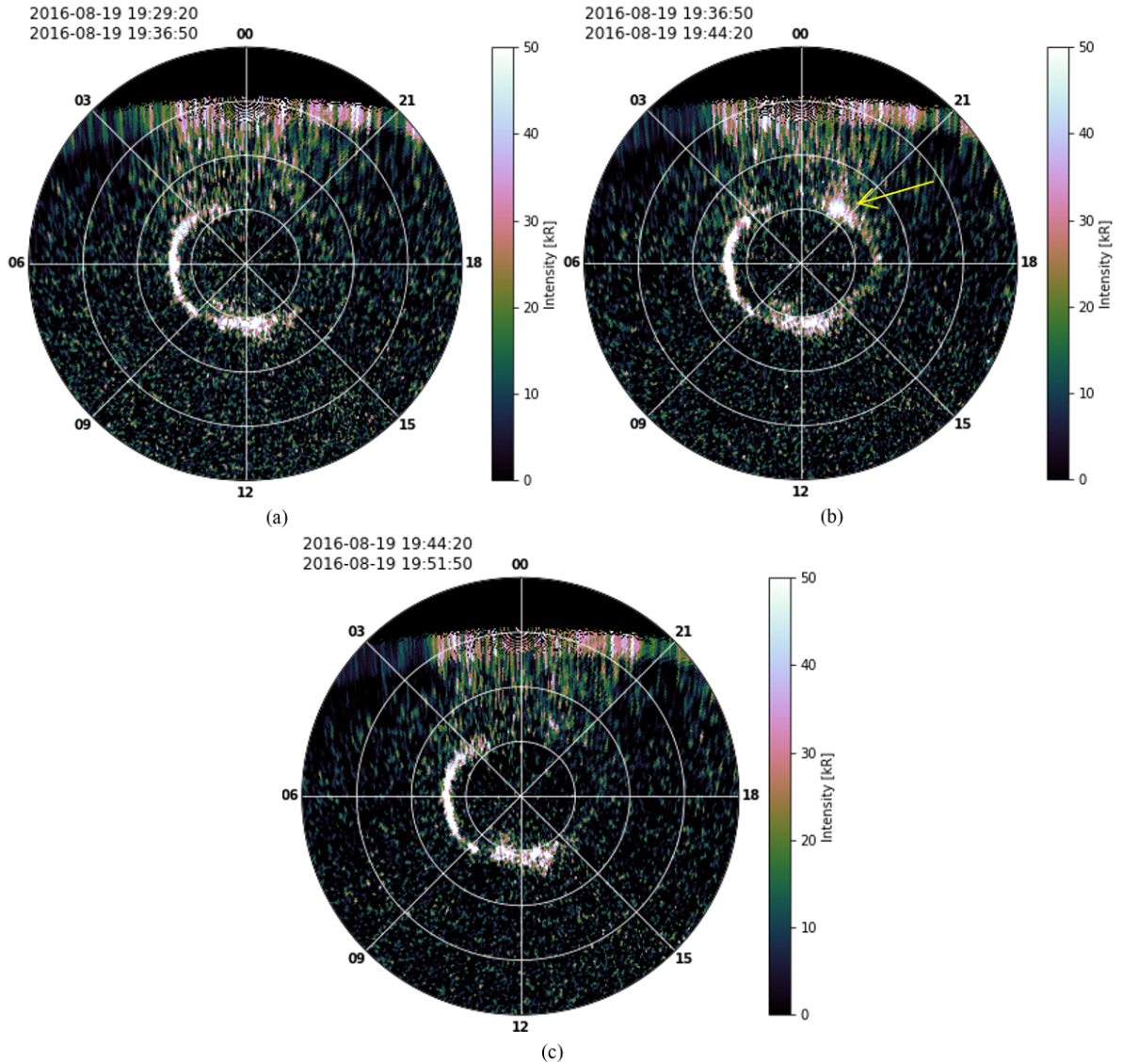
Figure 3.6: HST images of Saturn's northern hemisphere in polar projection for the frames before (a), during (b), and after (c) the first event in 2016-232. The yellow arrow in (b) indicates the identified transient feature. 0-40° colatitude range was extracted hence the innermost ring in every plot stands for 10° colatitude (or 80° latitude) and each two rings are spaced by an increment of 10°. The longitude is represented in local hour starting from 0 at the top anti-clockwise, hence the dawn is at 6 LT, noon at 12 LT and dusk at 18 LT. The exposure times of the images are 450 sec.
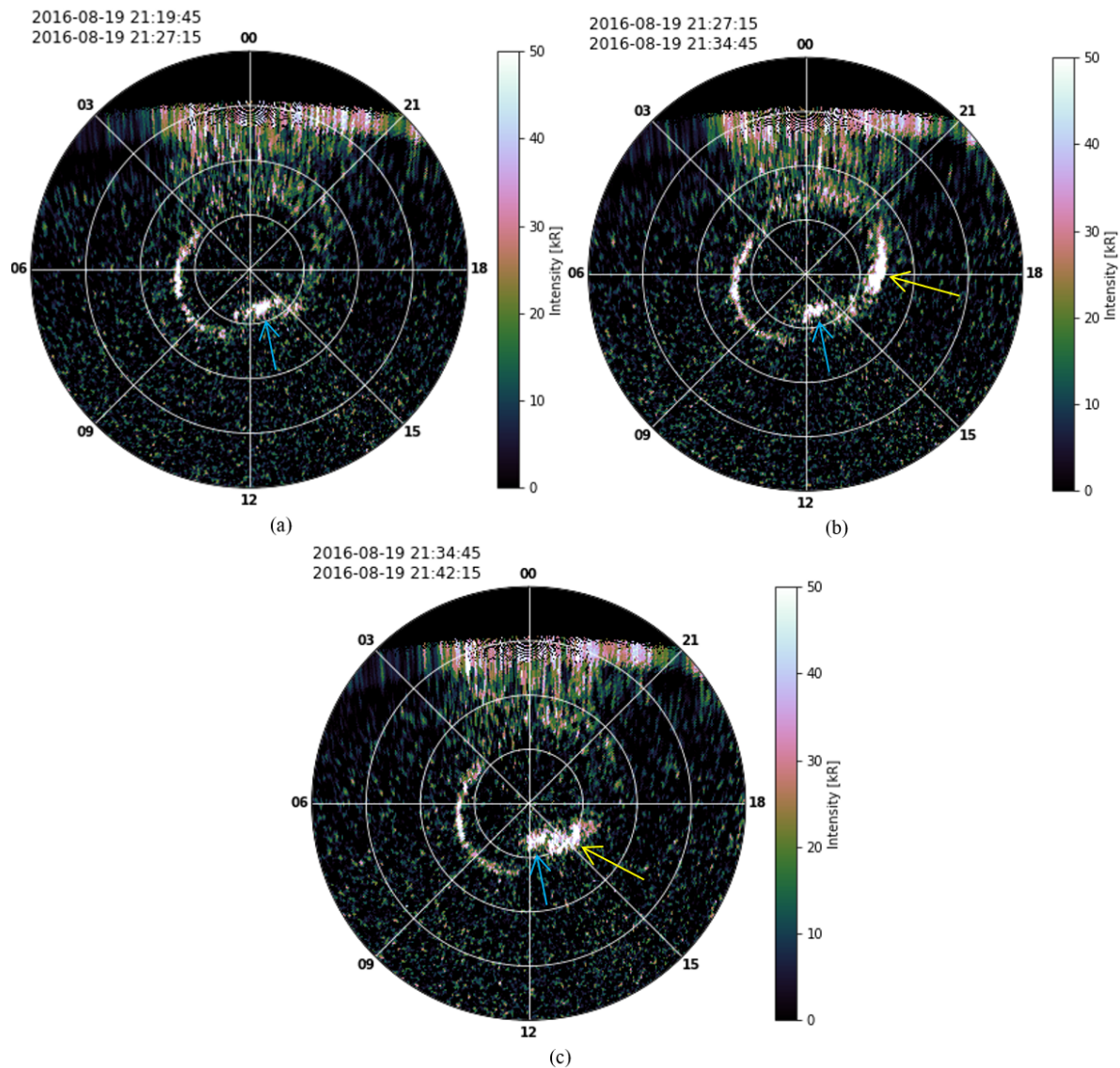
Figure 3.7: HST images of Saturn's northern hemisphere in polar projection for the frames before (a) and during (b and c) the second (fast rotating) event in 2016-232. The yellow arrow in (b) indicates the identified transient feature while the blue arrow indicate the persisting feature near the transient flash. 0-40° colatitude range was extracted hence the innermost ring in every plot stands for 10° colatitude (or 80° latitude) and each two rings are spaced by an increment of 10°. The longitude is represented in local hour starting from 0 at the top anti-clockwise, hence the dawn is at 6 LT, noon at 12 LT and dusk at 18 LT. The exposure times of the images are 450 sec.

3.3 Summary of Transient Flashes

We examined 36-day observations consisting of, in total, 548 images of Saturn's northern aurora taken by the HST in 2013-2017 and identified 29 transient flashing episodes (summarised in Table 1) over 21 different days. Multiple flashing events in a row, in consecutive HST orbits, were observed on 6 occasions, and we found these consecutive events occur at similar spatial locations (both local time and latitude): see 2013-111, 2013-140, 2014-145, 2016-181, 2017-238 and 239 in Table 1, except for one obvious counterexample in 2016-232 (Figure 3.6 and 3.7) when the flash location shifted against the direction of corotation from near the midnight towards the afternoon sector between two observations separated by ∼1 h 45 min. The rare opportunities of exposures in consecutive HST orbits enabled us to find these recurrent (quasiperiodic) flashes with a variable periodicity between 60 and 90 min although the uncertainty can be several minutes due to the time length of each subexposure. It is likely that the other flashes were also quasi-periodic but this cannot be confirmed with the limited imaging available. The images from 2013 had integration times of ∼2 min each whereas the 3 other years had longer integrations, on average ∼8 min. The flash duration was calculated based on image time tags to show in how many images frames every flash was present. Hence the periodicity and lifetime can differ in either direction, that is, the duration calculated for every flash is of order of the picture's exposure time. Hence we found the lifetimes of these transient features to be ∼5-13 ± 2 min for 2013 and ∼5-17 ± 8 min for the 3 other years.

Figure 3.3 shows the peak (orange triangles) and mean (orange dots) intensities of the flashes, compared to the mean intensity of the "background" frame (same spatial region but in the subexposure frame just before the flash was identified). The peak brightness ranges vastly and randomly from less than 30 to 151 kR (with a median 54 kR), whilst their mean intensities mostly lie below 20 kR. There are also uncertainties on the brightness values associated with the image integration time: the peak intensity may be higher but for a shorter duration than the image exposure.

Figure 3.4 is a heat map constructed according to the number of occurrences of QP flashes with respect to colatitude (extended 20° from pole) and local hour (from noon to midnight). The detailed steps are explained in Section 2.1.2. The darker colour in this figure stands for more occasions of overlap of the flash morphology, while the plain yellow regions outside the main distribution are partially the result of residual background after applying the subtraction method. The background lie at the margins of the distribution in most cases and hence do not influence our flash distribution. We present that QP auroral flashes have a strong preference in spatial locations in

Table 1: List of transient flashes identified from HST images of Saturn's northern hemisphere. The data sets are illustrated with flash sequence number, "Flash start time" representing the HST-to-Saturn subexposure in which each flash is first observed, TD the time duration (in minutes) in which the flashes were identifiable on the images, the spatial locations where flashes were switched on with respect to Local Time (in hour) and Colatitude (in degrees), the maximum intensity of each flashing episode measured in kiloRayleigh, and the average Cassini's range (in saturnian radii) away from the planet during the flash interval.

No.	Flash start time	T_D (m)	LT (h)	Colat (°)	I_{max} (kR)	Range (Rs)
1	2013-110 12:11:25	11.0	18-21	15	27.8	14.9
2	2013-111 12:00:02	11.0	16-20	15	37.8	9.0
3	2013-111 13:31:04	4.7	16-20	15	28.7	8.5
4	2013-113 07:04:05	6.3	18	10	35.8	12.5
5	2013-138 02:16:43	6.3	14-17	10-15	86.0	19.4
6	2013-139 01:46:36	11.0	14-18	10	45.3	15.5
7	2013-140 18:00:53	8.7	13-17	10	41.0	6.3
8	2013-140 19:08:00	9.0	13-16	10	41.2	6.2
9	2013-140 20:39:02	8.7	15-19	5-15	52.2	6.3
10	2013-141 16:04:12	13.3	14-18	10-15	33.3	10.5
11	2013-142 01:21:47	6.3	12-14	10	37.3	12.9
12	2014-097 07:55:23	11.7	13-15	15	63.3	21.0
13	2014-100 02:29:09	14.0	13-21	10-15	96.1	12.9
14	2014-102 23:42:51	7.0	18	10	49.3	26.0
15	2014-145 04:39:03	16.3	15-19	10	36.9	45.2
16	2014-145 06:24:00	14.0	17-21	5-10	64.3	45.4
17	2014-145 07:29:31	11.7	13-18	5-10	61.2	45.5
18	2016-181 03:53:59	7.5	13-16	15	66.5	10.7
19	2016-181 04:59:25	7.5	14-16	15	63.2	10.7
20	2016-181 07:04:50	5.0	15-18	10-15	72.5	10.7
21	2016-232 19:36:50	7.5	20-23	10-15	86.1	8.0
22	2016-232 21:27:15	15.0	14-20	10-15	151.2	8.2
23	2017-066 15:44:06	16.7	13-15	5-10	70.1	3.3
24	2017-088 02:29:43	8.3	15-19	15	82.0	4.0
25	2017-095 06:49:16	8.3	18	10	65.4	4.5
26	2017-154 21:04:14	8.3	15-18	5	48.8	5.0
27	2017-206 18:00:08	8.3	15	15	42.9	1.5
28	2017-238 23:45:06	8.3	18	10	54.1	3.0
29	2017-239 04:15:01	16.7	15-17	15	59.8	3.0

both axes: 14-19 LT and 8-15° colatitude. The regions with the highest occurrences (10 overlaps) are centred at 10° colatitude and 14-16 or 17-18 LT, indicating an even distribution of QP flashes from the mid noon-dusk sector to the dusk at high latitudes.
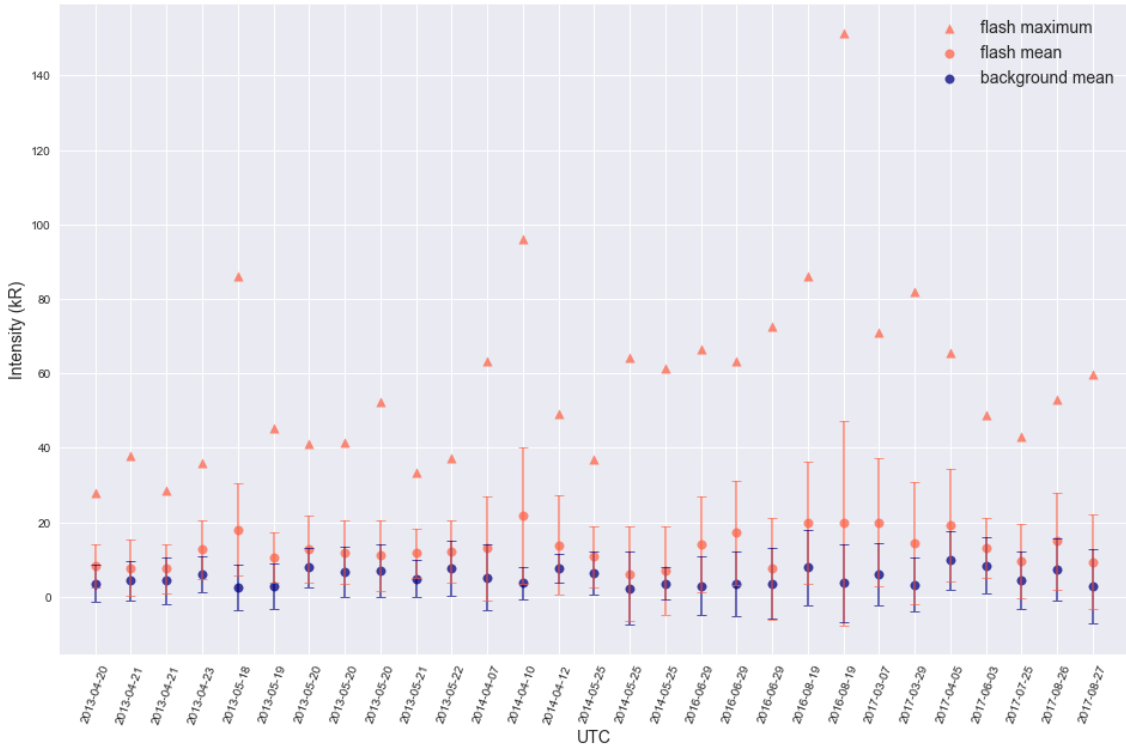
Figure 3.8: Graph of the mean intensity (in kR) of transient flashes (orange dots) compared to the mean intensity of the same local region before flash events occur (blue dots), with uncertainty marked in both intensities. The maximum intensity for every flash event is represented by orange triangles.

However, it is noticeable that two exceptions, marked with green boxes, lies outside of the main distribution of occurrence in our observations: they are flash no.11 at noon and no.21 (Figure 3.2e) at pre-midnight.

Flash no.11 is located near noon where the ∼30 min duration noon brightenings are found (Yao et al., 2017). Although its nature cannot not be accurately categorised because of the spatial and temporal overlap with a rather persisting (>20 min) feature (see Figure A.6d), a significant intensification (Figure A.6 b) in emission power followed by a dimming (Figure A.6c) is clearly observed. But this could also indicate intensity fluctuations in a more persistent brightening, rather than an isolated flash on top of a near-noon feature.

Flash no.21 is located between 21-24 LT which is clearly outside of main distribution of observed transient flashes, but QP pulsations in the magnetic field at the nightside (and even near midnight) have been observed by Cassini Magnetometer for the time list
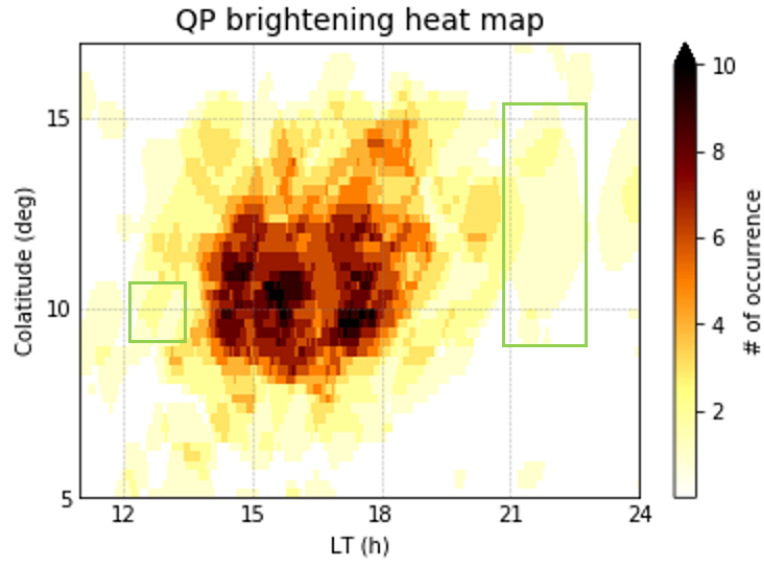
Figure 3.9: Heat map of all identified transient flashes plotted with Colatitude versus Longitude (represented in local time). The colour scale encodes the number of occurrences from light to dark with highest value 10. Two green boxes highlights two flash events outside of the main distribution in terms of their spatial dependence in LT. Some faint yellow areas appear in the plot as a result of residual background.

in this study and will be described in the next section. So, the lack of observations of transient flashes near midnight is likely to be raised by the limitation of HST observing windows. Additionally, the lack of detection of transient flashes in other local times (e.g., the dayside) could be given by the presence of bright main oval which insulated the observation of any transient auroral features, but in this study the flashes were indeed observed for both strong and very weak (or maybe in the absence of) main emission.

4 Cassini Magnetometer Observations of Quasiperiodic Perturbations

4.1 *In-Situ* Measurements of Saturn's Magnetic Field

We examined *in-situ* magnetic field data measured by Cassini's magnetometer for the time list of HST observations of transient auroral flashes (Table 1). On 2014-145 Cassini was located >45 Rs (see Table 1), i.e., outside the magnetosphere. Out of the remaining events, quasiperiodic pulsations in the MAG data were observed on ten of these days (24h interval) and simultaneous with a transient auroral flash on 6 events. The magnetic field measurements are plotted for each day in chronological order as Figures 4.1-4.6. From top to bottom in each MAG figure, the panels illustrate the radial distance of Cassini (in Rs), the radial (B_r), azimuthal (B_ϕ), and southward (B_θ) components of the magnetic field (KRTP coordinates) and the total field magnitude. The labels on the x-axis represents UT (in the hh:mm format), Latitude (positive direction to the north) and Local Time (in hours), respectively. The red shading on each plot indicates the time during which a transient flash was observed in HST images. Some outstanding regions are indicated with green boxes.

On 2013-110 (Figure 4.1a), sawtooth-shaped perturbations with <0.5 nT magnitude are visible in the B_ϕ component throughout the whole 24-hour interval shown, and several peaks in the B_θ component in the early hours can also be seen. The signals are easiest to observe in B_ϕ due to the smaller magnitude of the background field in this component. Cassini was at a radial distance of $\sim$15 Rs in the southern hemisphere around the time the HST images were taken (red shading), but the signal during this time interval is flat right after a gradual increase of magnitude $\sim$0.5 nT unlike those typical asymmetric peak structures that are picked up during the day. The periodicity of perturbations generally appears to be $\sim$1h except that it obviously shortens to $\sim$20 min between 15-19 UT. This shortening in periodicity also shows up the following day, 2013-111 (Figure 4.1b), in which several peaks around 13-15 UT (highlighted with green box) develops into shorter periods starting from 18 UT. These $\sim$20 min signatures were investigated by a case study of QP auroral hiss and magnetic field perturbations around auroral current encounters (Badman et al., 2015).

On 2013-138 (Figure 4.2a) a series of at least 5 consecutive B_θ perturbations (highlighted with green box) of $\sim$0.5 nT intensity are seen including one during the flash exposure time. This suggests that the magnetic field perturbations were of an abnormal configuration, with B_θ more significant than B_ϕ which was continuously noisy for half

Figure 4.1: Magnetic field measurements in KRTP coordinates recorded by Cassini's magnetometer. Red shade represents the time when flash was observed by the HST. (a): 2013-110; (b): 2013-111.
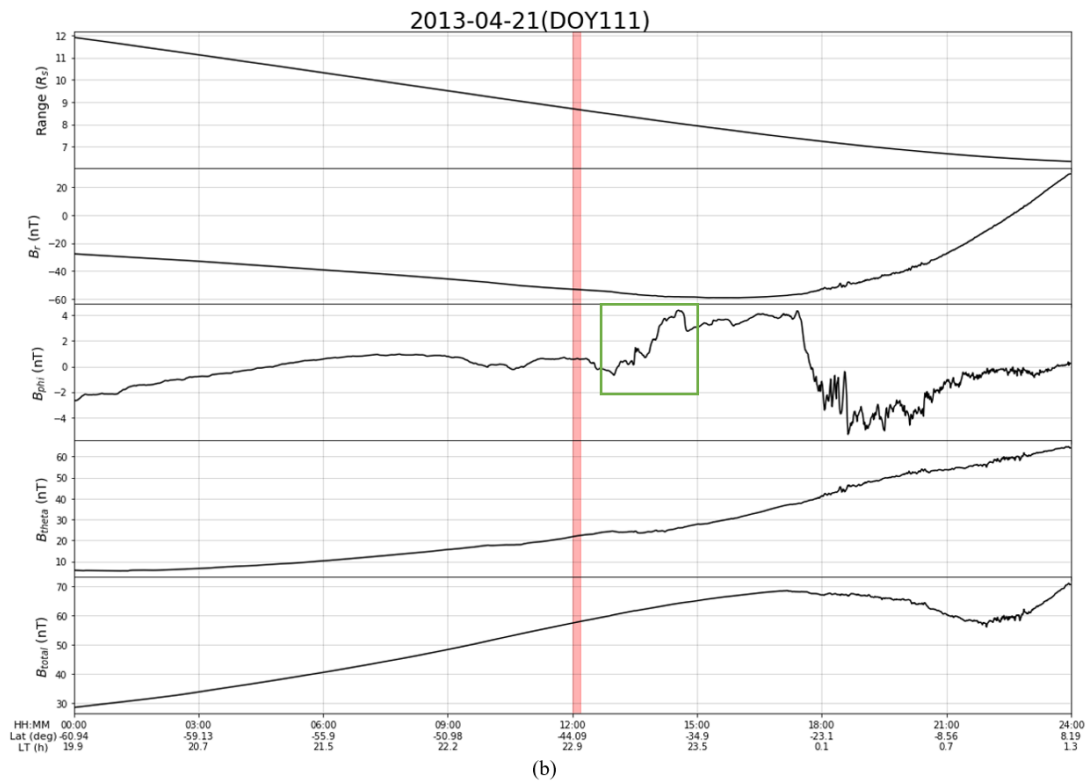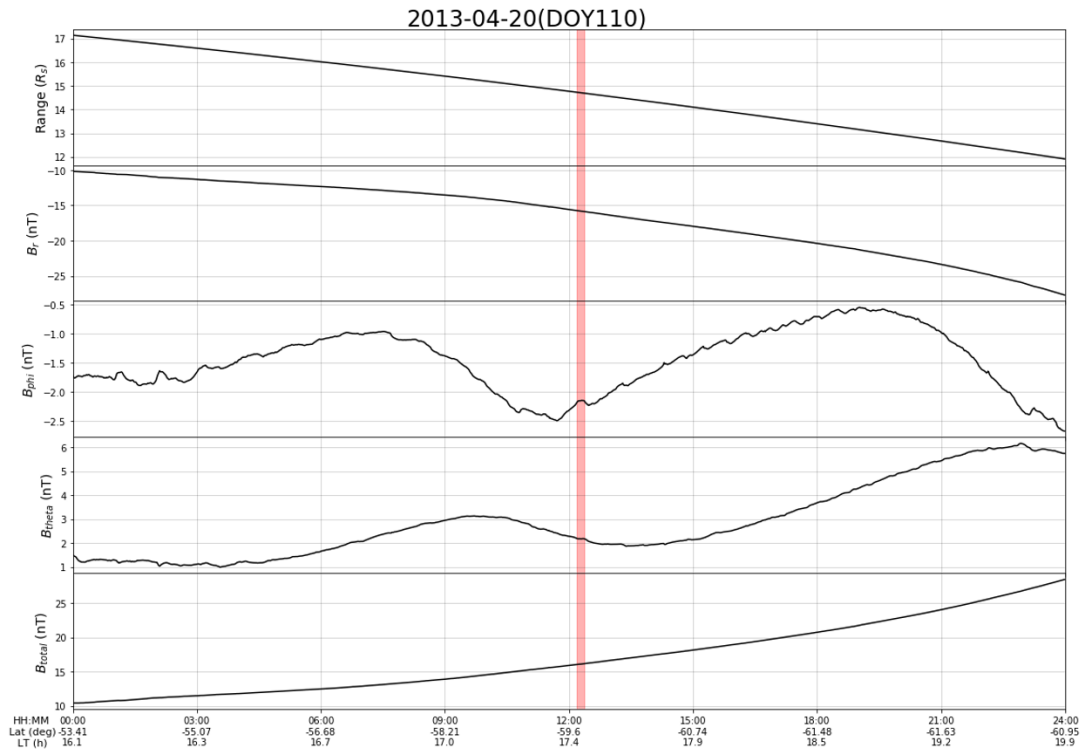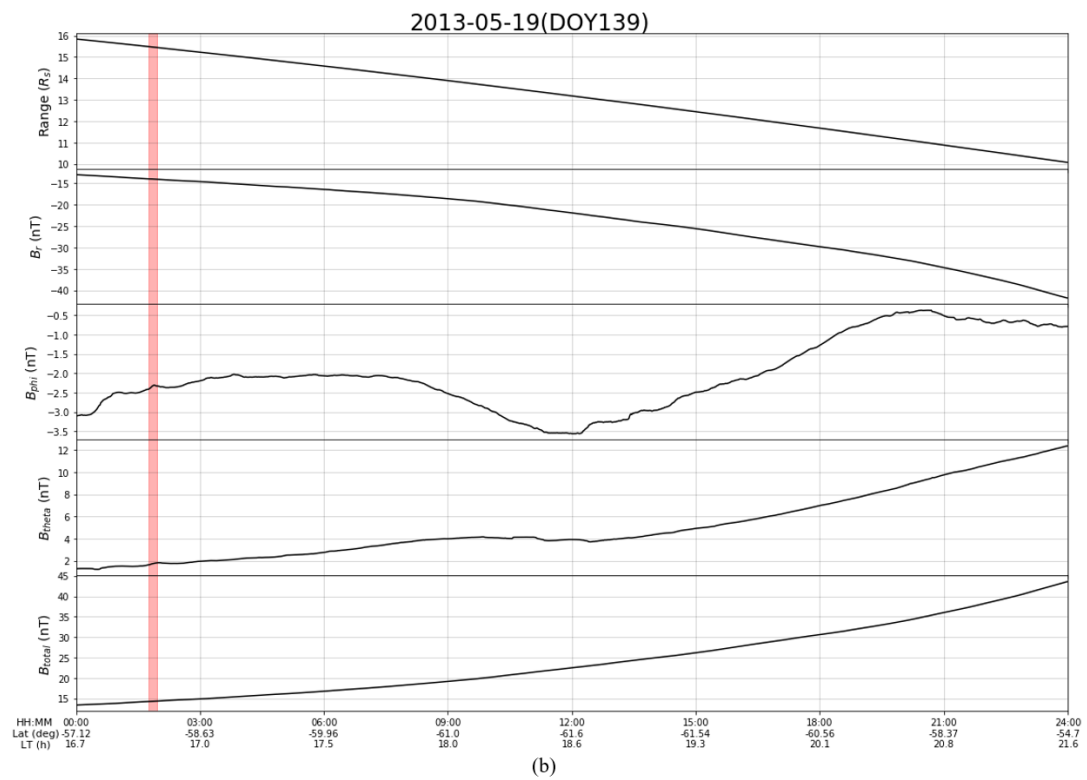
Figure 4.2: Magnetic field measurements in KRTP coordinates recorded by Cassini's magnetometer. Red shade represents the time when flash was observed by the HST. (a): 2013-138; (b): 2013-139.

of the day. The variability of the field suggests this was a region of hot plasma e.g., the outer magnetosphere. 2013-139 (Figure 4.2b) shows a quasiperiodically perturbed field in B_ϕ, similar to 2013-110 (Figure 4.1a) to some extend, with the spacecraft located at a similar range ($\sim$15 Rs) in the south during the flash exposure. But the perturbations are relatively weaker ($<$0.3 nT) and take smoother ripple shapes instead of sharp sawtooth. This makes the perturbations clearly detectable only on early, middle and late hours of the day. On 2013-140 (Figure 4.3), Cassini was in the southern hemisphere (with initially a constant negative B_r) when it picked up a series of large B_ϕ pulsations of $\sim$2 nT magnitude on average between 9-15 UT (marked in green box) with the highest value 5 nT at $\sim$10 UT which can related to the main auroral current crossing. Several peaks with generally $\sim$1 h period can be observed near and after 12 UT. The spacecraft then travelled to northern hemisphere at around 16 UT (when B_r sharply reversed) and only picked up a rather different feature around 21 UT (also during the third flash subexposure) with very short periods just before another main auroral current crossing at a later time.

Figure 4.3: Magnetic field measurements in KRTP coordinates recorded by Cassini's magnetometer for 2013-140. Red shades represent the time when flashes were observed by the HST.

Recurrent B_ϕ pulsation events in the southern hemisphere with magnitude 0.5-2nT as well as the corresponding pulsations in B_θ and occasionally in B_r were observed in 2014-

Figure 4.4: Magnetic field measurements in KRTP coordinates recorded by Cassini's magnetometer for 2014-100. Red shade represents the time when flash was observed by the HST.

100 (Figure 4.4), 2016-181 (Figure 4.5a), and 2016-232 (Figure 4.5b).

For 2014-100 (Figure 4.4), the first significant sawtooth B_ϕ pulsation was picked up just before 3 UT when Cassini was at 13 Rs. The second and the third detections are at around 4 and 5 UT, starting from which the event seems to be halted for more than 2 hours. Between $\sim$7 and 21 UT, 15 consecutive QP pulsations are observed, showing the $\sim$1 h periodicity. Then the signals become noisier with small-scale sine-wave perturbations, but the large-scale change in magnitude still follows the $\sim$1 h pattern. It is also worth pointing out that the B_θ component shows a couple of perturbations of sinusoidal shapes (highlighted with green boxes) which are very different from the peak structures in the same pulsation event and even other events discussed here.

On 2016-181 (Figure 4.5a), the MAG data shows pulsations for two of the three flash subexposures when the spacecraft stayed steady between 10.5-11 Rs. But the pulsations picked up take slightly different shapes from other typical sawtooth shapes and have relatively large magnitude (1-2 nT), especially around the third image time (red stripe) where B_ϕ sharply increased after the dip whilst both B_r and B_θ saw a significant dip as well. A sharp decrease in signal is observed between the second and the third images, this stands for one more pulsation between two consecutive HST subexposures
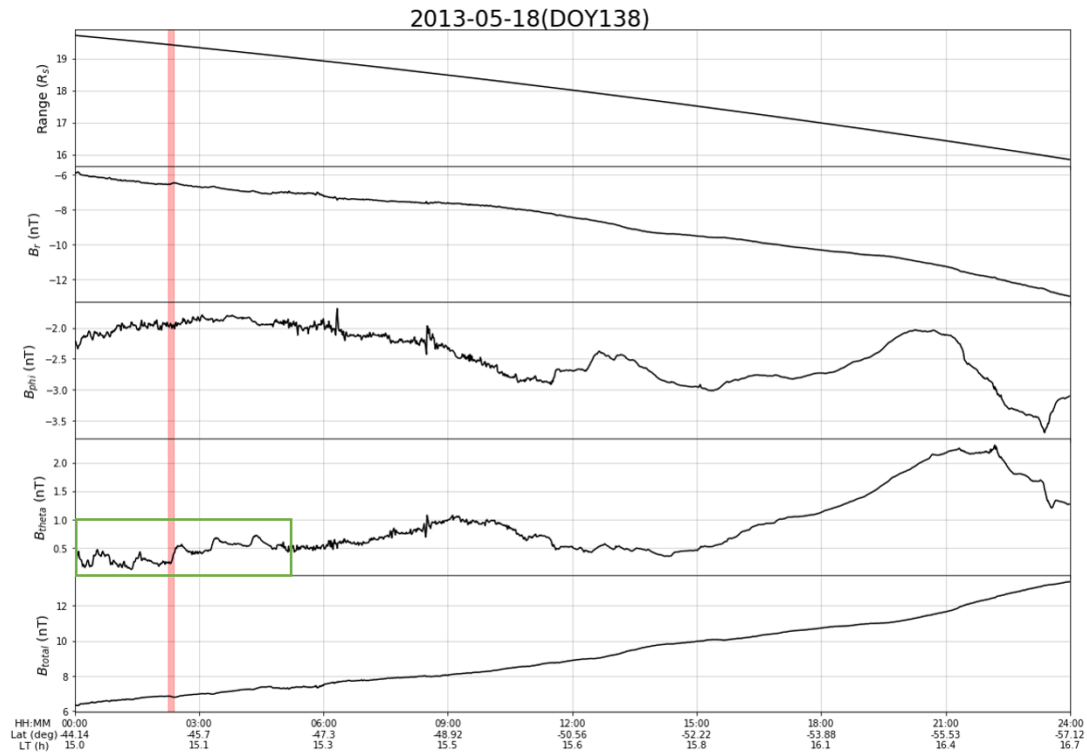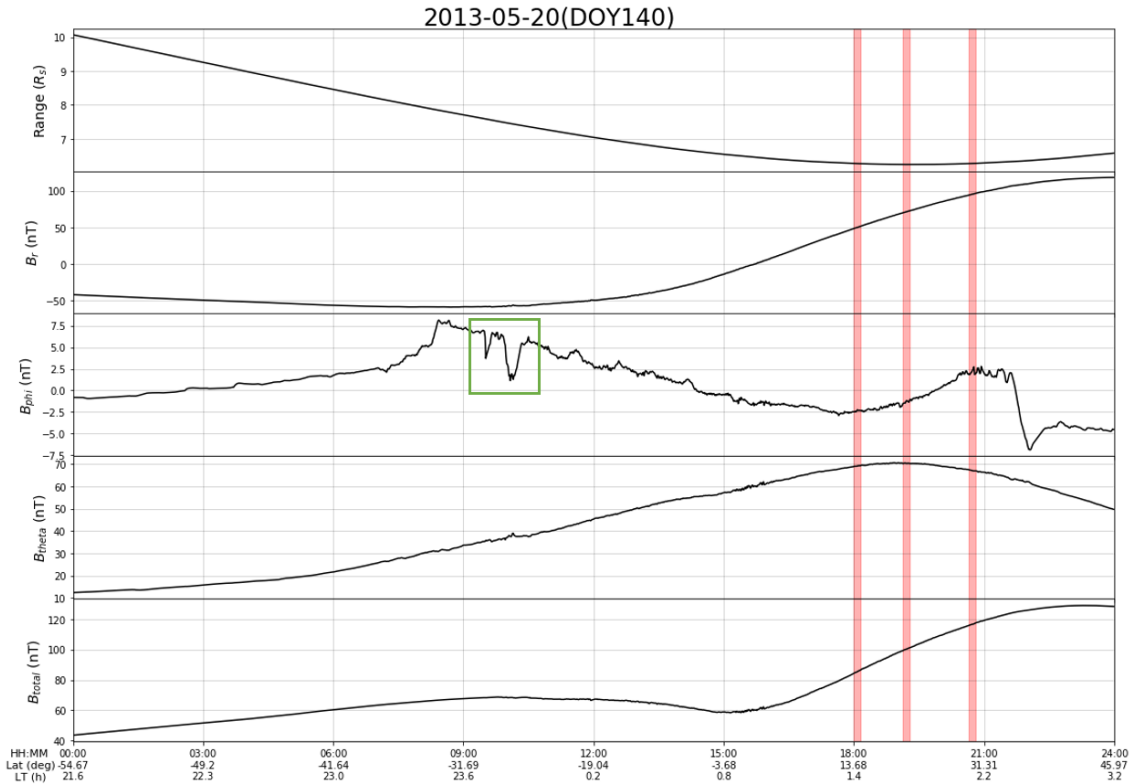
45
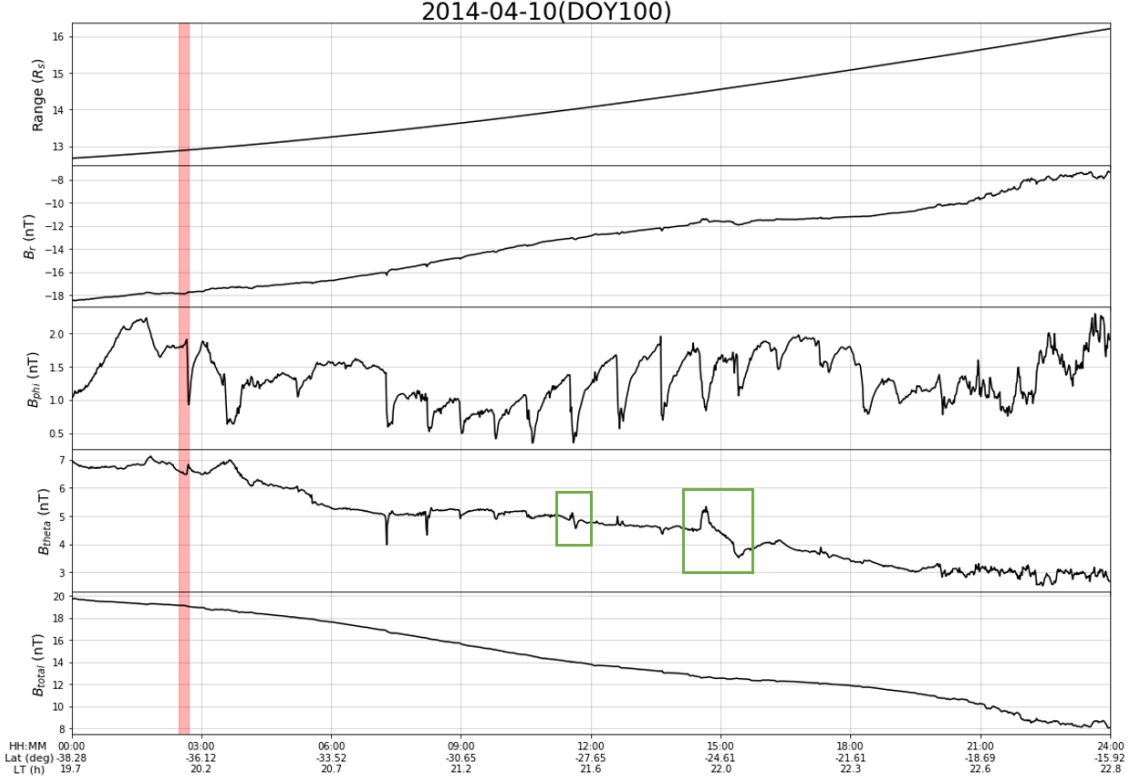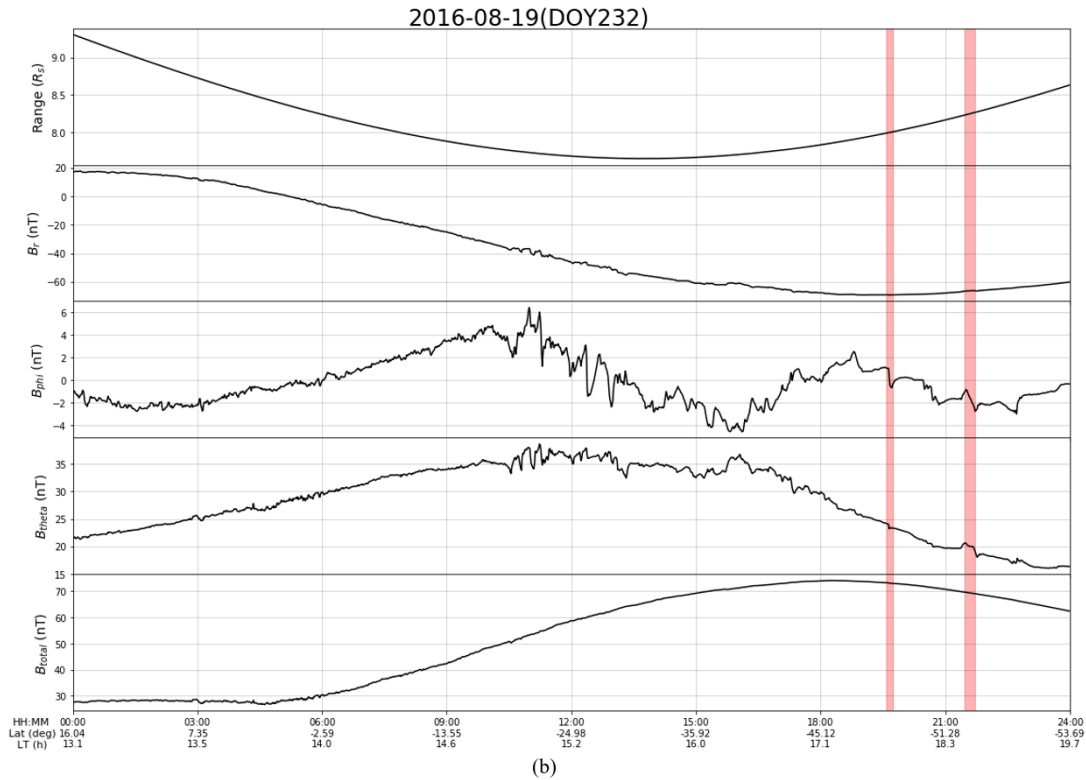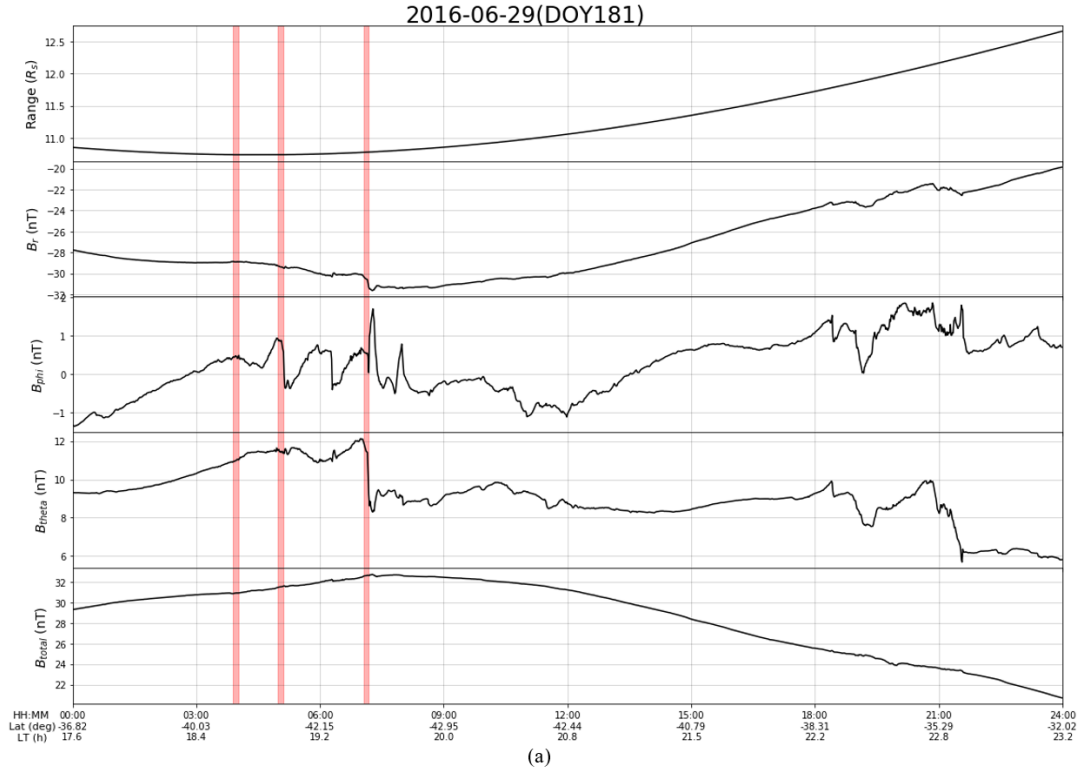
Figure 4.5: Magnetic field measurements in KRTP coordinates recorded by Cassini's magnetometer. Red shades represent the time when flashes were observed by the HST. (a): 2016-181; (b): 2016-232.

separated by ∼2 h, satisfying the overall pattern of 1 h periodicity. Looking at the change in magnitude of the B_ϕ component, the field continuously developed into non-lagged configuration (as it approached about zero) from during the pulsations as the spacecraft was in the southern hemisphere (negative B_r). Additionally, little spikes of small-scale perturbations can be seen in the rest of the day but with a much less significant magnitude.

For 2016-232 (Figure 4.5b), the field turns out to be filled with irregular perturbations for most of the day while the spacecraft was flying from Saturn's northern hemisphere to the south with a relatively low range (7.5-9 Rs). Two pulsations clearly stand out during both flash subexposures as the field turned quieter starting from 18 UT. It is noticeable that during these two pulsations the B_ϕ component dropped from positive to about zero and then from slightly negative to even more negative, suggesting the field developed from a lagging configuration into more leading, given that the spacecraft was in the southern hemisphere.

2017-088 (Figure 4.6a) and 2017-095 (Figure 4.6b) both show large magnetic field magnitudes at very low range (2-10 Rs and 2-8 Rs, respectively) as Cassini was flying in the F-ring orbits. The high magnitude of the background field change, and the detected perturbations close to both flash subexposures, which are likely to be signatures of the auroral field-aligned currents (Hunt et al., 2018), do not allow us to distinguish the target QP signatures. However, QP pulsations are indeed present in later hours (highlighted with green boxes) in the B_ϕ component alone. They are, respectively, measured to be ∼2.5 nT and ∼5 nT when Cassini's range at 6-8 Rs and 4-8 Rs and show ∼1 h periodicity.

In the HST image time sequence, we identified QP pulsations in both hemispheres of different nature, i.e., magnitude, shape, and periods. Although these pulsation events give a typical periodicity of 1 h, the periods between each pulse (or the interpulse period) can vary even if in the same event, and we found this range to be ∼40-70 min according to MAG data. The HST campaigns used in this study allowed us to observe a 60-90 min periodicity as mentioned in Section 3.3, but the uncertainty in a single HST image can be of order the integration time (2 min for 2013 campaigns and 8 min for the other years). Moreover, our results indicate the strength of pulsations observed are modulated by about half of the planetary rotation period, 5-6 h, (see Figure 5a and further description in the case study below) and agree that quasiperiodic magnetic field pulsations most commonly take sawtooth shapes rather than sinusoidal (Yates et al., 2016) and that the affected magnetic field lines are of likely to be closed rather than open because the pulsations were picked out on both hemispheres for northern transient
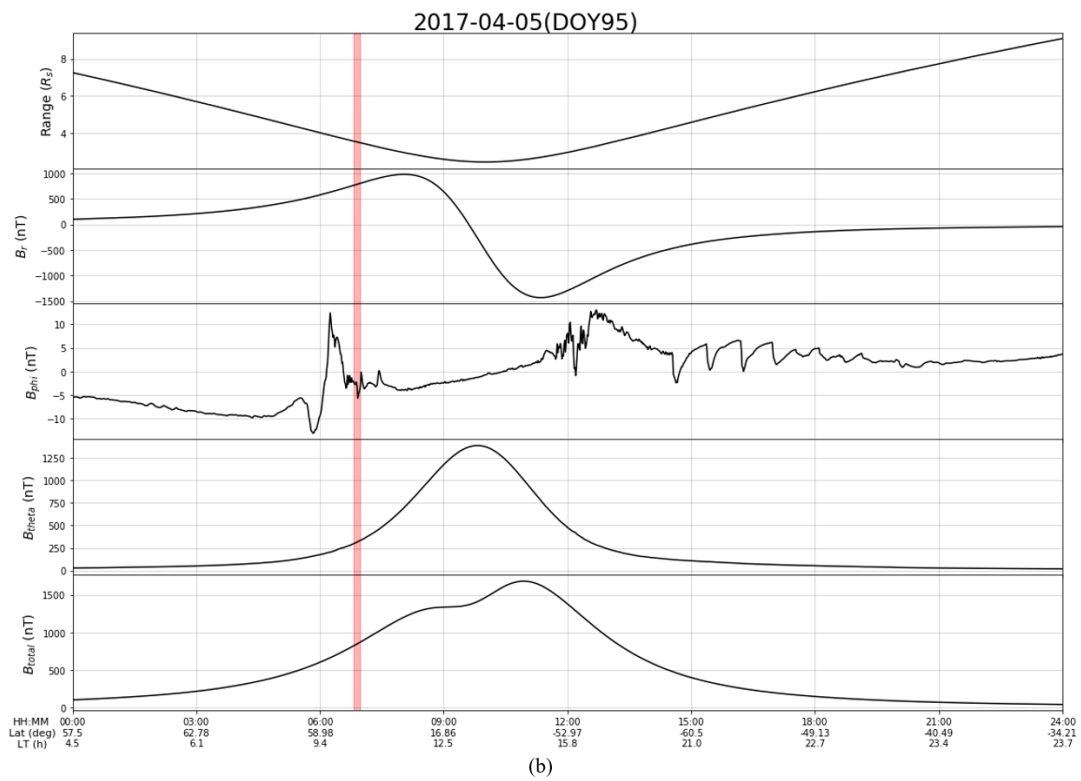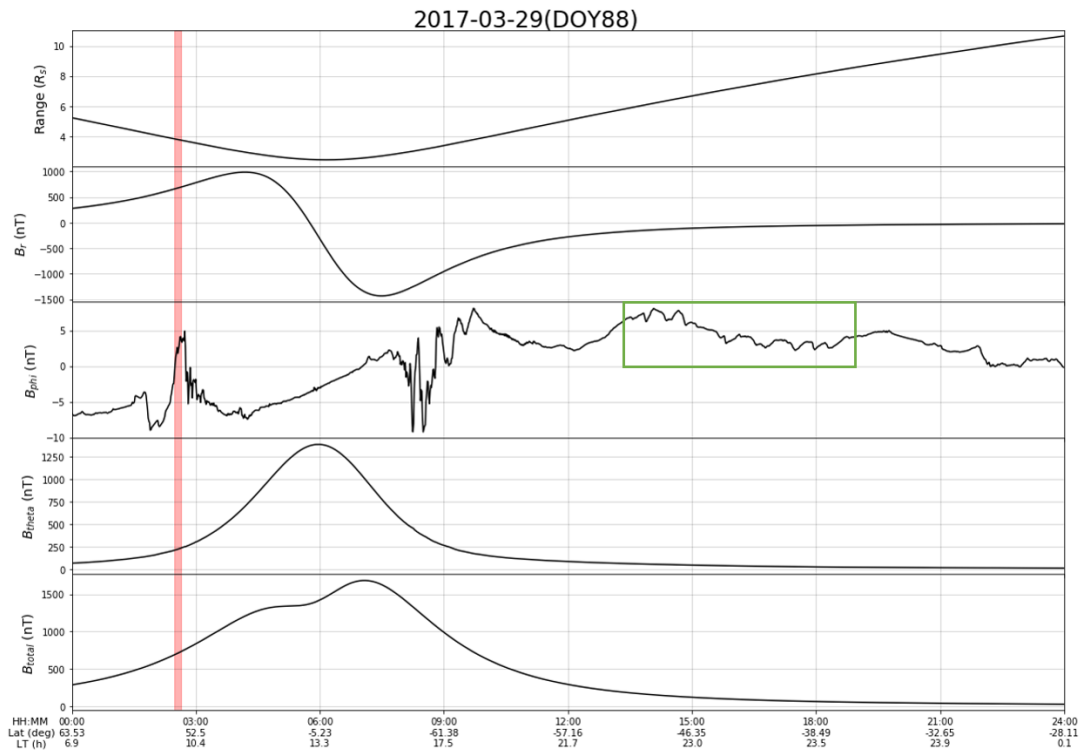
Figure 4.6: Magnetic field measurements in KRTP coordinates recorded by Cassini's magnetometer. Red shade represents the time when flash was observed by the HST. (a): 2017-088; (b): 2017-095.

auroral flashes (Bader et al., 2019). Usually, the sense of the field perturbation is towards a less-lagging configuration (i.e., reduction in positive B_ϕ values in the southern hemisphere).

4.2 Cassini Ionospheric Footprint

We obtained and plotted Cassini's ionospheric footprint for each image in which a flash was observed. The mapping from the spacecraft position was performed using the Burton et al. (2010) model of the internal field, plus the Bunce et al. (2007) model of the ring current for a standard magnetopause standoff distance of 21 Rs. As a measure of the uncertainty in the footprint position, this model has $\sim 2°$ latitude difference from the UCL model Sorba et al. (2019) for both expanded and compressed solar wind conditions. We expect Cassini's magnetometer to pick out QP perturbations primarily in the B_ϕ component (shown in the previous subsection) particularly when the spacecraft's trajectory overlaps the corresponding field line which should be near the flashing region even with the stretching effect on the field lines due to the planet's rapid rotation.

A summary of Cassini's real-time footprint in all flash sequences in this study (Table 1) was made as Figure 4.7, and the overall coverage from different years and whether QP pulsations were seen in MAG data in each HST exposure are distinguished by different colours and shapes as labelled in the lower right corner. Cassini moved to the F-ring and proximal orbits, periapsis 10 Rs, in 2017 (the Grand Finale), so it's noticeable that the trajectories (in yellow) are much longer than other years within the same exposure durations. Moreover, the footprints from 2017 did not extend to 12-18 LT sector and were generally lower in latitudes, while that from other years were more towards the planet's poles - within 15° colatitude - in the noon-dusk sector where QP pulsations were mostly found. The crosses in the 15-21 LT sector are footprints in 2013-110, 138 and 139 (green), 2014-100 (red), 2016-181 and 232 (blue), and have their MAG data in Figures 4.1a, 4.2a, 4.2b, 4.4, 4.5a, 4.5b respectively.

We find the spatial location of the spacecraft an important factor in order to pick out a quasiperiodic pulsations, and this preferential spatial location of Cassini's footprint is within 15-21 LT and 5-15° colatitude, which agrees with our observed morphological distribution of QP auroral flashes. The perturbations were not detected at lower latitudes in the preferred LT sector (20° colatitude, 20-21 LT), nor in the dawn, noon and midnight sectors at the preferred co-latitude range (5-15°). It is worth noting that Cassini's *in-situ* measurements have an orbital bias as it did not cover the high latitudes in the dayside as often as it did in the duskside. Besides, the range of the spacecraft is also an important factor. Nonetheless, this result indicates that QP auroral flashes

49

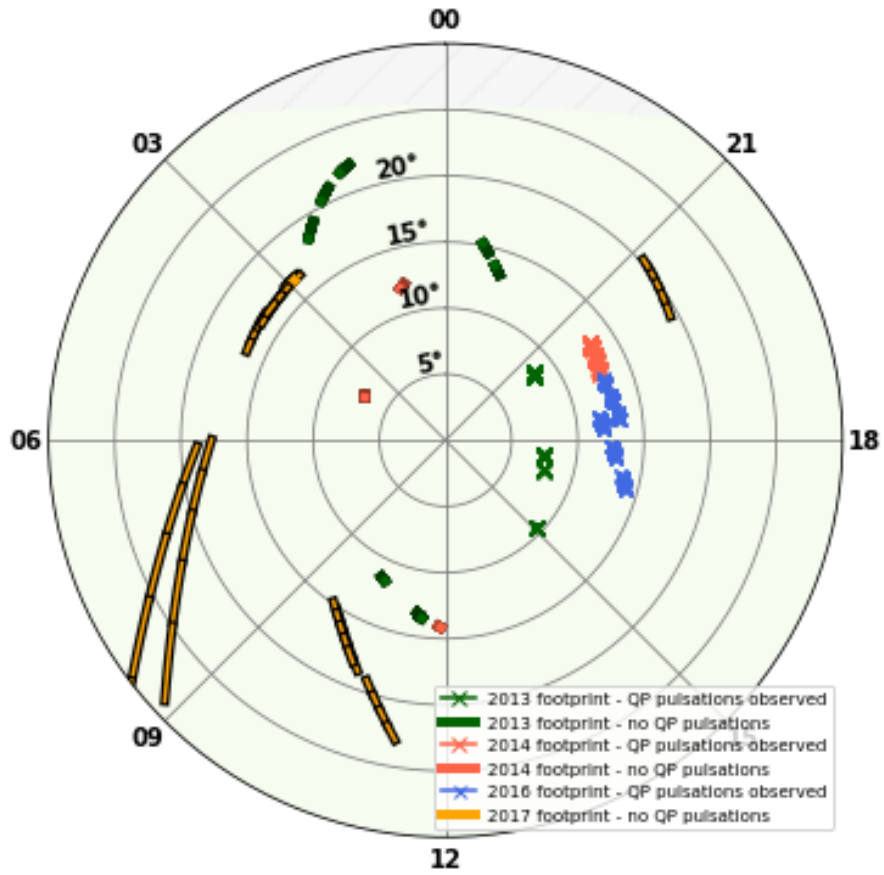Figure 4.7: Summary footprint of Cassini orbiter in flash sequences from 2013-2017. The polar projection extracts latitude from 90 to 60° (i.e., 0 to 30° colatitude) with a step of 5°. The year every colour stands for is listed in the legend at lower right corner, with the following cases of detection of QP pulsations (green: 2013-110, 2013-138, 2013-139, red: 2014-100, blue: 2016-181, 2016-232).
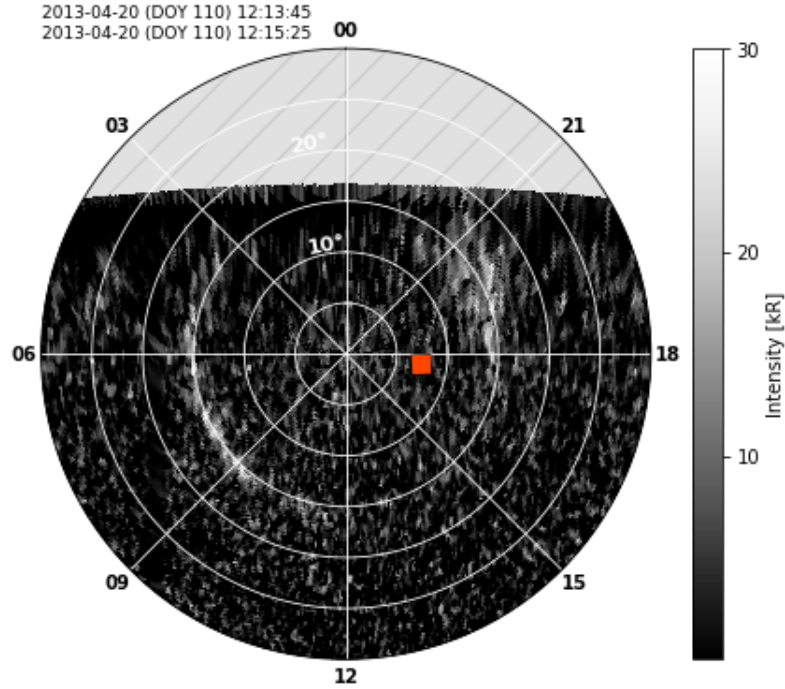
Figure 4.8: HST images of Saturn's northern aurora in polar projection with Cassini's real-time position for 2013-110. 0-30° colatitude range was extracted for these plots hence the innermost ring stands for 5° colatitude (or 80° latitude) and each two rings are spaced by 5°.

and field pulsations are likely to be localised rather than being driven globally because of lack of detection in other LT and latitude regions. The spacecraft's range, location in LT and latitude combined is the key to detection of pulsations. Cassini's range for every flash sequence is listed in Table 1, we found the ranges to be 8-19.4 Rs for our detected cases which are all in the southern hemisphere.

Figures 4.8-4.11 plots Cassini's footprint (red box) on a grey-scale polar projection of northern transient flashes for the cases of detection (indicated by crosses) in Figure 4.7 and depicts the dependence of spatial location of the events and the spacecraft.

Figure 4.9a (2013-110) shows the spacecraft measured a leading field while being $\sim 7°$ poleward away from the flash (which is at 15° colatitude) and close to 18 LT when the flash extends to the nightside (see Figure 4.1a). The B_ϕ component in Figure 4.1a during the flash subexposure (red shading) is mostly flat instead of showing a typical pulsation. Hence there is no firm conclusion on whether the periodically perturbed field observed during the day is connected to the transient flash observed. Figure 4.9 shows the 2013-138 (a) and 2013-139 (b) event with the Cassini located inside the flash region in LT as both auroral flashes are of arc shapes (i.e., extends across several hours in LT) and slightly poleward particularly for 2013-139 (b). Their MAG data are presented in Figure 4.2, showing modest perturbations in B_θ (a) B_ϕ (b), respectively.

2013-05-18 (DOY 138) 02:21:23
2013-05-18 (DOY 138) 02:23:03

(a)

2013-05-19 (DOY 139) 01:51:14
2013-05-19 (DOY 139) 01:52:54
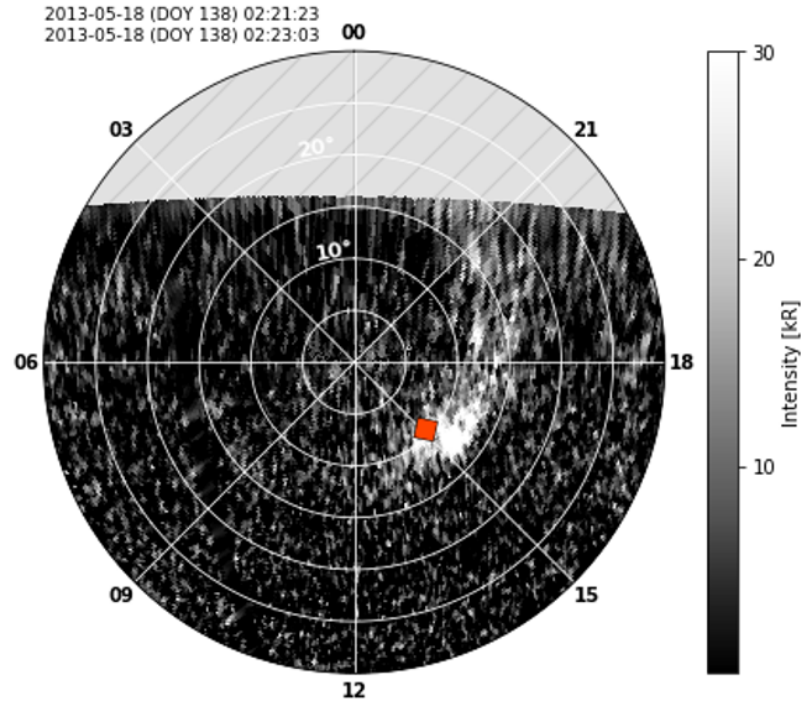
(b)

Figure 4.9: HST images of Saturn's northern aurora in polar projection with Cassini's real-time position for 2013-138 (a) and 2013-139 (b). 0-30° colatitude range was extracted for these plots hence the innermost ring stands for 5° colatitude (or 80° latitude) and each two rings are spaced by 5°.
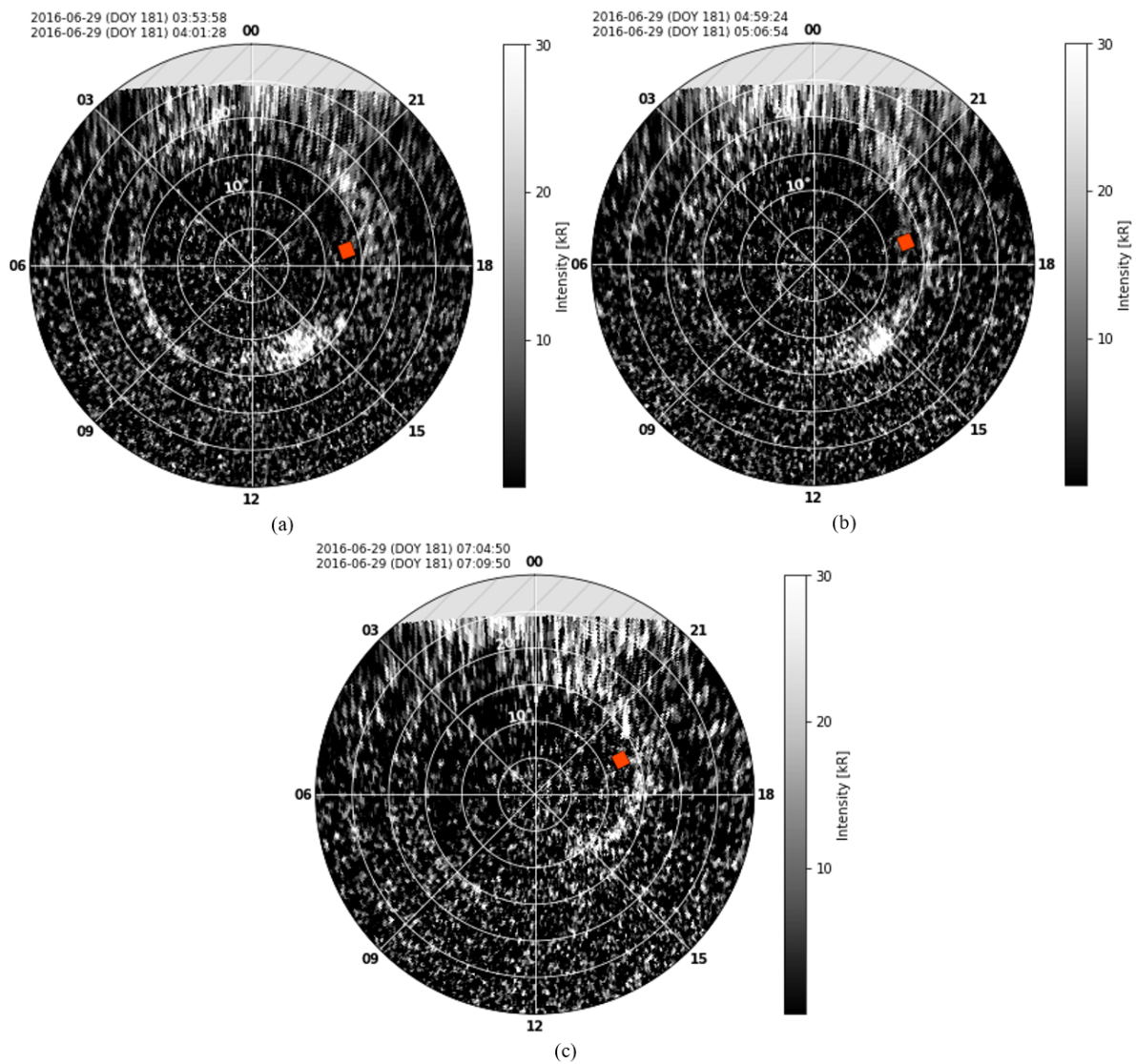
Figure 4.10: HST images of Saturn's northern aurora in polar projection with Cassini's real-time position for the three flashes in 2016-181 (a to c in chronological order). 0-30° colatitude range was extracted for these plots hence the innermost ring stands for 5° colatitude (or 80° latitude) and each two rings are spaced by 5°.

Figure 4.11: HST images of Saturn's northern aurora in polar projection with Cassini's real-time position for the two flashes in 2016-232. Panels a to c are in chronological order, while b and c are showing two consecutive image frames for the second flash event. 0-30° colatitude range was extracted for these plots hence the innermost ring stands for 5° colatitude (or 80° latitude) and each two rings are spaced by 5°.
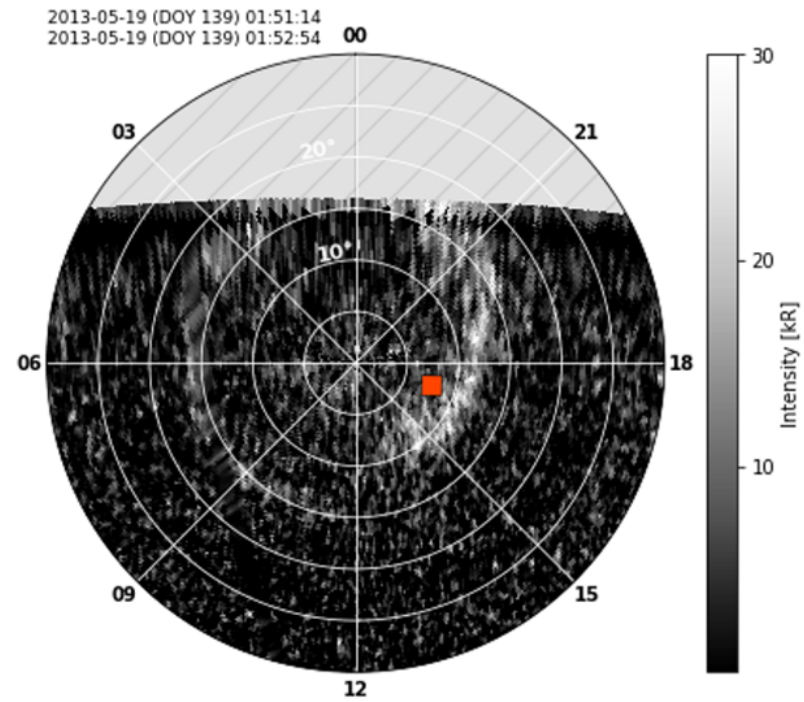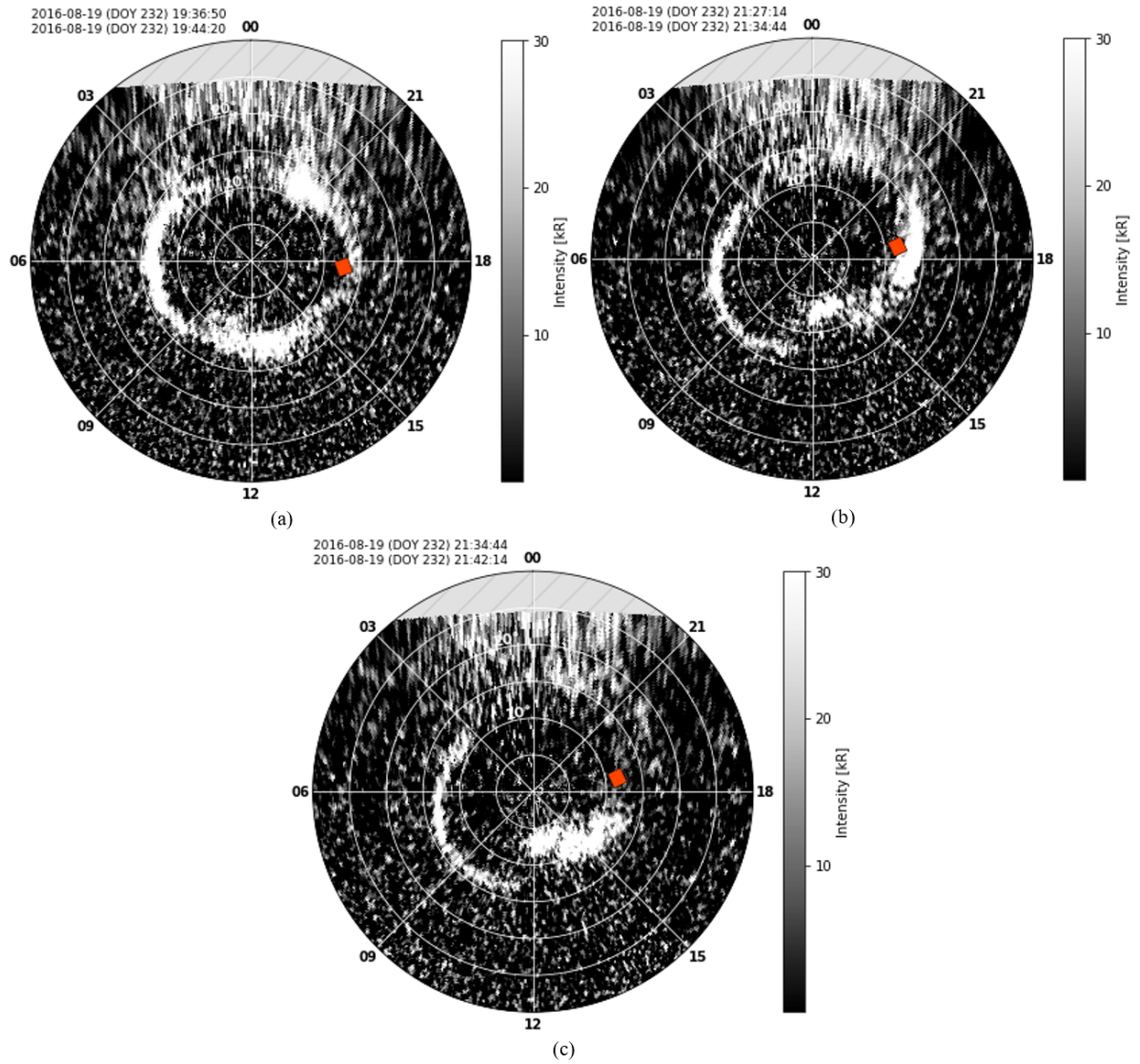
Figure 4.10 show the 2016-181 event with three separate flash episodes in chronological order (a-c). Although every flash episode did not shift in LT within its own duration, the conjugate field perturbations occurred in the direction of corotation (reduced lagging). The spacecraft moved modestly poleward and to the nightside during this interval and is located at a later LT than the flashes, whereas the pulsations do not show a bent-forward field configuration. Hence the fact that the MAG to pick up pulsations for the second and the third HST subexposure whilst it did not for the first subexposure (see Figure 4.5a) can be related to the small latitudinal change of the spacecraft. Figure 4.11 all show the 2016-232 event with a near midnight flash (panel a) and a fast-rotating flash (panels b and c) separated by ∼100 min, and their MAG data is displayed in Figure 4.5b. The spacecraft was at similar latitude as the flashes but at earlier LT (∼18 LT) for the first episode (∼21 LT) and then at later LT than the flashes as the second flash developed from ∼18 LT to ∼15 LT. The pulsations picked up by the MAG agree with this development as the B_ϕ showed a sharp drop from positive to about zero (less lagging) and then a second drop into more negative (more leading). Overall, Cassini's locations with detection and the distribution of the transient flashes show an agreement in general, indicating there is something regional taking place in the duskside powering the transient flashes.

4.3 Case Study: 2014-99 − 2014-100

This case study aims to extend the time interval in search of the dependence between multiple pulsation events and Cassini's coverage while taking the orbital bias into account. We used SPICE to obtain Cassini's trajectory from 2014-80 to 2014-120 (Figure 4.12a) shown as the orange path which completes an oval coverage at high latitudes. Four sequences of QP pulsation events, in total, are observed in the magnetometer data (see green boxes in Figure 4.13) whose time duration are marked with thick red chunks. The four pulsation events are all identified between ∼15-23 LT at 10-15° colatitude from 2014-99 to 2014-100. Non-detection outside the duskside could be due to the higher radial distances when the spacecraft travels to the dayside. In addition to the footprint pattern of detected cases in Figure 4.7, this case study provides a detection of pulsation which was also picked up near midnight, 21-23 LT, meaning that these QP flashing events can extend to near midnight and the fact that our flash no.21 (see Figure 3.6b or 4.11a) is only lying outside the main distribution (see Figure 3.9, green box near midnight) due to HST's limited observing window.

Figure 4.12b and 4.12c are the grey-scale HST polar projected images, of 420 sec integration time, of the 2014-100 flash (no.13) captured during this interval including

Cassini's position marked with red square. Since these two images are the consecutive frames for the same flash event, they will be referred as "frame 1" and "frame 2" in the following narrative. In this case, the flash was highly dynamical as pointed out in section 3.2, and Cassini was only on top of the flashing region after the flash itself rotated rapidly in the direction of corotation within its 14-min lifetime (twice the subexposure integration time). Figure 4.13a and 4.13b are the MAG plots for day 2014-99 and 2014-100 with pulsations highlighted with green boxes matching the four red chunks in Figure 4.12a. The pulsations take sawtooth shapes, variable intensity of $\sim$0.5-1.5 nT in B_ϕ and inconstant inter-pulse period of $\sim$40-60 min. Peak structures that correspond to the QP pulsations can also be seen in the B_θ components when the spacecraft was gradually changing its radial range. Hence it would be worthwhile to examine the MAG data in the averaged field-aligned coordinates in aid of analysing the characteristics of QP pulsations particularly when the field is in an abnormal shape. In Figure 4.13b, the blue and red stripes are HST subexposure time of the flash whose integration time matches that of frame 1 and 2, respectively.

In more details about the 2014-100 flash and its MAG data, the B_ϕ pulsation was detected in the pink shading (whose start and stop time are the same as frame 2) with a peak followed by a very sharp drop, whereas the signal remained rather constant in the blue shading as shown by the zoomed-in view. The decrease in B_ϕ indicates a transition to a less lagging field configuration as the spacecraft was at the southern hemisphere (negative B_r), this indicates that the MAG could not be measuring the pulsating field lines unless the spacecraft changed its leading position (frame 1) to a slightly lagging position (frame 2) relative to the flash overall morphology. The fact that MAG did not detect a pulsation during the time of frame 1 whilst it did during frame 2 further proves the direct connection between transient flashes and QP pulsation events picked up in magnetic field measurements.

The duration of each event ranges from 3 to over 10 hours and is separated by a gap of 2-10 hours. The gaps between the sets of events could be related to the rocking of the affected field region over and away from the spacecraft, driven by the PPO, as described in Section 1.3. This rocking has been observed in the auroral currents and the cusp at Saturn (Bunce et al., 2014; Arridge et al., 2016). However, the duration of the gaps is irregular (2-10 h), and there are other examples where gaps are not present, e.g., 2013-100 (see Figure 4.1a). This effect could be further examined by comparing the position of the spacecraft relative to the PPO oscillation in more detail to possibly determine the boundaries of the pulsating region.
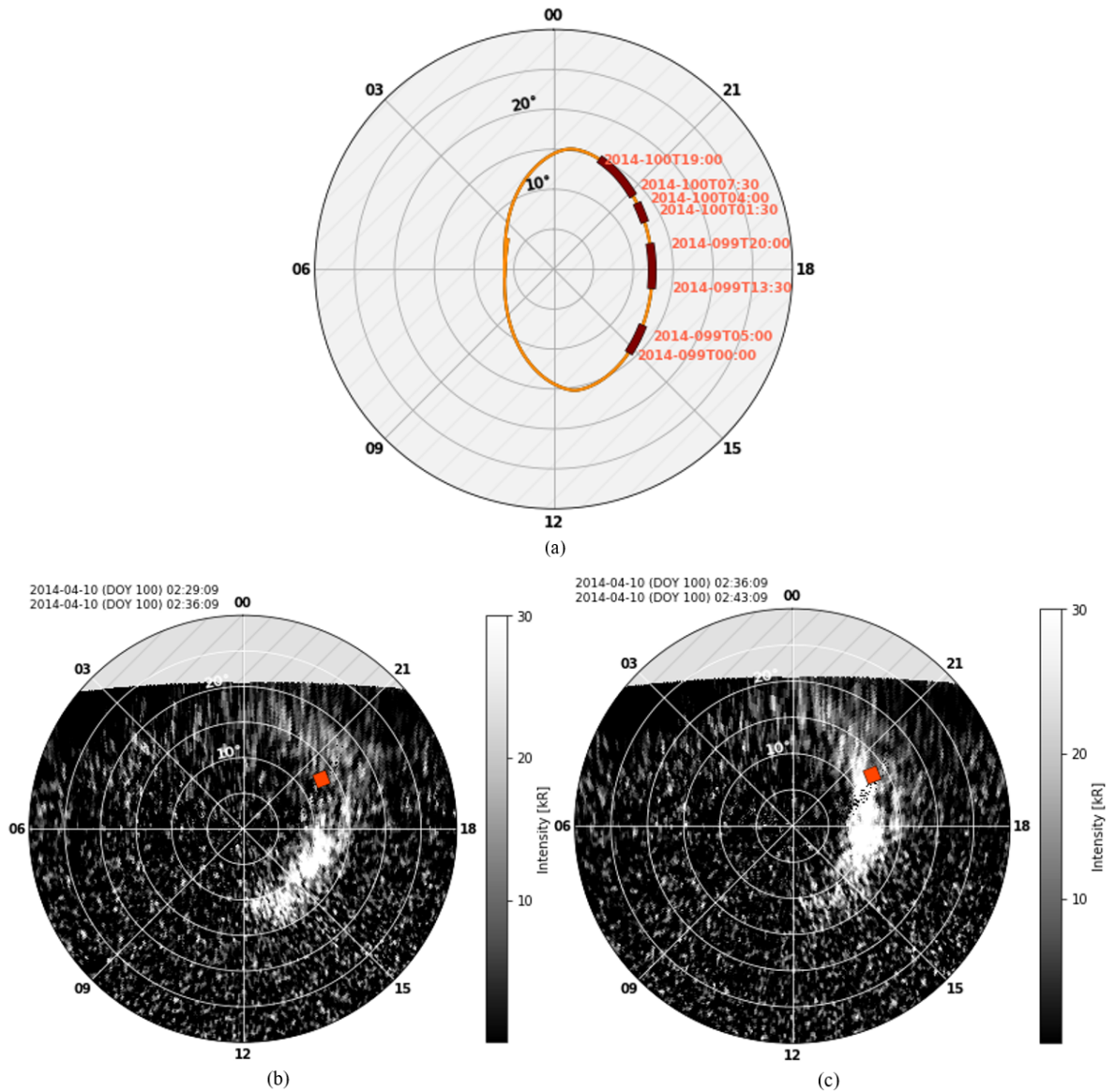
Figure 4.12: (a): Trajectory of Cassini spacecraft from 2014-80 to 2014-120 (orange path), obtained using SPICE, projected onto the Kronocentric polar plane, with 4 QP pulsation events identified in MAG data (red thick chunks) during this interval. (b) and (c): Grey-scale HST images for 2014-100 transient flash (no.13) with Cassini's real-time position mapped onto the projection.
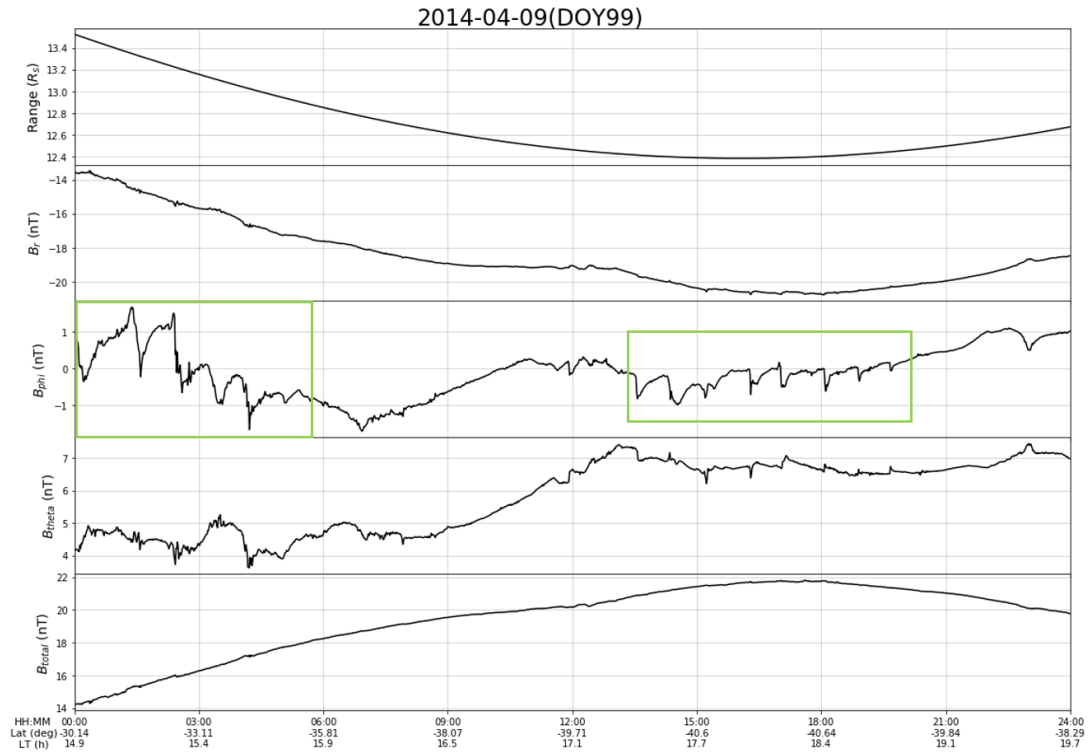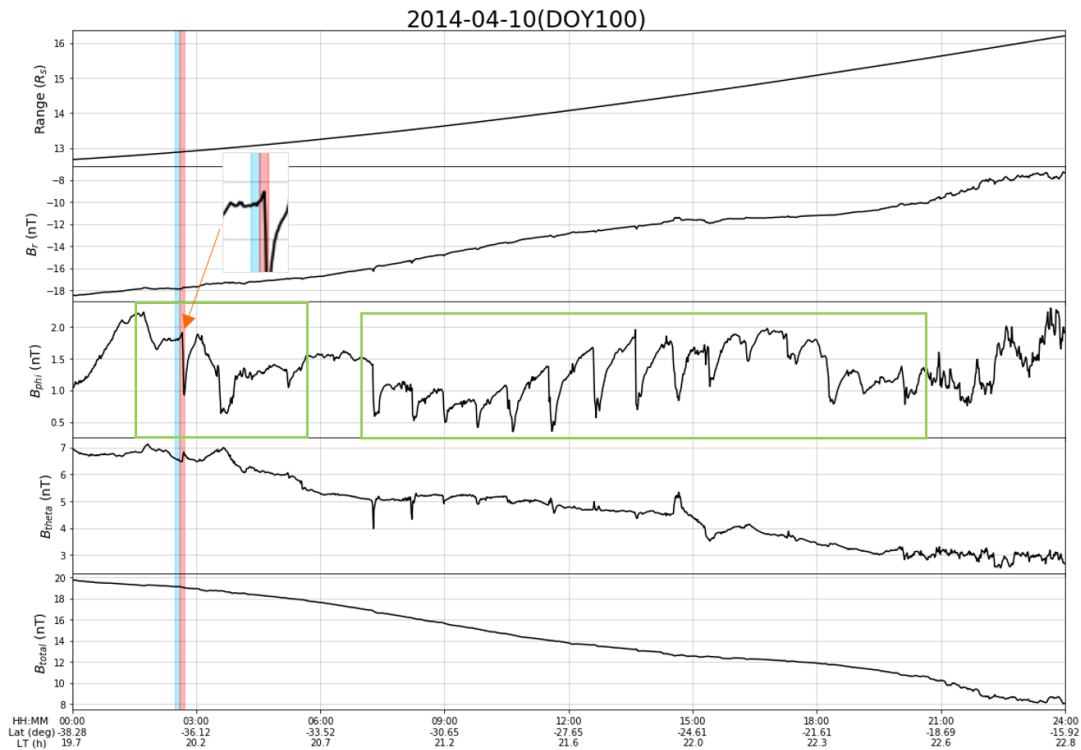
Figure 4.13: Magnetic field measurements in KRTP coordinates recorded by Cassini's magnetometer for 2014-099 (a) and 2014-100 (b). The green boxes highlights the four pulsation events observed in the two days, and the shadings in blue and red matches the two consecutive HST subexposures for the 2014-100 event.

58

5 Conclusion and Discussions

In this study, we examined 36 days of HST observations of Saturn's northern UV aurora during 2013-2017 and identified 29 flashes. These transient features appear for ∼4-17 min in HST subexposures, though can be subject to uncertainties related to the image integration times, and are predominantly located at ∼8-15° colatitude in the duskside (14-19 LT). In this research, more than one flashing event in the same day was found on 6 occasions (2013-111, 2013-140, 2014-145, 2016-181, 2016-232, and 2017-238 to 239) indicating these transient flashes can be recurrent leading to the quasi-periodic characteristics. The spatial distribution is in general agreement with the duskside preference from previous studies (Roussos et al., 2016; Palmaerts et al., 2016; Bader et al., 2019; Pan et al., 2021). However, the modified Alfven wave model by Rusaitis et al. (2021) concluded no strong dependence of spatial location for QP pulsed events after normalising for the spacecraft's dwell time.

We analysed the Cassini MAG data for the time list of HST observation of transient auroral flashes (Table 1) and identified 10 sets of QP pulsed events (6 of them occured exactly simultaneous with the HST flash exposure). The field perturbations take asymmetric sawtooth shapes with typical magnitudes ranging from ∼0.5-2 nT primarily in the B_ϕ component and only irregularly in B_θ and B_r (see Figure 4.1a, 4.2, 4.4a and b). Their shapes can be ambiguous (see Figure 4.1b and 4.3) and the magnitudes can reach as high as ∼5 nT when Cassini travelled closest to Saturn (see Figures 4.5b, 4.6a and b). We find Cassini's range to be 8-19.4 Rs for our detected cases (all in the southern hemisphere), this agrees with Palmaerts et al. (2016) who found the dependence in range to be 5-30 Rs in the northern hemisphere and 5-20 Rs in the southern hemisphere. Hence the factors affecting the sampling of pulsation events are the combination of Cassini's spatial location in LT, latitude, and distance.

The pulsation events can vary from a couple of pulses to recurrent events with duration over a half day. A typical periodicity of ∼1 h can be found on both HST images and MAG data, which is consistent with particle and wave measurements found in other studies (Radioti et al., 2013; Roussos et al., 2016; Palmaerts et al., 2016; Carbary et al., 2016; Mitchell et al., 2016; Bader et al., 2019; Pan et al., 2021). The inter-pulse period in the same event could vary, and we found different ranges using HST images (60-90 min) and Cassini MAG data (40-70 min), both lying inside the distribution concluded by other multi-instrument studies (Roussos et al., 2016; Palmaerts et al., 2016; Bader et al., 2019). However, the underlying factor(s) for such a periodicity and its variability remain an open question.

There is no observed correlation between the occurrence of the transient flashes and Saturn's main emission power as they were observed with both strong and faint main emission. We infer that the QP60 events have been observed during a range of solar wind conditions, so they are unlikely to be driven by solar wind dominant mechanisms (e.g., magnetopause reconnection). Delamere et al. (2015) proposed the reconnection drizzle that occurs primarily in the duskside, and Guo et al. (2018a,b) suggested that magnetodisc reconnection can occur on the dayside. This provides indications to the dynamic process which potentially powers the QP energetic events focused in this research with similar spatial location dependence. Moreover, the HST campaigns used in this study all captured Saturn's northern aurora while Cassini picked up periodic magnetic field perturbations in the southern hemisphere (indicated by negative B_r), suggesting QP60 events occur on closed field lines. Pulsations in MAG were only observed when Cassini's footprint was in the same LT-latitude sector (inside the magnetosphere) as the observed flashes, implying that the driving mechanism is localised. This needs to be accounted for in considering the origin of the flashes, e.g., if driven by a solar wind structure, this cannot impact all LT or propagate through the magnetosphere equally, otherwise a more global response would be expected. The aforementioned studies used a sharp drop in the B_θ component or negative B_θ as an identifier of current sheet crossings, however, for QP pulsations detected at high latitudes in our research, the B_θ component often shows an increase (i.e., becomes more southward) and the sharp drop is observed in the B_ϕ component (i.e., becomes less lagging).

Some previous works indicated wave relations for these quasi-periodic pulsed events (e.g., Yates et al., 2016; Yao et al., 2017). However, the identified magnetic field perturbations in the B_ϕ component presented in Section 5.1 are of asymmetric sawtooth shapes instead of sinusoidal shapes, and the discontinuities in the pulsated events are more random than expected for wave signatures. In addition to the lack of wave-related characteristics, the auroral flashes are predominantly located in the duskside and tend to have even shorter lifetimes than the noon features investigated by Yao et al. (2017). At Jupiter, Yao et al. (2021) suggested compressional waves are also associated with Jupiter's auroral pulsations. However, the Saturn flashes are very commonly seen, so the question remains whether they need a transient driver e.g., bursts of magnetodisc reconnection, or if they are an ongoing state of the magnetosphere.

6 Future Work

In respect of future works, an algorithm to pick out recurrent sawtooth-shaped pulsations (as presented in this study) in the magnetic field measurements since Cassini's arrival would provide a full picture of spatial location dependence of the QP pulsations and potentially the modulation as a result of the PPO. It is, hence, important to examine the field measurements in both Kronocentric and field-aligned coordinate systems in order to identify in which coordinates the pulsations are seen especially for the cases when pulsations are seen in all Br, B_θ and B_ϕ components. Furthermore, a modified model for standing Alfven waves (Rusaitis et al., 2021) found QP pulsations primarily on the duskside but having no LT dependence after the normalisation of Cassini's dwell time, and Bader et al. (2019) identified transient events on the dawnside using the Cassini UVIS data although the overall location bias is towards the duskside. However, in this study (using the HST data) we do not identify any other similar features in the dawnside. Therefore, it is necessary to extend the analysis to include earlier HST campaigns during the entire Cassini era in order to make the comparison with the event time sequence given by both standing Alfven wave model and the Cassini UVIS data. A few "stepped" ion energy-latitude dispersions in the ion flux measurement indicate recurrent reconnection events in the magnetodisc or magnetopause, (Delamere et al., 2015) proposed the idea of a drizzle of small-scale reconnection sites which means that recurrent reconnection events could occur at multiple reconnection sites. So, combining field and particle measurements with morphological analysis of transient auroral flashes allows us to understand the field configuration and locate the reconnection sites especially for fast rotating events. The transient flashes and QP pulsations are observed at high latitudes, the distance of the field line traced to the planet's equatorial plane are mostly L>25 during solar compression or L>35 during solar rarefaction according to Sorba et al. (2019) Saturn magnetic mapping model. The ambiguity of whether magnetopause reconnection or magnetodisc reconnection that is powering such events is under debate, thus a plausible way could be understanding the periodic plasma injections in the magnetodisc (introduced in Section 1.3).

Lastly, the transient auroral flashes were observed in Saturn's IR aurorae (Badman et al., 2012a) although the finite lifetime of H_3^+ IR emission could result in blurring of its auroral features, so the IR instruments onboard of the newly launched James-Webb Space Telescope (JWST) would also provide us with a better view as observing from the L2 point would massively reduce sunlight contamination.

A   Appendix

In this appendix, the rest of the HST images with identified transient auroral flashes (listed in Table 1) not discussed in Sections 3 and 4 will be shown here. They are 2013-113 (Figure A.1), 2013-140 (Figures A.2-A.4), 2013-141 (Figure A.5), 2013-142 (Figure A.6), 2014-097 (Figure A.7), 2014-102 (Figure A.8), 2014-145 (Figures A.9-A.11), 2017-088 (Figure A.12), 2017-095 (Figure A.13), 2017-154 (Figure A.14), 2017-206 (Figure A.15). For every event, the frame before, during and after the transient feature will be shown, apart from the cases in which the HST exposure window did not observe the start or the end of the event. It is worth noting that the 2014 campaign comes from the usage of both "F25SrF2" and "25MAMA" filters, the later is more sensitive to dayglow and gives more noise contamination, hence the images had to be blurred more when being processed (e.g., Figure A.7b and A.11b).

The blue arrows in Figures A.7 and A.8 both indicate a dusk feature (similar to Figures 3.3 and 3.5) with duration longer than HST observing interval. The identification of transient flash in 2017-206 (Figure A.15) can be ambiguous because the near-noon feature also appears to have a pulsating emission power (indicated by the blue arrow). This is similar to the 2013-142 flash event (flash no. 11, Figure A.6) as mentioned in Section 3.3.

Figure A.1: HST images of Saturn's northern hemisphere in polar projection for the frames before (upper left), during (upper right), and after (lower centre) the 2013-113 event. The yellow arrow indicates the transient auroral power intensification 0-40° colatitude range was extracted hence the innermost ring in every plot stands for 10° colatitude (or 80° latitude) and each two rings are spaced by an increment of 10°. The longitude is represented in local hour starting from 0 at the top anticlockwise, hence the dawn is at 6 LT, noon at 12 LT and dusk at 18 LT. The exposure time for the images is 100 sec.

Figure A.2: HST images of Saturn's northern hemisphere in polar projection for the frames before (upper left), during (upper right), and after (lower centre) 2013-140 event 1. The yellow arrow indicates the transient auroral power intensification 0-40° colatitude range was extracted hence the innermost ring in every plot stands for 10° colatitude (or 80° latitude) and each two rings are spaced by an increment of 10°. The longitude is represented in local hour starting from 0 at the top anti-clockwise, hence the dawn is at 6 LT, noon at 12 LT and dusk at 18 LT. The exposure time for the images is 100 sec.
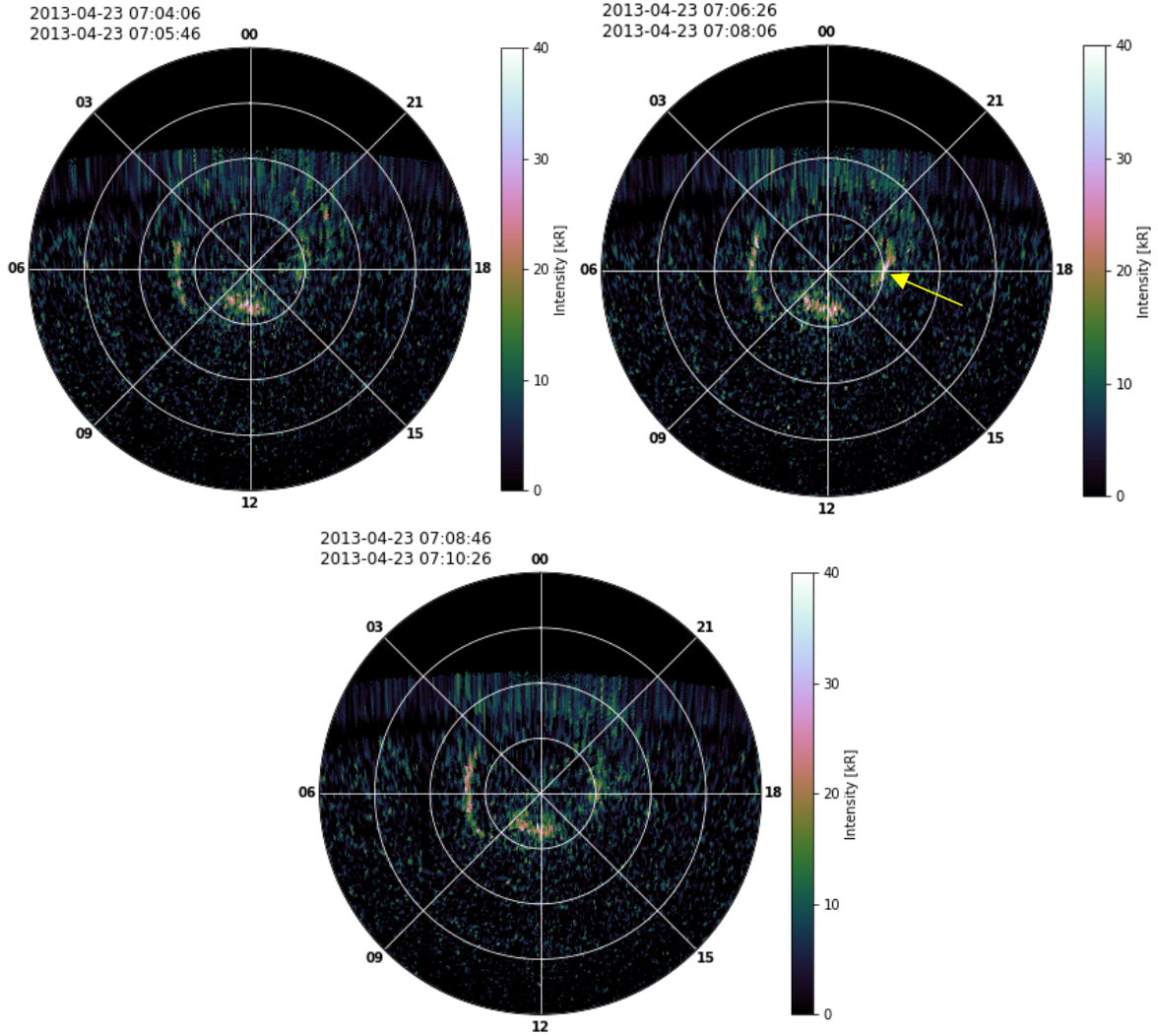
Figure A.3: HST images of Saturn's northern hemisphere in polar projection for the frames before (upper left), during (upper right), and after (lower centre) 2013-140 event 2. The yellow arrow indicates the flash region. 0-40° colatitude range was extracted hence the innermost ring in every plot stands for 10° colatitude (or 80° latitude) and each two rings are spaced by an increment of 10°. The longitude is represented in local hour starting from 0 at the top anti-clockwise, hence the dawn is at 6 LT, noon at 12 LT and dusk at 18 LT. The exposure time for the images is 100 sec.

Figure A.4: HST images of Saturn's northern hemisphere in polar projection for the frames during (left) and after (right) 2013-140 event 3. The yellow arrow indicates the flash region. 0-40° colatitude range was extracted hence the innermost ring in every plot stands for 10° colatitude (or 80° latitude) and each two rings are spaced by an increment of 10°. The longitude is represented in local hour starting from 0 at the top anti-clockwise, hence the dawn is at 6 LT, noon at 12 LT and dusk at 18 LT. The exposure time for the images is 100 sec.
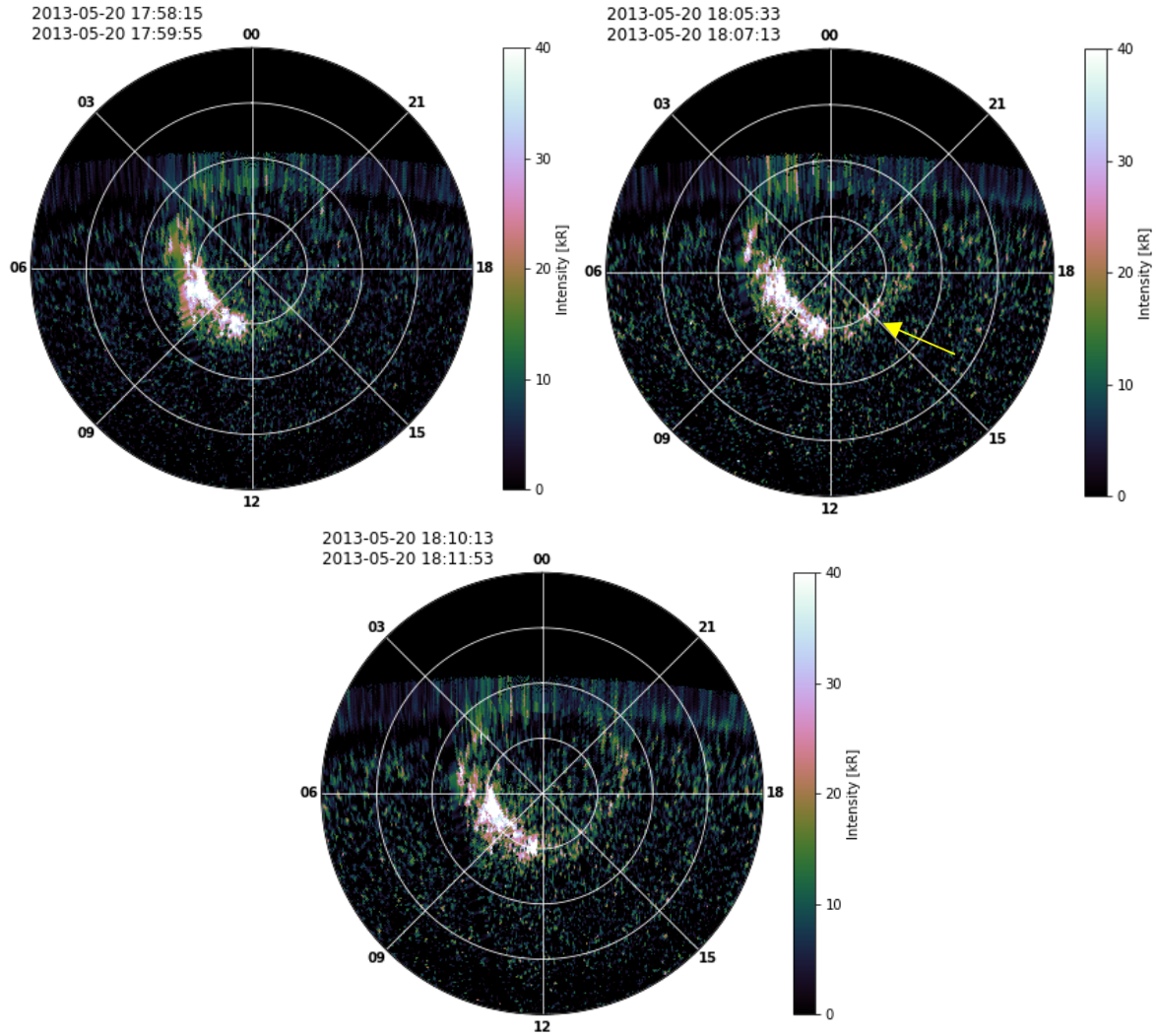
Figure A.5: HST images of Saturn's northern hemisphere in polar projection for the frames before (upper left), during (upper right), and after (lower centre) of the 2013-141 event. The yellow arrow indicates the flash region. 0-40° colatitude range was extracted hence the innermost ring in every plot stands for 10° colatitude (or 80° latitude) and each two rings are spaced by an increment of 10°. The longitude is represented in local hour starting from 0 at the top anti-clockwise, hence the dawn is at 6 LT, noon at 12 LT and dusk at 18 LT. The exposure time for the images is 100 sec.
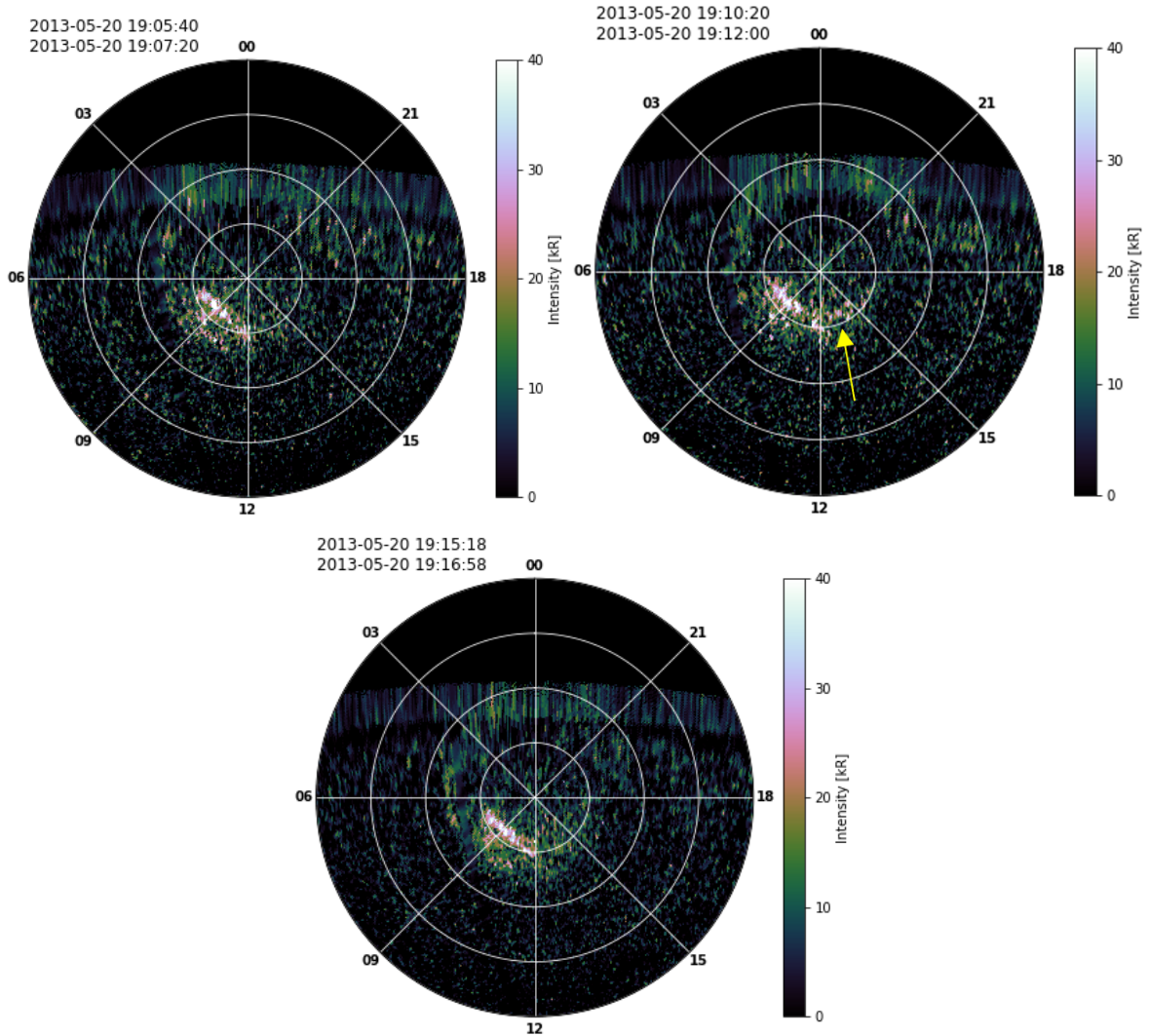
Figure A.6: HST images of Saturn's northern hemisphere in polar projection for the frames before (upper left), during (upper right), and after (lower centre) of the 2013-142 event. The yellow arrow indicates the transient auroral power intensification, while the blue arrow indicates possibly a faint persisting noon feature at the flash region. 0-40° colatitude range was extracted hence the innermost ring in every plot stands for 10° colatitude (or 80° latitude) and each two rings are spaced by an increment of 10°. The longitude is represented in local hour starting from 0 at the top anti-clockwise, hence the dawn is at 6 LT, noon at 12 LT and dusk at 18 LT. The exposure time for the images is 100 sec.
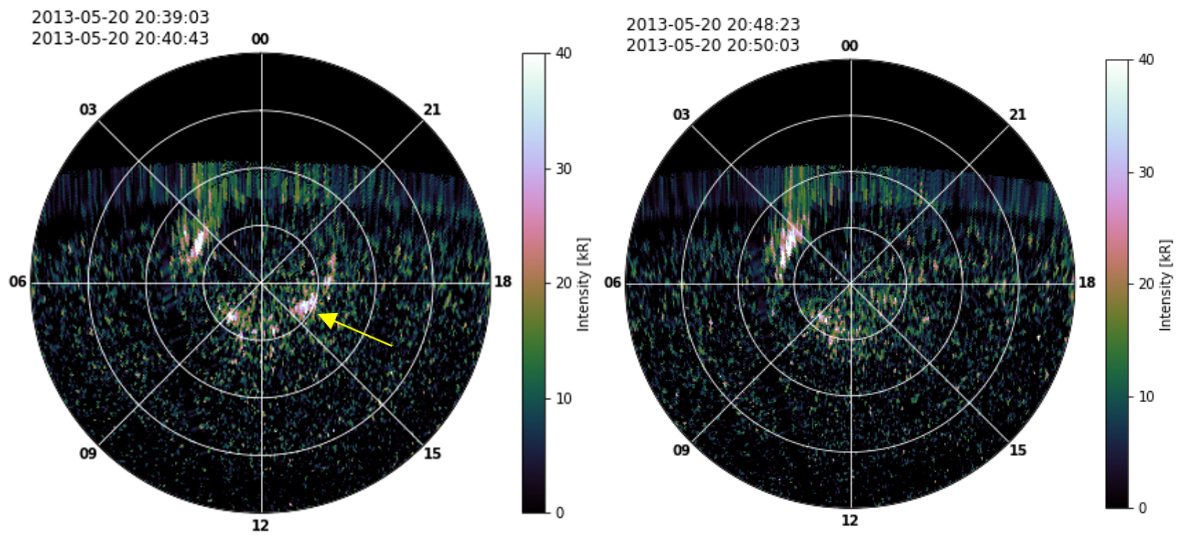
Figure A.7: HST images of Saturn's northern hemisphere in polar projection for the frames during (left) and after (right) the 2014-097 event. The yellow arrow indicates the transient auroral power intensification, while the blue arrow indicates the persisting dusk feature. The image is 0-40° colatitude range was extracted hence the innermost ring in every plot stands for 10° colatitude (or 80° latitude) and each two rings are spaced by an increment of 10°. The longitude is represented in local hour starting from 0 at the top anti-clockwise, hence the dawn is at 6 LT, noon at 12 LT and dusk at 18 LT. The exposure time for the images ranges from 270-350 sec.

Figure A.8: HST images of Saturn's northern hemisphere in polar projection for the frames during (left) and after (right) the 2014-102 event. The yellow arrow indicates the transient auroral power intensification, while the blue arrow indicates the persisting dusk feature. 0-40° colatitude range was extracted hence the innermost ring in every plot stands for 10° colatitude (or 80° latitude) and each two rings are spaced by an increment of 10°. The longitude is represented in local hour starting from 0 at the top anti-clockwise, hence the dawn is at 6 LT, noon at 12 LT and dusk at 18 LT. The exposure time for the images is 420 sec.
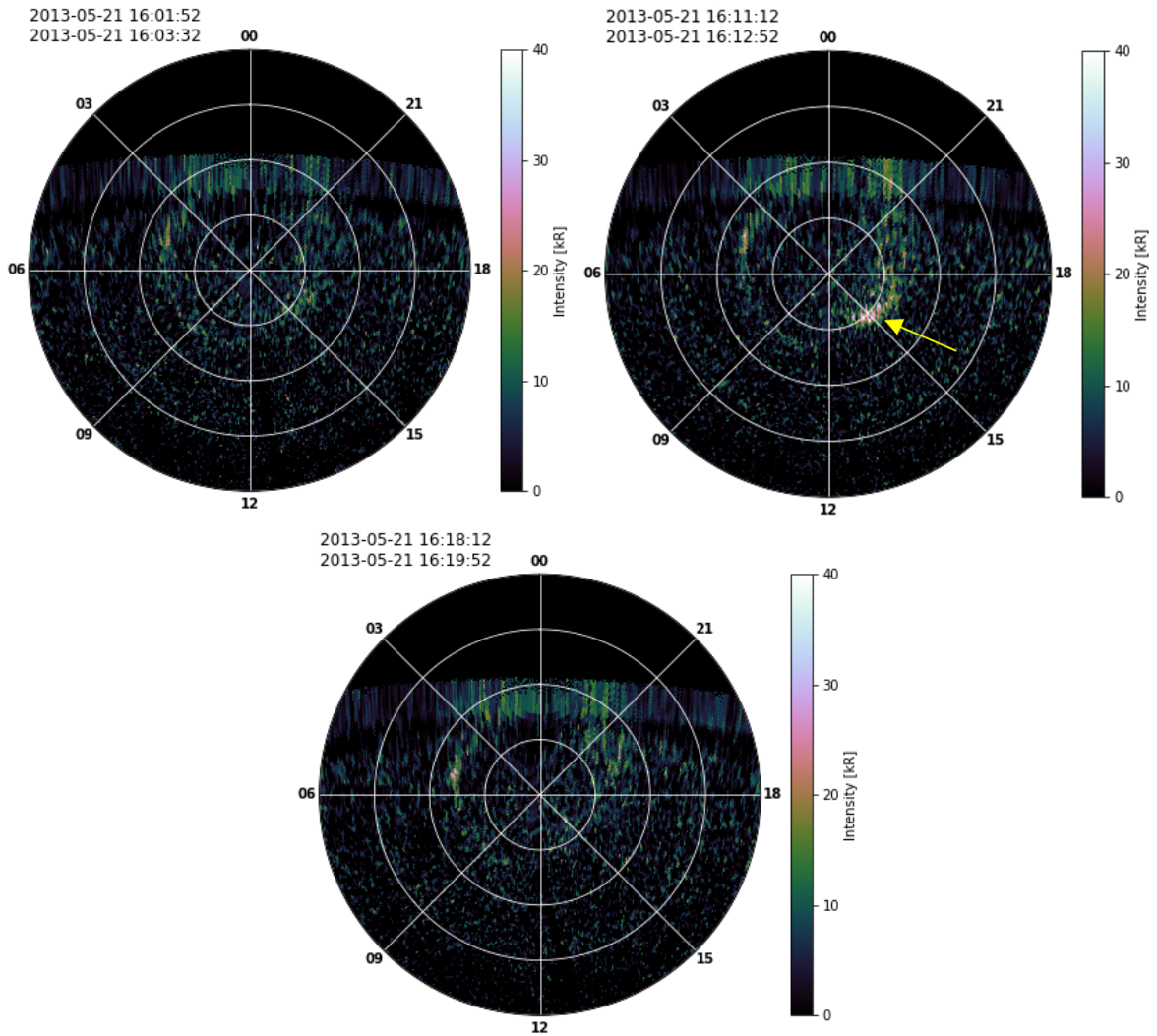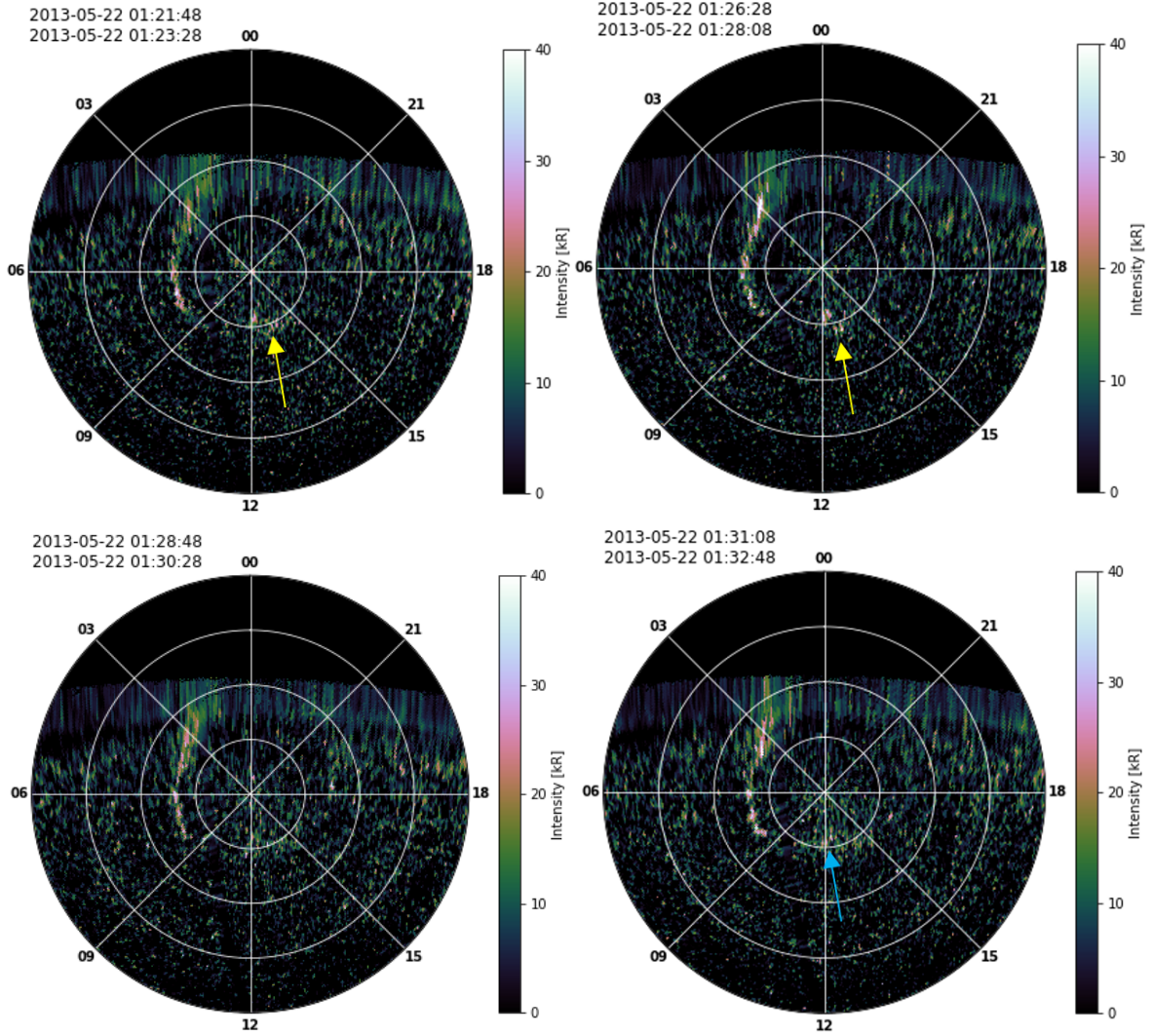
Figure A.9: HST images of Saturn's northern hemisphere in polar projection for the frames during (left) and after (right) 2014-145 event 1. The yellow arrow indicates the transient auroral power intensification. 0-40° colatitude range was extracted hence the innermost ring in every plot stands for 10° colatitude (or 80° latitude) and each two rings are spaced by an increment of 10°. The longitude is represented in local hour starting from 0 at the top anti-clockwise, hence the dawn is at 6 LT, noon at 12 LT and dusk at 18 LT. The exposure time for the images is 420 sec.

Figure A.10: HST images of Saturn's northern hemisphere in polar projection for the frames before (left) and during (right) 2014-145 event 2. The yellow arrow indicates the transient auroral power intensification. 0-40° colatitude range was extracted hence the innermost ring in every plot stands for 10° colatitude (or 80° latitude) and each two rings are spaced by an increment of 10°. The longitude is represented in local hour starting from 0 at the top anti-clockwise, hence the dawn is at 6 LT, noon at 12 LT and dusk at 18 LT. The exposure time for the images ranges from 190-420 sec.
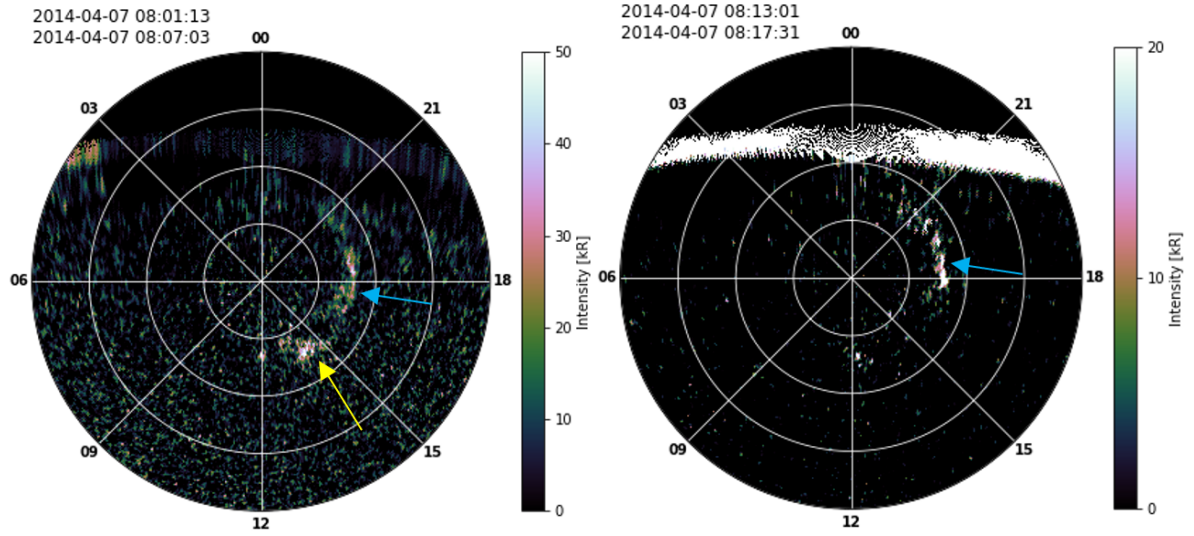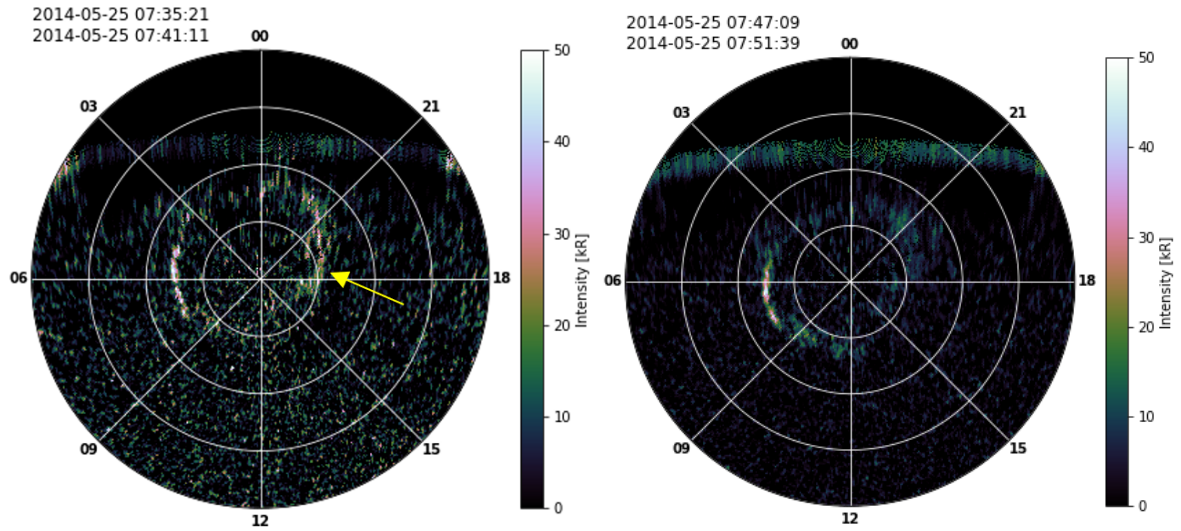
Figure A.11: HST images of Saturn's northern hemisphere in polar projection for the frames during (left) and after (right) 2014-145 event 3. The yellow arrow indicates the transient auroral power intensification. 0-40° colatitude range was extracted hence the innermost ring in every plot stands for 10° colatitude (or 80° latitude) and each two rings are spaced by an increment of 10°. The longitude is represented in local hour starting from 0 at the top anti-clockwise, hence the dawn is at 6 LT, noon at 12 LT and dusk at 18 LT. The exposure time for the images ranges from 270-350 sec.
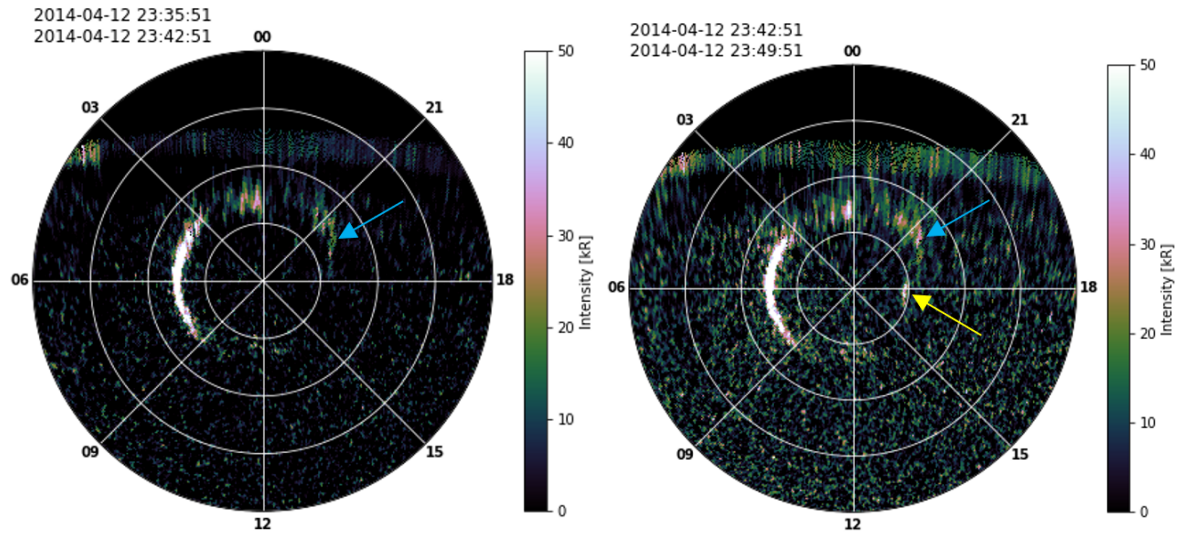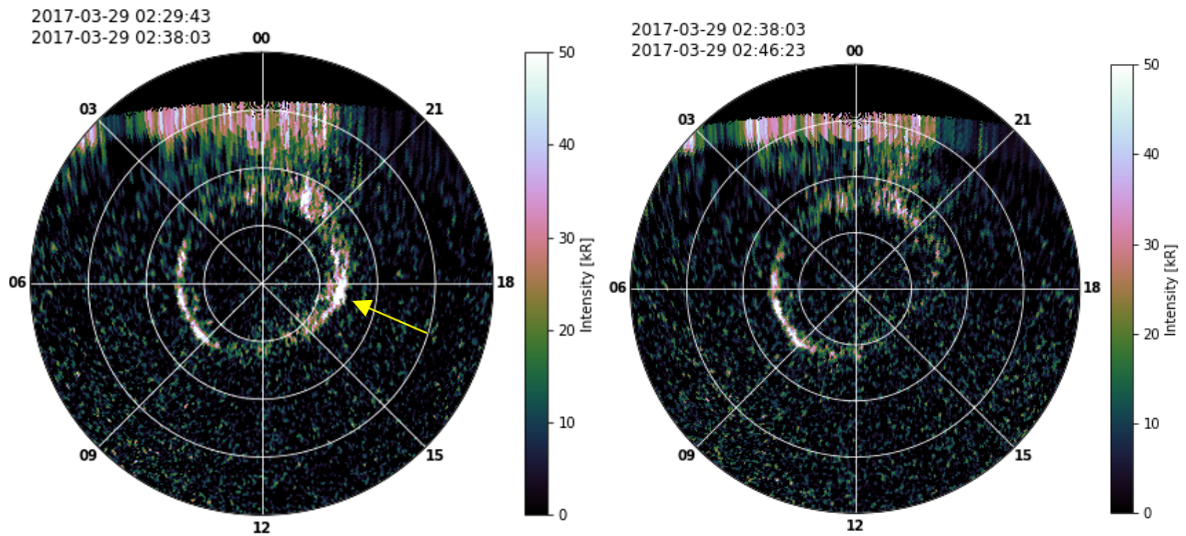

Figure A.12: HST images of Saturn's northern hemisphere in polar projection for the frames during (left) and after (right) the 2017-088 event. 0-40° colatitude range was extracted hence the innermost ring in every plot stands for 10° colatitude (or 80° latitude) and each two rings are spaced by an increment of 10°. The longitude is represented in local hour starting from 0 at the top anti-clockwise, hence the dawn is at 6 LT, noon at 12 LT and dusk at 18 LT. The exposure time for the images is 500 sec.
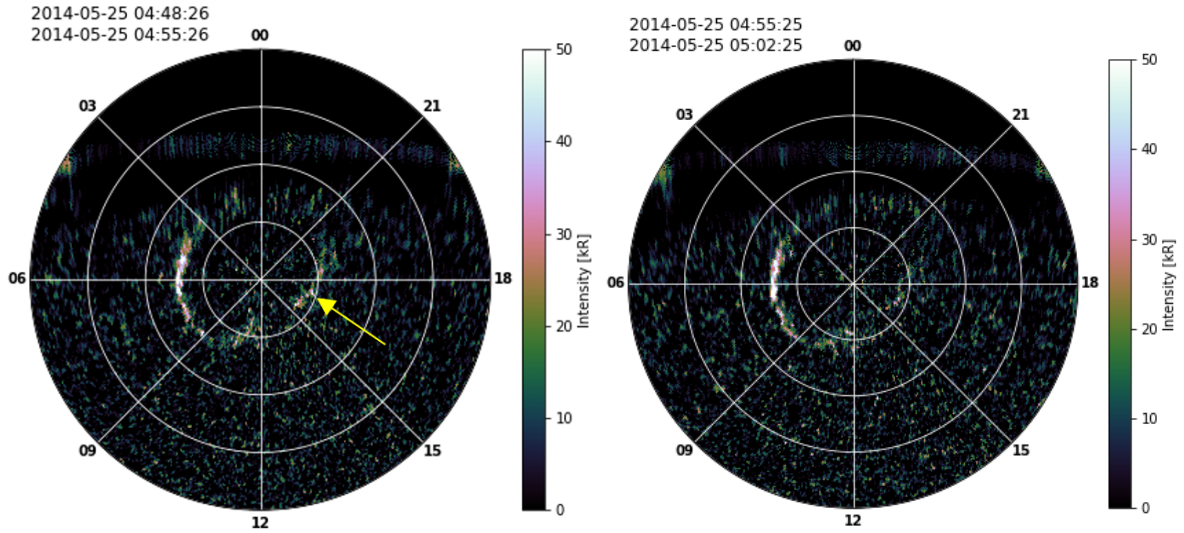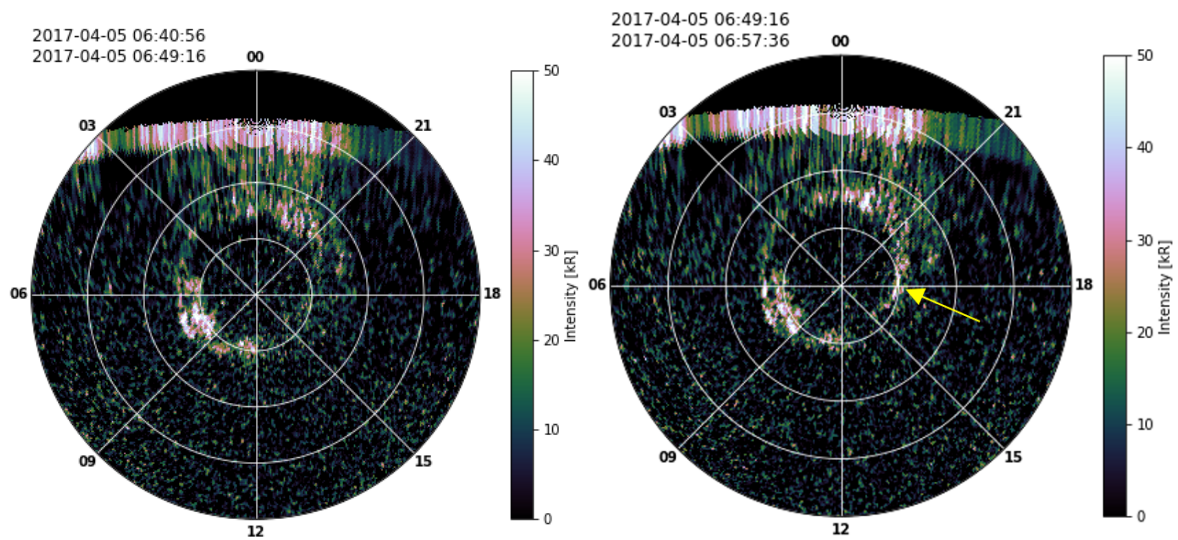
Figure A.13: HST images of Saturn's northern hemisphere in polar projection for the frames before (left) and during (right) the 2017-095 event. The yellow arrow indicates the transient auroral power intensification. 0-40° colatitude range was extracted hence the innermost ring in every plot stands for 10° colatitude (or 80° latitude) and each two rings are spaced by an increment of 10°. The longitude is represented in local hour starting from 0 at the top anti-clockwise, hence the dawn is at 6 LT, noon at 12 LT and dusk at 18 LT. The exposure time for the images is 500 sec.
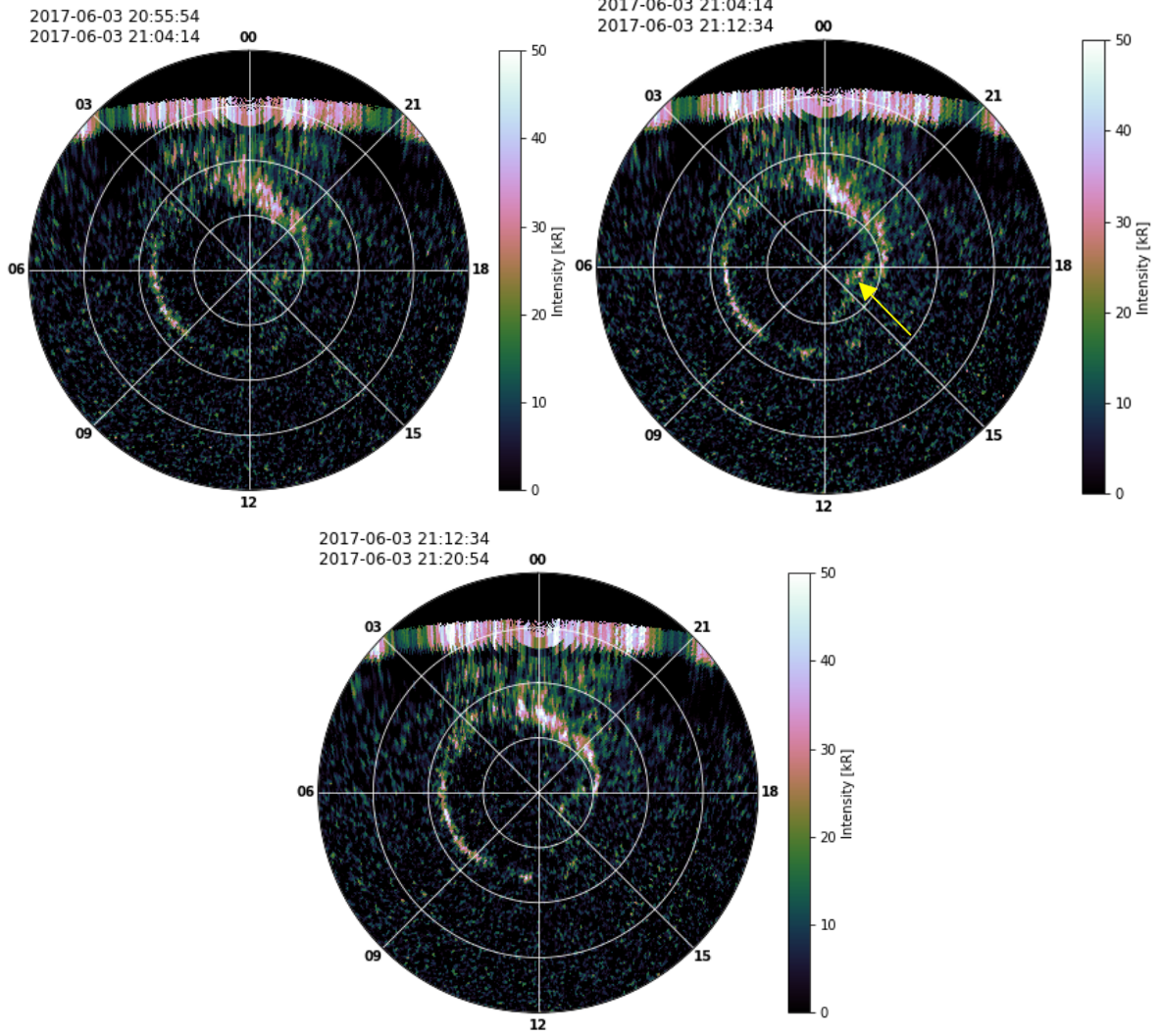
Figure A.14: HST images of Saturn's northern hemisphere in polar projection for the frames before (left) and during (right) the 2017-154 event. The yellow arrow indicates the transient auroral power intensification. 0-40° colatitude range was extracted hence the innermost ring in every plot stands for 10° colatitude (or 80° latitude) and each two rings are spaced by an increment of 10°. The longitude is represented in local hour starting from 0 at the top anti-clockwise, hence the dawn is at 6 LT, noon at 12 LT and dusk at 18 LT. The exposure time for the images is 500 sec.
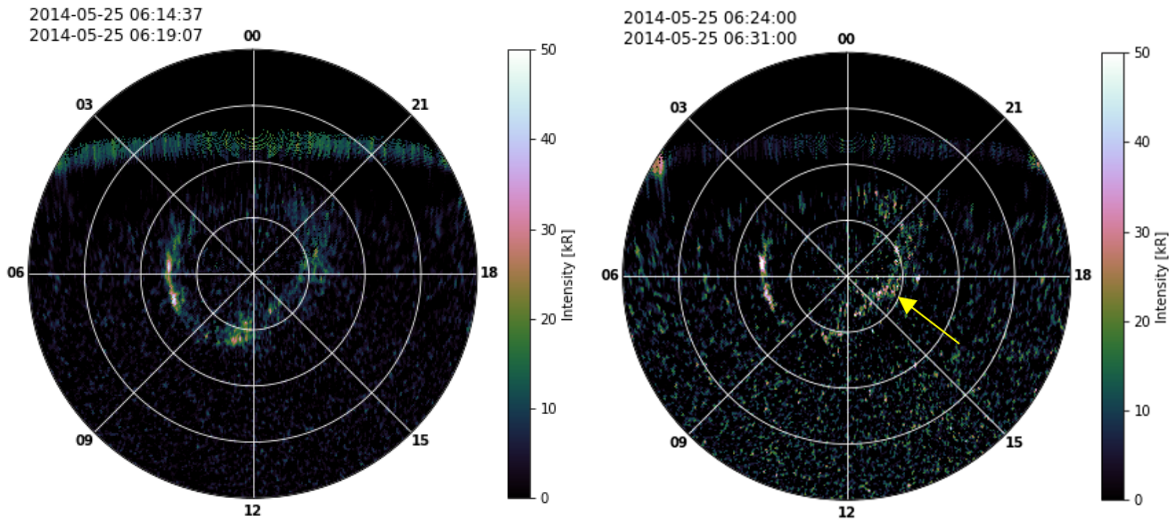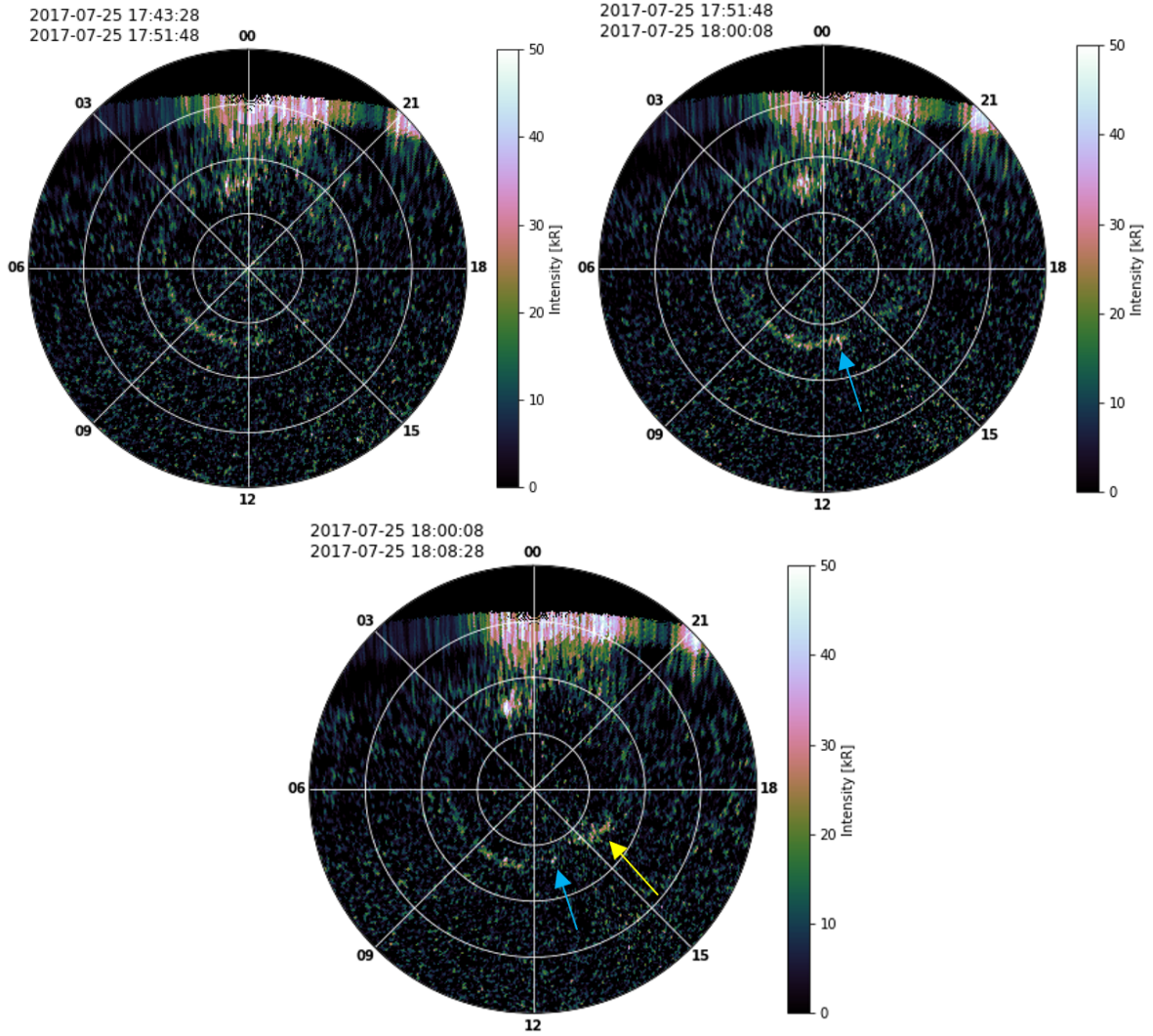
Figure A.15: HST images of Saturn's northern hemisphere in polar projection for the frames before (left) and during (right) the 2017-206 event. The yellow and blue arrows both indicate a possible transient auroral power intensification, but the feature marked with the blue arrow is more likely to be connected with the noon feature at 12 LT. 0-40° colatitude range was extracted hence the innermost ring in every plot stands for 10° colatitude (or 80° latitude) and each two rings are spaced by an increment of 10°. The longitude is represented in local hour starting from 0 at the top anti-clockwise, hence the dawn is at 6 LT, noon at 12 LT and dusk at 18 LT. The exposure time for the images is 500 sec.

References

Achilleos, N., Arridge, C., and Guio, P. (2008). Modeling of a giant planet magnetodisc. In *AGU Fall Meeting Abstracts*, volume 2008, pages P11B–1263.

Allegrini, F., Bagenal, F., Bolton, S., Connerney, J., Clark, G., Ebert, R., Kim, T., Kurth, W., Levin, S., Louarn, P., et al. (2017). Electron beams and loss cones in the auroral regions of jupiter. *Geophysical Research Letters*, 44(14):7131–7139.

Andrews, D., Cecconi, B., Cowley, S., Dougherty, M., Lamy, L., Provan, G., and Zarka, P. (2011). Planetary period oscillations in saturn's magnetosphere: Evidence in magnetic field phase data for rotational modulation of saturn kilometric radiation emissions. *Journal of Geophysical Research: Space Physics*, 116(A9).

Andrews, D., Cowley, S., Dougherty, M., and Provan, G. (2010). Magnetic field oscillations near the planetary period in saturn's equatorial magnetosphere: Variation of amplitude and phase with radial distance and local time. *Journal of Geophysical Research: Space Physics*, 115(A4).

Arridge, C., Achilleos, N., Dougherty, M., Khurana, K., and Russell, C. (2006). Modeling the size and shape of saturn's magnetopause with variable dynamic pressure. *Journal of Geophysical Research: Space Physics*, 111(A11).

Arridge, C., André, N., McAndrews, H., Bunce, E., Burger, M., Hansen, K., Hsu, H.-W., Johnson, R., Jones, G., Kempf, S., et al. (2011). Mapping magnetospheric equatorial regions at saturn from cassini prime mission observations. *Space science reviews*, 164(1):1–83.

Arridge, C., Khurana, K., Russell, C., Southwood, D., Achilleos, N., Dougherty, M., Coates, A., and Leinweber, H. (2008a). Warping of saturn's magnetospheric and magnetotail current sheets. *Journal of Geophysical Research: Space Physics*, 113(A8).

Arridge, C., Russell, C., Khurana, K., Achilleos, N., Cowley, S., Dougherty, M., Southwood, D., and Bunce, E. (2008b). Saturn's magnetodisc current sheet. *Journal of Geophysical Research: Space Physics*, 113(A4).

Arridge, C. S., Jasinski, J., Achilleos, N., Bogdanova, Y., Bunce, E., Cowley, S. W., Fazakerley, A., Khurana, K., Lamy, L., Leisner, J., et al. (2016). Cassini observations of saturn's southern polar cusp. *Journal of Geophysical Research: Space Physics*, 121(4):3006–3030.

Azari, A. R., Liemohn, M. W., Jia, X., Thomsen, M. F., Mitchell, D. G., Sergis, N., Rymer, A. M., Hospodarsky, G. B., Paranicas, C., and Vandegriff, J. (2018). Interchange injections at saturn: Statistical survey of energetic h+ sudden flux intensifications. *Journal of Geophysical Research: Space Physics*, 123(6):4692–4711.

Bader, A., Badman, S., Kinrade, J., Cowley, S., Provan, G., and Pryor, W. (2018). Statistical planetary period oscillation signatures in saturn's uv auroral intensity. *Journal of Geophysical Research: Space Physics*, 123(10):8459–8472.

Bader, A., Badman, S., Ray, L. C., Paranicas, C., Lorch, C., Clark, G., André, M., Mitchell, D. G., Constable, D. A., Kinrade, J., et al. (2020). Energetic particle signatures above saturn's aurorae. *Journal of Geophysical Research: Space Physics*, 125(1):e2019JA027403.

Bader, A., Badman, S. V., Yao, Z., Kinrade, J., and Pryor, W. (2019). Observations of continuous quasiperiodic auroral pulsations on saturn in high time-resolution uv auroral imagery. *Journal of Geophysical Research: Space Physics*, 124(4):2451–2465.

Badman, S., Achilleos, N., Baines, K., Brown, R., Bunce, E., Dougherty, M., Melin, H., Nichols, J., and Stallard, T. (2011). Location of saturn's northern infrared aurora determined from cassini vims images. *Geophysical research letters*, 38(3).

Badman, S., Bunce, E., Clarke, J., Cowley, S., Gérard, J.-C., Grodent, D., and Milan, S. (2005). Open flux estimates in saturn's magnetosphere during the january 2004 cassini-hst campaign, and implications for reconnection rates. *Journal of Geophysical Research: Space Physics*, 110(A11).

Badman, S. and Cowley, S. (2007). Significance of dungey-cycle flows in jupiter's and saturn's magnetospheres, and their identification on closed equatorial field lines. In *Annales Geophysicae*, volume 25, pages 941–951. Copernicus GmbH.

Badman, S. V., Achilleos, N., Arridge, C. S., Baines, K., Brown, R., Bunce, E., Coates, A. J., Cowley, S., Dougherty, M., Fujimoto, M., et al. (2012a). Cassini observations of ion and electron beams at saturn and their relationship to infrared auroral arcs. *Journal of Geophysical Research: Space Physics*, 117(A1).

Badman, S. V., Andrews, D. J., Cowley, S., Lamy, L., Provan, G., Tao, C., Kasahara, S., Kimura, T., Fujimoto, M., Melin, H., et al. (2012b). Rotational modulation and local time dependence of saturn's infrared h3+ auroral intensity. *Journal of Geophysical Research: Space Physics*, 117(A9).

Badman, S. V., Branduardi-Raymont, G., Galand, M., Hess, S. L., Krupp, N., Lamy, L., Melin, H., and Tao, C. (2015). Auroral processes at the giant planets: Energy deposition, emission mechanisms, morphology and spectra. *Space Science Reviews*, 187(1):99–179.

Badman, S. V., Jackman, C. M., Nichols, J. D., Clarke, J. T., and Gérard, J.-C. (2014). Open flux in saturn's magnetosphere. *Icarus*, 231:137–145.

Badman, S. V., Masters, A., Hasegawa, H., Fujimoto, M., Radioti, A., Grodent, D., Sergis, N., Dougherty, M., and Coates, A. J. (2013). Bursty magnetic reconnection at saturn's magnetopause. *Geophysical Research Letters*, 40(6):1027–1031.

Baumjohann, W. and Treumann, R. A. (2012). *Basic space plasma physics (revised edition)*. World Scientific Publishing Company.

Bradley, T., Cowley, S., Bunce, E., Melin, H., Provan, G., Nichols, J., Dougherty, M., Roussos, E., Krupp, N., Tao, C., et al. (2020). Saturn's nightside dynamics during cassini's f ring and proximal orbits: Response to solar wind and planetary period oscillation modulations. *Journal of Geophysical Research: Space Physics*, 125(9):e2020JA027907.

Bradley, T., Cowley, S., Bunce, E., Smith, A., Jackman, C., and Provan, G. (2018). Planetary period modulation of reconnection bursts in saturn's magnetotail. *Journal of Geophysical Research: Space Physics*, 123(11):9476–9507.

Brice, N. M. and Ioannidis, G. A. (1970). The magnetospheres of jupiter and earth. *Icarus*, 13(2):173–183.

Bunce, E., Arridge, C., Cowley, S., and Dougherty, M. (2008). Magnetic field structure of saturn's dayside magnetosphere and its mapping to the ionosphere: Results from ring current modeling. *Journal of Geophysical Research: Space Physics*, 113(A2).

Bunce, E., Cowley, S., Alexeev, I., Arridge, C., Dougherty, M., Nichols, J., and Russell, C. (2007). Cassini observations of the variation of saturn's ring current parameters with system size. *Journal of Geophysical Research: Space Physics*, 112(A10).

Bunce, E., Cowley, S., and Milan, S. (2005). Interplanetary magnetic field control of saturn's polar cusp aurora. In *Annales Geophysicae*, volume 23, pages 1405–1431. Copernicus GmbH.

Bunce, E. J., Grodent, D., Jinks, S., Andrews, D. J., Badman, S., Coates, A. J., Cowley, S., Dougherty, M., Kurth, W., Mitchell, D., et al. (2014). Cassini nightside observations of the oscillatory motion of saturn's northern auroral oval. *Journal of Geophysical Research: Space Physics*, 119(5):3528–3543.

Burton, M., Dougherty, M., and Russell, C. (2010). Saturn's internal planetary magnetic field. *Geophysical Research Letters*, 37(24).

Carbary, J., Kurth, W., and Mitchell, D. (2016). Short periodicities in low-frequency plasma waves at saturn. *Journal of Geophysical Research: Space Physics*, 121(7):6562–6572.

Carbary, J. and Mitchell, D. (2013). Periodicities in saturn's magnetosphere. *Reviews of Geophysics*, 51(1):1–30.

Carbary, J., Mitchell, D., Brandt, P., Paranicas, C., and Krimigis, S. (2008). Ena periodicities at saturn. *Geophysical research letters*, 35(7).

Chowdhury, M., Stallard, T., Baines, K., Provan, G., Melin, H., Hunt, G., Moore, L., O'Donoghue, J., Thomas, E. M., Wang, R., et al. (2022). Saturn's weather-driven aurorae modulate oscillations in the magnetic field and radio emissions. *Geophysical Research Letters*, 49(3):e2021GL096492.

Clark, G., Mauk, B., Haggerty, D., Paranicas, C., Kollmann, P., Rymer, A., Bunce, E., Cowley, S., Mitchell, D., Provan, G., et al. (2017). Energetic particle signatures of magnetic field-aligned potentials over jupiter's polar regions. *Geophysical Research Letters*, 44(17):8703–8711.

Clarke, J., Nichols, J., Gérard, J.-C., Grodent, D., Hansen, K., Kurth, W., Gladstone, G., Duval, J., Wannawichian, S., Bunce, E., et al. (2009). Response of jupiter's and saturn's auroral activity to the solar wind. *Journal of Geophysical Research: Space Physics*, 114(A5).

Connerney, J., Acuna, M., and Ness, N. (1981). Saturn's ring current and inner magnetosphere. *Nature (London)*, 292(5825):724–726.

Connerney, J., Acuna, M., and Ness, N. (1983). Currents in saturn's magnetosphere. *Journal of Geophysical Research: Space Physics*, 88(A11):8779–8789.

Connerney, J. E., Nekut, A., and Kuckes, A. (1980). Deep crustal electrical conductivity in the adirondacks. *Journal of Geophysical Research: Solid Earth*, 85(B5):2603–2614.

Cowley, S., Badman, S. V., Bunce, E., Clarke, J., Gérard, J.-C., Grodent, D., Jackman, C. M., Milan, S. E., and Yeoman, T. K. (2005). Reconnection in a rotation-dominated magnetosphere and its relation to saturn's auroral dynamics. *Journal of Geophysical Research: Space Physics*, 110(A2).

Cowley, S. and Bunce, E. (2001). Origin of the main auroral oval in jupiter's coupled magnetosphere–ionosphere system. *Planetary and Space Science*, 49(10-11):1067–1088.

Cowley, S. and Bunce, E. (2003). Corotation-driven magnetosphere-ionosphere coupling currents in saturn's magnetosphere and their relation to the auroras. In *Annales Geophysicae*, volume 21, pages 1691–1707. Copernicus GmbH.

Cowley, S., Bunce, E., and O'Rourke, J. (2004a). A simple quantitative model of plasma flows and currents in saturn's polar ionosphere. *Journal of Geophysical Research: Space Physics*, 109(A5).

Cowley, S., Bunce, E., and Prangé, R. (2004b). Saturn's polar ionospheric flows and their relation to the main auroral oval. In *Annales Geophysicae*, volume 22, pages 1379–1394. Copernicus GmbH.

Cowley, S. and Provan, G. (2017). Planetary period modulations of saturn's magnetotail current sheet during northern spring: Observations and modeling. *Journal of Geophysical Research: Space Physics*, 122(6):6049–6077.

Crary, F. J., Clarke, J. T., Dougherty, M. K., Hanlon, P., Hansen, K., Steinberg, J. T., Barraclough, B., Coates, A. J., Gérard, J.-C., Grodent, D., et al. (2005). Solar wind dynamic pressure and electric field as the main factors controlling saturn's aurorae. *Nature*, 433(7027):720–722.

Delamere, P. A., Otto, A., Ma, X., Bagenal, F., and Wilson, R. J. (2015). Magnetic flux circulation in the rotationally driven giant magnetospheres. *Journal of Geophysical Research: Space Physics*, 120(6):4229–4245.

Dougherty, M. K., Cao, H., Khurana, K. K., Hunt, G. J., Provan, G., Kellock, S., Burton, M. E., Burk, T. A., Bunce, E. J., Cowley, S. W., et al. (2018). Saturn's magnetic field revealed by the cassini grand finale. *Science*, 362(6410):eaat5434.

Dungey, J. W. (1961). Interplanetary magnetic field and the auroral zones. *Physical Review Letters*, 6(2):47.

Ergun, R., Carlson, C., McFadden, J., Mozer, F., Delory, G., Peria, W., Chaston, C., Temerin, M., Elphic, R., Strangeway, R., et al. (1998). Fast satellite observations of electric field structures in the auroral zone. *Geophysical research letters*, 25(12):2025–2028.

Gérard, J.-C., Grodent, D., Gustin, J., Saglam, A., Clarke, J. T., and Trauger, J. T. (2004). Characteristics of saturn's fuv aurora observed with the space telescope imaging spectrograph. *Journal of Geophysical Research: Space Physics*, 109(A9).

Gombosi, T. I., Armstrong, T. P., Arridge, C. S., Khurana, K. K., Krimigis, S. M., Krupp, N., Persoon, A. M., and Thomsen, M. F. (2009). Saturn's magnetospheric configuration. In *Saturn from Cassini-Huygens*, pages 203–255. Springer.

Grodent, D. (2015). A brief review of ultraviolet auroral emissions on giant planets. *Space Science Reviews*, 187(1):23–50.

Grodent, D., Gérard, J.-C., Cowley, S., Bunce, E., and Clarke, J. (2005). Variable morphology of saturn's southern ultraviolet aurora. *Journal of Geophysical Research: Space Physics*, 110(A7).

Grodent, D., Gustin, J., Gérard, J.-C., Radioti, A., Bonfond, B., and Pryor, W. (2011). Small-scale structures in saturn's ultraviolet aurora. *Journal of Geophysical Research: Space Physics*, 116(A9).

Grodent, D., Radioti, A., Bonfond, B., and Gérard, J.-C. (2010). On the origin of saturn's outer auroral emission. *Journal of Geophysical Research: Space Physics*, 115(A8).

Guio, P., Staniland, N., Achilleos, N., and Arridge, C. (2020). Trapped particle motion in magnetodisk fields. *Journal of Geophysical Research: Space Physics*, 125(7):e2020JA027827.

Guo, R., Yao, Z., Sergis, N., Wei, Y., Mitchell, D., Roussos, E., Palmaerts, B., Dunn, W., Radioti, A., Ray, L. C., et al. (2018a). Reconnection acceleration in saturn's dayside magnetodisk: A multicase study with cassini. *The Astrophysical Journal Letters*, 868(2):L23.

Guo, R., Yao, Z., Wei, Y., Ray, L. C., Rae, I., Arridge, C. S., Coates, A., Delamere, P., Sergis, N., Kollmann, P., et al. (2018b). Rotationally driven magnetic reconnection in saturn's dayside. *Nature Astronomy*, 2(8):640–645.

Gurnett, D., Lecacheux, A., Kurth, W., Persoon, A., Groene, J., Lamy, L., Zarka, P., and Carbary, J. (2009). Discovery of a north-south asymmetry in saturn's radio rotation period. *Geophysical Research Letters*, 36(16).

Gustin, J., Bonfond, B., Grodent, D., and Gérard, J.-C. (2012). Conversion from hst acs and stis auroral counts into brightness, precipitated power, and radiated power for h2 giant planets. *Journal of Geophysical Research: Space Physics*, 117(A7).

Hill, T., Rymer, A., Burch, J., Crary, F., Young, D., Thomsen, M., Delapp, D., André, N., Coates, A., and Lewis, G. (2005). Evidence for rotationally driven plasma transport in saturn's magnetosphere. *Geophysical Research Letters*, 32(14).

Hunt, G., Cowley, S., Provan, G., Bunce, E., Alexeev, I, Belenkaya, E., Kalegaev, V., Dougherty, M., and Coates, A. (2015). Field-aligned currents in saturn's northern nightside magnetosphere: Evidence for interhemispheric current flow associated with planetary period oscillations. *Journal of Geophysical Research: Space Physics*, 120(9):7552–7584.

Hunt, G., Provan, G., Cowley, S., Dougherty, M., and Southwood, D. (2018). Saturn's planetary period oscillations during the closest approach of cassini's ring-grazing orbits. *Geophysical Research Letters*, 45(10):4692–4700.

Hunt, G. J., Cowley, S. W., Provan, G., Bunce, E. J., Alexeev, I. I., Belenkaya, E. S., Kalegaev, V. V., Dougherty, M. K., and Coates, A. J. (2014). Field-aligned currents in saturn's southern nightside magnetosphere: Subcorotation and planetary period oscillation components. *Journal of Geophysical Research: Space Physics*, 119(12):9847–9899.

Jackman, C. (2013). Saturn's magnetotail dynamics: A study of reconnection signatures. In *European Planetary Science Congress*, pages EPSC2013–320.

Jia, X., Kivelson, M. G., and Gombosi, T. I. (2012). Driving saturn's magnetospheric periodicities from the upper atmosphere/ionosphere. *Journal of Geophysical Research: Space Physics*, 117(A4).

Kellett, S., Arridge, C. S., Bunce, E., Coates, A. J., Cowley, S., Dougherty, M., Persoon, A., Sergis, N., and Wilson, R. (2010). Nature of the ring current in saturn's dayside magnetosphere. *Journal of Geophysical Research: Space Physics*, 115(A8).

Kellett, S., Arridge, C. S., Bunce, E., Coates, A. J., Cowley, S., Dougherty, M., Persoon, A., Sergis, N., and Wilson, R. (2011). Saturn's ring current: Local time dependence and temporal variability. *Journal of Geophysical Research: Space Physics*, 116(A5).

Kellett, S., Bunce, E., Coates, A., and Cowley, S. (2009). Thickness of saturn's ring current determined from north-south cassini passes through the current layer. *Journal of Geophysical Research: Space Physics*, 114(A4).

Kinrade, J., Badman, S. V., Bunce, E., Tao, C., Provan, G., Cowley, S., Grocott, A., Gray, R., Grodent, D., Kimura, T., et al. (2017). An isolated, bright cusp aurora at saturn. *Journal of Geophysical Research: Space Physics*, 122(6):6121–6138.

Kivelson, M. and Southwood, D. (2005). Dynamical consequences of two modes of centrifugal instability in jupiter's outer magnetosphere. *Journal of Geophysical Research: Space Physics*, 110(A12).

Kivelson, M. G. (2015). Adventures in parameter space: Reconnection and the magnetospheres of the solar system. In *Magnetospheric Plasma Physics: The Impact of Jim Dungey's Research*, pages 199–219. Springer.

Kollmann, P., Roussos, E., Kotova, A., Regoli, L., Mitchell, D., Carbary, J., Clark, G., Krupp, N., and Paranicas, C. (2018). Saturn's innermost radiation belt throughout and inward of the d-ring. *Geophysical Research Letters*, 45(20):10–912.

Kollmann, P., Roussos, E., Paranicas, C., Krupp, N., and Haggerty, D. (2013). Processes forming and sustaining saturn's proton radiation belts. *Icarus*, 222(1):323–341.

Kurth, W., Hospodarsky, G., Gurnett, D., Lamy, L., Dougherty, M., Nichols, J., Bunce, E., Pryor, W., Baines, K., Stallard, T., et al. (2016). Saturn kilometric radiation intensities during the saturn auroral campaign of 2013. *Icarus*, 263:2–9.

Lamy, L., Prangé, R., Tao, C., Kim, T., Badman, S., Zarka, P., Cecconi, B., Kurth, W., Pryor, W., Bunce, E., et al. (2018). Saturn's northern aurorae at solstice from hst observations coordinated with cassini's grand finale. *Geophysical Research Letters*, 45(18):9353–9362.

Mauk, B. H., Haggerty, D., Paranicas, C., Clark, G., Kollmann, P., Rymer, A., Bolton, S., Levin, S., Adriani, A., Allegrini, F., et al. (2017). Discrete and broadband electron acceleration in jupiter's powerful aurora. *Nature*, 549(7670):66–69.

Meredith, C., Cowley, S., Hansen, K., Nichols, J., and Yeoman, T. (2013). Simultaneous conjugate observations of small-scale structures in saturn's dayside ultraviolet auroras: Implications for physical origins. *Journal of Geophysical Research: Space Physics*, 118(5):2244–2266.

Mitchell, D., Brandt, P., Carbary, J., Kurth, W., Krimigis, S., Paranicas, C., and Pryor, W. (2015). Injection, interchange, and reconnection: Energetic particle observations in saturn's magnetosphere. *Magnetotails in the solar system*, pages 327–343.

Mitchell, D., Carbary, J., Bunce, E., Radioti, A., Badman, S. V., Pryor, W. R., Hospodarsky, G., and Kurth, W. (2016). Recurrent pulsations in saturn's high latitude magnetosphere. *Icarus*, 263:94–100.

Mitchell, D., Krimigis, S., Paranicas, C., Brandt, P., Carbary, J., Roelof, E., Kurth, W., Gurnett, D., Clarke, J., Nichols, J., et al. (2009). Recurrent energization of plasma in the midnight-to-dawn quadrant of saturn's magnetosphere, and its relationship to auroral uv and radio emissions. *Planetary and Space Science*, 57(14-15):1732–1742.

Morooka, M., Modolo, R., Wahlund, J.-E., André, M., Eriksson, A., Persoon, A., Gurnett, D., Kurth, W., Coates, A., Lewis, G., et al. (2009). The electron density of saturn's magnetosphere. In *Annales Geophysicae*, volume 27, pages 2971–2991. Copernicus GmbH.

Ness, N. F., Acuña, M. H., Behannon, K. W., Burlaga, L. F., Connerney, J. E., Lepping, R. P., and Neubauer, F. M. (1982). Magnetic field studies by voyager 2: Preliminary results at saturn. *Science*, 215(4532):558–563.

Nichols, J., Cecconi, B., Clarke, J., Cowley, S., Gérard, J.-C., Grocott, A., Grodent, D., Lamy, L., and Zarka, P. (2010a). Variation of saturn's uv aurora with skr phase. *Geophysical Research Letters*, 37(15).

Nichols, J., Cowley, S., and Lamy, L. (2010b). Dawn-dusk oscillation of saturn's conjugate auroral ovals. *Geophysical Research Letters*, 37(24).

Nichols, J. D., Badman, S., Bunce, E., Clarke, J., Cowley, S. W. H., Hunt, G., and Provan, G. (2016). Saturn's northern auroras as observed using the hubble space telescope. *Icarus*, 263:17–31.

Nichols, J. D., Clarke, J., Cowley, S., Duval, J., Farmer, A., Gérard, J.-C., Grodent, D., and Wannawichian, S. (2008). Oscillation of saturn's southern auroral oval. *Journal of Geophysical Research: Space Physics*, 113(A11).

Palmaerts, B., Roussos, E., Krupp, N., Kurth, W. S., Mitchell, D. G., and Yates, J. N. (2016). Statistical analysis and multi-instrument overview of the quasi-periodic 1-hour pulsations in saturn's outer magnetosphere. *Icarus*, 271:1–18.

Pan, D.-X., Yao, Z.-H., Guo, R.-L., Bonfond, B., Wei, Y., Dunn, W., Zhang, B.-Z., Zong, Q.-G., Zhou, X.-Z., Grodent, D., et al. (2021). A statistical survey of low-frequency magnetic fluctuations at saturn. *Journal of Geophysical Research: Space Physics*, 126(2):e2020JA028387.

Paranicas, C., Mitchell, D., Roelof, E., Brandt, P., Williams, D., Krimigis, S., and Mauk, B. (2005). Periodic intensity variations in global ena images of saturn. *Geophysical Research Letters*, 32(21).

Pilkington, N., Achilleos, N., Arridge, C., Guio, P., Masters, A., Ray, L., Sergis, N., Thomsen, M., Coates, A., and Dougherty, M. (2015). Asymmetries observed in saturn's magnetopause geometry. *Geophysical research letters*, 42(17):6890–6898.

Prolss, G. W. (2004). *Physics of the Earth's space environment: an introduction.* Springer.

Provan, G., Andrews, D., Cecconi, B., Cowley, S., Dougherty, M., Lamy, L., and Zarka, P. (2011). Magnetospheric period magnetic field oscillations at saturn: Equatorial phase "jitter" produced by superposition of southern and northern period oscillations. *Journal of Geophysical Research: Space Physics*, 116(A4).

Provan, G., Andrews, D. J., Arridge, C. S., Coates, A. J., Cowley, S., Cox, G., Dougherty, M., and Jackman, C. (2012). Dual periodicities in planetary-period magnetic field oscillations in saturn's tail. *Journal of Geophysical Research: Space Physics*, 117(A1).

Provan, G., Bradley, T., Bunce, E., Cowley, S., Cao, H., Dougherty, M., Hunt, G. J., Roussos, E., Staniland, N., and Tao, C. (2021). Saturn's nightside ring current during cassini's grand finale. *Journal of Geophysical Research: Space Physics*, 126(3):e2020JA028605.

Provan, G., Cowley, S., Bradley, T., Bunce, E., Hunt, G., Cao, H., and Dougherty, M. (2019). Magnetic field observations on cassini's proximal periapsis passes: Planetary period oscillations and mean residual fields. *Journal of Geophysical Research: Space Physics*, 124(11):8814–8864.

Provan, G., Cowley, S., Bradley, T., Bunce, E., Hunt, G., and Dougherty, M. (2018a). Planetary period oscillations in saturn's magnetosphere: Cassini magnetic field observations over the northern summer solstice interval. *Journal of Geophysical Research: Space Physics*, 123(5):3859–3899.

Provan, G., Cowley, S., Bradley, T., Bunce, E. J., Hunt, G. J., Lamy, L., and Dougherty, M. K. (2018b). Saturn's planetary period oscillations observed throughout the cassini mission. In *AGU Fall Meeting Abstracts*, volume 2018, pages SM52A–05.

Provan, G., Cowley, S., and Nichols, J. (2009). Phase relation of oscillations near the planetary period of saturn's auroral oval and the equatorial magnetospheric magnetic field. *Journal of Geophysical Research: Space Physics*, 114(A4).

Pryor, W. R., Rymer, A. M., Mitchell, D. G., Hill, T. W., Young, D. T., Saur, J., Jones, G. H., Jacobsen, S., Cowley, S. W., Mauk, B. H., et al. (2011). The auroral footprint of enceladus on saturn. *Nature*, 472(7343):331–333.

Radioti, A., Grodent, D., Gérard, J.-C., Bonfond, B., Gustin, J., Pryor, W., Jasinski, J., and Arridge, C. (2013). Auroral signatures of multiple magnetopause reconnection at saturn. *Geophysical Research Letters*, 40(17):4498–4502.

Radioti, A., Grodent, D., Gérard, J.-C., Milan, S., Bonfond, B., Gustin, J., and Pryor, W. (2011). Bifurcations of the main auroral ring at saturn: Ionospheric signatures of consecutive reconnection events at the magnetopause. *Journal of Geophysical Research: Space Physics*, 116(A11).

Radioti, A., Grodent, D., Gérard, J.-C., Southwood, D., Chané, E., Bonfond, B., and Pryor, W. (2017a). Stagnation of saturn's auroral emission at noon. *Journal of Geophysical Research: Space Physics*, 122(6):6078–6087.

Radioti, A., Grodent, D., Yao, Z., Gérard, J.-C., Badman, S., Pryor, W., and Bonfond, B. (2017b). Dawn auroral breakup at saturn initiated by auroral arcs: Uvis/cassini beginning of grand finale phase. *Journal of Geophysical Research: Space Physics*, 122(12):12–111.

Radioti, A., Tomás, A. T., Grodent, D., Gérard, J.-C., Gustin, J., Bonford, B., Krupp, N., Woch, J., and Menietti, J. D. (2009). Equatorward diffuse auroral emissions at jupiter: Simultaneous hst and galileo observations. *Geophysical Research Letters*, 36(7).

Ray, L. and Ergun, R. (2012). Auroral signatures of ionosphere-magnetosphere coupling at jupiter and saturn. *Washington, DC: American Geophysical Union Geophysical Monograph Series*, 197.

Richardson, J. D. and Sittler Jr, E. (1990). A plasma density model for saturn based on voyager observations. *Journal of Geophysical Research: Space Physics*, 95(A8):12019–12031.

Roussos, E., Kollmann, P., Krupp, N., Kotova, A., Regoli, L., Paranicas, C., Mitchell, D., Krimigis, S., Hamilton, D., Brandt, P., et al. (2018). A radiation belt of energetic protons located between saturn and its rings. *Science*, 362(6410):eaat1962.

Roussos, E., Krupp, N., Armstrong, T., Paranicas, C., Mitchell, D., Krimigis, S., Jones, G., Dialynas, K., Sergis, N., and Hamilton, D. (2008). Discovery of a transient radiation belt at saturn. *Geophysical Research Letters*, 35(22).

Roussos, E., Krupp, N., Mitchell, D., Paranicas, C., Krimigis, S., Andriopoulou, M., Palmaerts, B., Kurth, W., Badman, S., Masters, A., et al. (2016). Quasi-periodic injections of relativistic electrons in saturn's outer magnetosphere. *Icarus*, 263:101–116.

Roussos, E., Krupp, N., Paranicas, C., Carbary, J., Kollmann, P., Krimigis, S. M., and Mitchell, D. (2014). The variable extension of saturn s electron radiation belts. *Planetary and Space Science*, 104:3–17.

Roussos, E., Krupp, N., Paranicas, C., Kollmann, P., Mitchell, D., Krimigis, S., Armstrong, T., Went, D., Dougherty, M., and Jones, G. H. (2011). Long-and short-term variability of saturn's ionic radiation belts. *Journal of Geophysical Research: Space Physics*, 116(A2).

Rusaitis, L., Khurana, K. K., Kivelson, M., and Walker, R. J. (2021). Quasiperiodic 1-hour alfvén wave resonances in saturn's magnetosphere: Theory for a realistic plasma/field model. *Geophysical Research Letters*, 48(7):e2020GL090967.

Rusaitis, L., Kivelson, M., Khurana, K. K., Strangeway, R. J., and Walker, R. J. (2018). Quasi-periodic 1-hour pulsations in saturn's outer magnetosphere. In *AGU Fall Meeting Abstracts*, volume 2018, pages SM23E–3242.

Saur, J., Janser, S., Schreiner, A., Clark, G., Mauk, B. H., Kollmann, P., Ebert, R. W., Allegrini, F., Szalay, J. R., and Kotsiaros, S. (2018). Wave-particle interaction of

alfvén waves in jupiter's magnetosphere: Auroral and magnetospheric particle acceleration. *Journal of Geophysical Research: Space Physics*, 123(11):9560–9573.

Schippers, P., Blanc, M., André, N., Dandouras, I., Lewis, G., Gilbert, L., Persoon, A., Krupp, N., Gurnett, D., Coates, A., et al. (2008). Multi-instrument analysis of electron populations in saturn's magnetosphere. *Journal of Geophysical Research: Space Physics*, 113(A7).

Schippers, P., Moncuquet, M., and Meyer-Vernet, N. (2012). Analysis of the large-scale structure of electrons in saturn's inner magnetosphere from the quasi-thermal noise observed with cassini/rpws antennas. In *European Planetary Science Congress 2012*, pages EPSC2012–551.

Sergis, N., Jackman, C., Thomsen, M., Krimigis, S., Mitchell, D., Hamilton, D., Dougherty, M., Krupp, N., and Wilson, R. (2017). Radial and local time structure of the saturnian ring current, revealed by cassini. *Journal of Geophysical Research: Space Physics*, 122(2):1803–1815.

Shprits, Y. Y., Menietti, J. D., Drozdov, A. Y., Horne, R. B., Woodfield, E. E., Groene, J. B., de Soria-Santacruz, M., Averkamp, T. F., Garrett, H., Paranicas, C., et al. (2018). Strong whistler mode waves observed in the vicinity of jupiter's moons. *Nature communications*, 9(1):1–6.

Smith, C. (2011). A saturnian cam current system driven by asymmetric thermospheric heating. *Monthly Notices of the Royal Astronomical Society*, 410(4):2315–2328.

Smith, E., Davis Jr, L., Jones, D., Coleman Jr, P. J., Colburn, D., Dyal, P., and Sonett, C. (1980). Saturn's magnetic field and magnetosphere. *Science*, 207(4429):407–410.

Sorba, A., Achilleos, N., Sergis, N., Guio, P., Arridge, C., and Dougherty, M. (2019). Local time variation in the large-scale structure of saturn's magnetosphere. *Journal of Geophysical Research: Space Physics*, 124(9):7425–7441.

Southwood, D. and Cowley, S. W. H. (2014). The origin of saturn's magnetic periodicities: Northern and southern current systems. *Journal of Geophysical Research: Space Physics*, 119(3):1563–1571.

Southwood, D. J. and Kivelson, M. G. (1987). Magnetospheric interchange instability. *Journal of Geophysical Research: Space Physics*, 92(A1):109–116.

Stallard, T., Miller, S., Lystrup, M., Achilleos, N., Bunce, E. J., Arridge, C. S., Dougherty, M. K., Cowley, S. W., Badman, S. V., Talboys, D. L., et al. (2008). Complex structure within saturn's infrared aurora. *Nature*, 456(7219):214–217.

Tao, C., Badman, S. V., and Fujimoto, M. (2011). Uv and ir auroral emission model for the outer planets: Jupiter and saturn comparison. *Icarus*, 213(2):581–592.

Thomas, N., Bagenal, F., Hill, T., and Wilson, J. (2004). The io neutral clouds and plasma torus. *Jupiter. The planet, satellites and magnetosphere*, 1:561–591.

Thomsen, M. and Coates, A. (2019). Saturn's plasmapause: Signature of magnetospheric dynamics. *Journal of Geophysical Research: Space Physics*, 124(11):8804–8813.

Vasyliunas, V. M. (1983). Physics of the jovian magnetosphere. 11. plasma distribution and flow. *Physics of the Jovian magnetosphere*, pages 395–453.

Wilson, R., Tokar, R., and Henderson, M. (2009). Thermal ion flow in saturn's inner magnetosphere measured by the cassini plasma spectrometer: A signature of the enceladus torus? *Geophysical research letters*, 36(23).

Yao, Z., Dunn, W. R., Woodfield, E. E., Clark, G., Mauk, B. H., Ebert, R. W., Grodent, D., Bonfond, B., Pan, D., Rae, I. J., et al. (2021). Revealing the source of jupiter's x-ray auroral flares. *Science Advances*, 7(28):eabf0851.

Yao, Z., Radioti, A., Rae, I., Liu, J., Grodent, D., Ray, L., Badman, S., Coates, A., Gérard, J.-C., Waite, J., et al. (2017). Mechanisms of saturn's near-noon transient aurora: In situ evidence from cassini measurements. *Geophysical Research Letters*, 44(22):11–217.

Yates, J. N., Southwood, D., Dougherty, M., Sulaiman, A. H., Masters, A., Cowley, S. W., Kivelson, M., Chen, C. H., Provan, G., Mitchell, D. G., et al. (2016). Saturn's quasiperiodic magnetohydrodynamic waves. *Geophysical Research Letters*, 43(21):11–102.